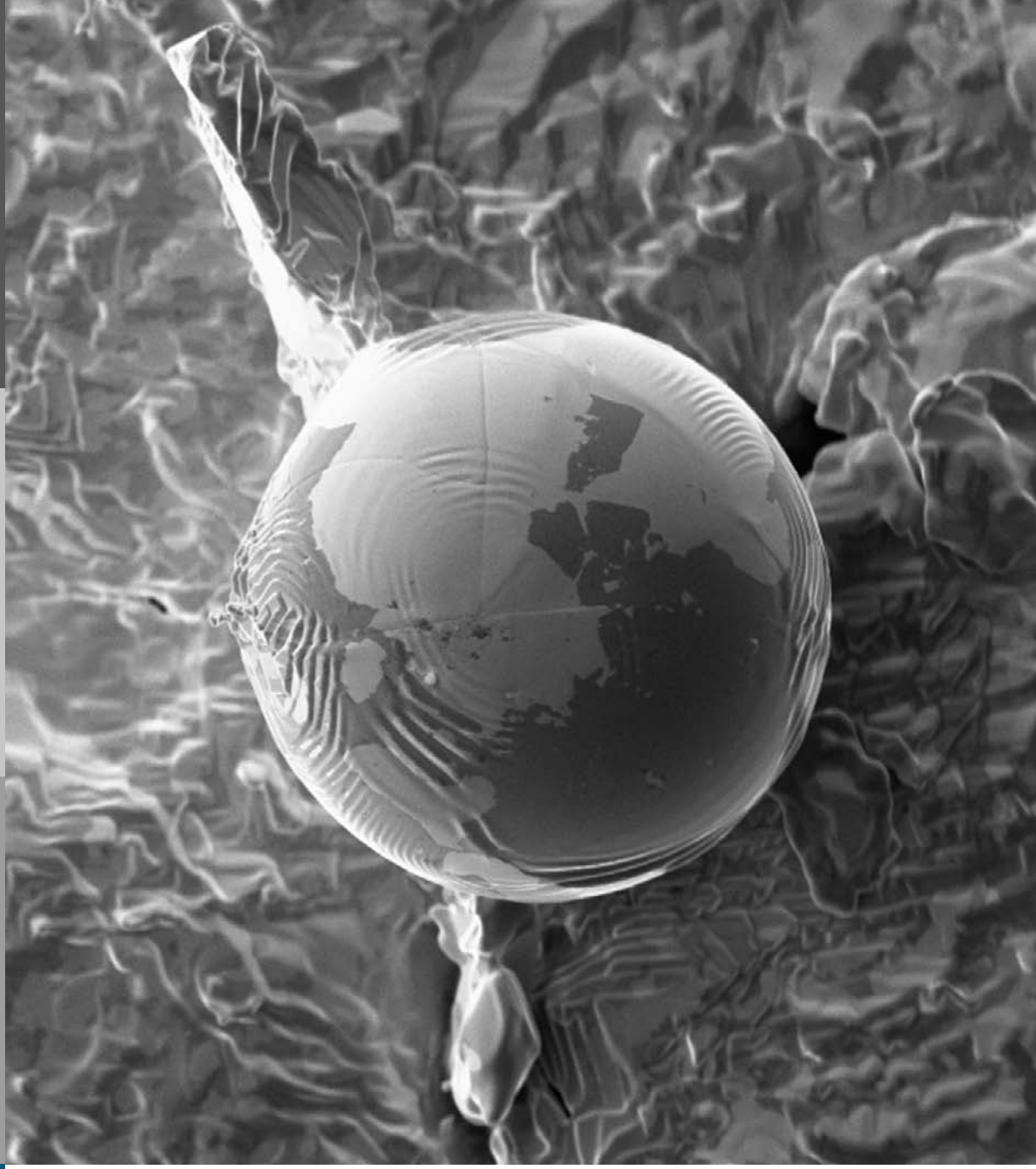

Performance of Tungsten-Based Materials and Components under ITER and DEMO Relevant Steady-State Thermal Loads

Guillaume Henri Ritz

Mitglied der Helmholtz-Gemeinschaft

JÜLICH
FORSCHUNGSZENTRUM

Schriften des Forschungszentrums Jülich
Reihe Energie & Umwelt / Energy & Environment Band / Volume 128

Forschungszentrum Jülich GmbH
Institute of Energy and Climate Research (IEK)
Microstructure and Properties of Materials (IEK-2)

Performance of Tungsten-Based Materials and Components under ITER and DEMO Relevant Steady-State Thermal Loads

Guillaume Henri Ritz

Schriften des Forschungszentrums Jülich
Reihe Energie & Umwelt / Energy & Environment Band / Volume 128

ISSN 1866-1793 ISBN 978-3-89336-755-9

Bibliographic information published by the Deutsche Nationalbibliothek.
The Deutsche Nationalbibliothek lists this publication in the Deutsche Nationalbibliografie; detailed bibliographic data are available in the Internet at http://dnb.d-nb.de.

Publisher and Distributor:	Forschungszentrum Jülich GmbH Zentralbibliothek 52425 Jülich Phone +49 (0) 24 61 61-53 68 · Fax +49 (0) 24 61 61-61 03 e-mail: zb-publikation@fz-juelich.de Internet: http://www.fz-juelich.de/zb
Cover Design:	Grafische Medien, Forschungszentrum Jülich GmbH
Printer:	Grafische Medien, Forschungszentrum Jülich GmbH
Copyright:	Forschungszentrum Jülich 2011

Schriften des Forschungszentrums Jülich
Reihe Energie & Umwelt / Energy & Environment Band / Volume 128

D 82 (Diss.,RWTH Aachen University, 2010)

ISSN 1866-1793
ISBN 978-3-89336-755-9

The complete volume is freely available on the Internet on the Jülicher Open Access Server (JUWEL) at http://www.fz-juelich.de/zb/juwel

List of symbols and abbreviations

Symbols

ΔT	Temperature rise (during thermal shock loads)	[K]
Δt	Pulse duration	[s]
ϵ	Absorption coefficient (of tungsten for electrons)	[-]
λ	Thermal conductivity	$[W \cdot K^{-1} \cdot m^{-1}]$
ρ	Density	$[kg \cdot m^{-3}]$
σ	Nuclear cross section	[barns]
τ_E	Energy confinement time	[s]
c	Speed of light	$[m \cdot s^{-1}]$
c_p	Specific heat	$[J \cdot kg^{-1} \cdot K^{-1}]$
d	Distance	[m]
f	Frequency	[Hz]
I	Current	[A]
K_D	Kinetic energy	$[kg \cdot m^2 \cdot s^{-2}]$
m	Mass	[kg]
n	Ions density	$[m^{-3}]$
P	Power	[W]
P_{abs}	Absorbed power density	$[W \cdot m^{-2}]$
P_{local}	Local power density	$[W \cdot m^{-2}]$
R_a	Roughness	[m]
S	Area	$[m^2]$
T	Temperature	[K]

t	Time	[s]
U	Acceleration voltage	[V]
v	Beam velocity	[m·s^{-1}]

Abbreviations

BSE	Backscattered Electron
CBN	Cubic Boron Nitride
CFC	Carbon Fibre Composite
CFD	Computational Fluid Dynamics
CTE	Coefficient of Thermal Expansion
CVD	Chemical Vapor Deposition
DBTT	Ductile-to-Brittle Transition Temperature
DPA	Displacement Per Atom
EBSD	Electron Backscattered Diffraction
ECM	Electro-Chemical Machining
EDM	Electric Discharge Machining
EDX	Energy-Dispersive X-ray
ELM	Edge Localized Mode
FE	Finite Element
FWHM	Full-Width Half-Maximum
FZJ	Forschungszentrum Jülich
HEMJ	HElium-cooled Modular Jet
HFF	Heat Flux Factor
HHF	High Heat Flux
JUDITH	Jülicher Divertor Testanlage in den Heißen Zellen
KIT	Karlsruhe Institute of Technology
LCMF	Last Closed Magnetic Surface
MFR	Mass Flow Rate
PFC	Plasma-Facing Component

PFM	Plasma-Facing Material
PIM	Powder Injection Moulding
PPCS	Power Plant Conceptual Study
RCT	Recrystallisation Temperature
RT	Room Temperature
SEM	Scanning Electron Microscopy
SOL	Scrape-Off Layer
VDE	Vertical Displacement Event
VPS	Vapor Plasma Spraying

Kurzfassung

Bei Kernfusionsanlagen ist die Innenwand, die direkten Kontakt mit dem Plasma hat, hohen Energieflüssen ausgesetzt. Die stärksten Belastungen treten dabei im Bereich des Divertors im unteren Teil der Plasmakammer auf, der kontinuierlichen Wärmelasten mit Leistungsdichten von mehreren $MW \cdot m^{-2}$ sowie transienten Belastungen widerstehen muss. Letztere sind sehr kurzzeitig (Millisekunden- und Submillisekundenbereich), deponieren aber höchere Leistungsdichten von einigen $GW \cdot m^{-2}$. Die Anforderungen an Materialien, das diesen extremen Bedingungen widerstehen kann, führte zur Wahl von Wolfram, das die Folgenden vorteilhaften Eigenschaften besitzt: eine hohe Schmelztemperatur, gute thermische Leitfähigkeit, hohe Widerstandsfähigkeit gegen physikalisches Sputtern, geringe Wärmeausdehnung und niedrige Aktivierbarkeit. Diese Eigenschaften machen es zu einem interessanten und vielversprechenden Kandidat für die Auskleidung der Divertoren zukünftiger Fusionsanlagen wie ITER und DEMO.

Für den DEMO Divertor wurde eine konzeptionelle Studie an heliumgekühlten Wandkomponenten aus Wolfram durchgeführt. Dieses Konzept wurde umgesetzt und unter DEMO relevanten zyklischen Wärmebelastungen getestet. Die anschließende Untersuchung der Komponenten vor und nach der thermischen Belastung mittels Metallographie ermöglichte es, die Mechanismen, die zum Versagen der Komponenten führten, zu bestimmen. Es wurde unter anderem gezeigt, dass die Wolframsorte und die damit verbundene Rissstruktur einen Einfluss auf das Verhalten der Wandkomponenten unter hohen Wärmeflüssen hatte.

Eine Eignungsstudie sollte unter besonderer Berücksichtigung der auftretenden Rissbildung zeigen, wie sich bestimmte Wolframsorten unter fusionsrelevanten kontinuierlichen Wärmelasten verhalten. Insgesamt wurden sieben kommerziell verfügbare Wolframsorten von zwei Herstellern untersucht. Da das thermische Verhalten der Materialien stark mit deren Mikrostruktur verknüpft ist, wurden im Rahmen dieser Studie verschiedene Materialgeometrien und Herstellungsverfahren miteinander verglichen. Dies beinhaltete eine selbst entworfene, aktivgekühlte Komponente, die auf dem Flachprobendesign basierte, um alle Materialien denselben Oberflächentemperaturen zu belasten. Die kontinuierlichen Wärmelasten mit überlagerten transienten Wärmelasten wurden mit einem Elektronenstrahl, der die Komponenten mit Frequenzen in kHz Bereich scannte, auf die Komponenten aufgebracht. In den Versuchen wurde die Leistungsdichte, die Oberflächentemperatur der Proben und die aufgebrachten Zyklenzahlen variiert. Der Temperaturgrenzwert für Rissbildung konnte zwischen 1000 und 1900°C lokalisiert werden. Sobald Rissbildung einsetzte, hatte die Oberflächentemperatur keinen Einfluss mehr auf das Rissnetzwerk im belasteten Bereich. Allerdings wuchs die Risstiefe mit der Zyklenzahl an, war aber immer auf einen oberflächennahen Bereich von ca. 100 μm begrenzt.

Ein Nachteil von Wolfram ist sein sprödes Verhalten bei Raumtemperatur, das eine Verarbeitung erschwert und geeignete Bearbeitungmethoden erfordert. Die Untersuchung der heliumgekühlten Wandkomponenten aus Wolfram zeigte Risse in den maschinell bearbeiteten Oberflächen. Um das Verhalten der Wandkomponenten besser zu verstehen, war es notwendig, den Einfluss der Oberflächenvorschädigung auf die Gesamtschädigung unter starken Wärmelasten zu untersuchen. Im Rahmen der Eignungstests wurden daher vorgeschädigte und nicht vorgeschädigte Proben starken Wärmeflüssen ausgesetzt. Vorgeschädigte Oberflächen erhielt man durch Oberflächenbearbeitung mittels Funkenerosion (electric discharge machining) und defektfreie Oberflächen durch Polieren. Nach thermischer Beanspruchung zeigte sich, dass die Vorschädigung in den höchsten Rissdichten resultierte. Die Risstiefe war hingegen unabhängig von der Zyklenzahl ganz im Gegensatz zu den Rissen, die in den polierten Oberflächen auftraten.

Abstract

In nuclear fusion devices the surfaces directly facing the plasma are irradiated with high energy fluxes. The most intense loads are deposited on the divertor located at the bottom of the plasma chamber, which has to withstand continuous heat loads with a power density of several $MW \cdot m^{-2}$ as well as transient events. These are much shorter (in the millisecond and sub-millisecond regime) but deposit a higher power densities of a few $GW \cdot m^{-2}$. The search for materials that can survive to those severe loading conditions led to the choice of tungsten which possesses advantageous attributes such as a high melting point, high thermal conductivity, low thermal expansion and an acceptable activation rate. These properties made it an attractive and promising candidate as armor material for divertors of future fusion devices such as ITER and DEMO.

For the DEMO divertor, conceptual studies on helium-cooled tungsten plasma-facing components were performed. The concept was realized and tested under DEMO specific cyclic thermal loads. The examination of the plasma-facing components by microstructural analyses before and after thermal loading enabled to determine the mechanisms for components failure. Among others, it clearly showed the impact of the tungsten grade and the thermal stress induced crack formation on the performance of the armor material and in general of the plasma-facing component under high heat loads.

A tungsten qualification program was launched to study the behaviour of various tungsten grades, in particular the crack formation, under fusion relevant steady-state thermal loads. In total, seven commercially available materials from two industrial suppliers were investigated. As the material's thermal response is strongly related to its microstructure, this program comprised different material geometries and manufacturing technologies. It also included the utilization of an actively cooled specimen holder which has been designed to perform sophisticated material tests at different surface temperatures. The steady-state thermal loading with superimposed transient thermal loading was induced by high frequency scanning of the electron beam. The steady-state thermal loading was performed with different power densities, surface temperatures and cycle numbers. The cracking threshold was investigated in a temperature range of 1000 to 1900°C. Once cracks occurred, the surface temperature had no impact on the crack network of the loaded surface. The cracks grew in depth with increasing the cycle number. However, under all loading conditions, crack depths were still limited in a shallow region, namely below 100 μm.

One disadvantage of tungsten is its high brittleness at room temperature which makes the manufacturing of tungsten parts challenging as it requires suitable machining techniques. The examination of the helium-cooled tungsten plasma-facing components revealed cracks in as-machined surfaces. For a better understanding of the perfor-

mance of plasma-facing components it was necessary to estimate the impact of pre-cracked surfaces on the components' degradation under high heat fluxes. Therefore, in the frame of the tungsten qualification program, specimens with defect-free and pre-cracked surfaces were exposed to high heat fluxes. Surface processing by electric discharge machining (EDM) led to pre-cracked surfaces and defect-free surfaces were achieved by polishing. EDM-pre-cracking resulted in a high crack density consisting of inter- and intra-granular cracks, which did not change after thermal loading. Even more, the cracks did not grow with the cycle number in contrast to thermo-mechanical induced cracks on polished surfaces which occurred at lower crack density.

Contents

1 Introduction **1**

1.1 Nuclear fusion concepts 1

1.2 Magnetic confinement fusion devices 5

1.3 Energy deposition on in-vessel walls 8

1.4 Plasma-facing components 11

1.5 Plasma-facing materials 13

1.6 Tungsten as plasma-facing material 15

1.7 Thermally induced damage in tungsten 16

1.8 Scope of the work 17

2 Failure mode of plasma-facing components for the European DEMO divertor **19**

2.1 Introduction 19

2.2 Design of the divertor component 19

2.3 Fabrication of divertor modules 21

2.3.1 Material selection 22

2.3.2 Joining technology 23

2.4 Testing under cyclic thermal loads 24

2.5 Results 26

2.5.1 Plasma-facing part 26

2.5.2 Structural-heat sink part 30

2.5.3 Tungsten-steel interface 36

3 Performance of tungsten grades under steady-state thermal loads **39**

3.1 Introduction 39

3.2 Materials selection 40

3.3 Components for testing under thermal loads 44
3.3.1 Design of the components 44
3.3.2 Fabrication of the components 45
3.4 Testing under fusion relevant thermal loads 48
3.4.1 The electron beam facility JUDITH 1 48
3.4.2 Thermal loading of cracked surfaces 52
3.4.3 Thermal loading of defect-free (polished) surfaces 52
3.5 Results 54
3.5.1 Surfaces pre-cracked by electric discharge machining 54
3.5.2 Surfaces prepared by polishing 67
3.5.3 Comparison of pre-cracked and polished surfaces after thermal loads 82
3.5.4 Performance of the grades under the combined thermal load . . 86

4 Summary and conclusions **95**

A Appendix: machining qualification program for tungsten **99**
A.1 Machining techniques 99
A.2 Machining parameters 102
A.3 Results (examination of machined surfaces) 105
A.3.1 Turning and milling 106
A.3.2 Cutting wheels 110
A.3.3 Diamond wire cutting 111
A.4 Summary and conclusions 111

Bibliography **113**

1 Introduction

1.1 Nuclear fusion concepts

Nuclear fusion is the physical process describing the joint of at least two atomic nuclei to form a heavier nucleus. Fusion reactions are accompanied by the release of huge energy quantities when the average mass of the nucleons involved in the process decreases between the initial and the final state. The missing mass, called the mass defect, is a measure of the nuclear binding energy which holds the nucleus together in spite of the electromagnetic force tending to repel the charged particles. This binding energy can be calculated from Einstein's equation $E = m \cdot c^2$. Nuclei fuse with a yield of energy when the binding energy of the formed nucleus is less than that of nickel (^{62}Ni) at the peak of the binding energy curve because the nuclear particles will be more tightly bound than they were in the lighter nuclei (figure 1.1) [1]. The decrease in mass

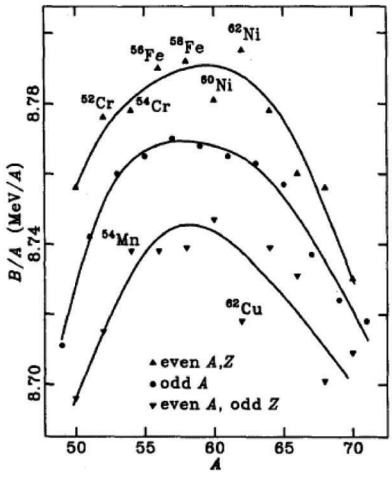

Figure 1.1. Average binding energy per nucleon against mass number of the strongest bound nucleons [1].

comes off in the form of kinetic energy carried by the end products and is equal to the difference between the binding energies of the fuel and the fusion products. The fusion of elements more massive than Ni would soak up energy rather than deliver it.

The nuclear force which binds nucleons together dominates at distances of about a few nucleon radii whereas the competing electromagnetic force dominates at longer distances. It is highly unlikely that two positive nuclei will approach each other close enough to undergo a fusion reaction unless they have an energy sufficient to overcome the Coulomb barrier. Typically, an average kinetic energy of at least 10^4 eV is necessary to enable fusion reactions. This explains why the centre of a star must be hot for the fuel to burn. In the sun, fusion proceeds at temperatures around $1.5{\cdot}10^7$ K. At such temperatures the atoms ionise (the electrons are stripped of the nuclei) forming a high-energy state of matter called plasma.
The so-called cross section σ [barn] characterises in a quantitative form the probability that a pair of nuclei cross the Coulomb barrier, i.e. undergo nuclear fusion. The cross section was measured for several fusion reactions over a wide range of particle energies. The largest values were obtained in the reaction between deuterium (D) and tritium (T), and this at even lower temperatures than those of the other fusion reactions (figure 1.2).

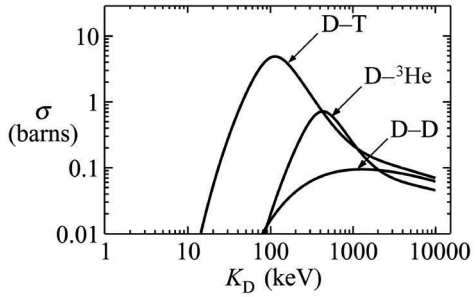

Figure 1.2. Experimentally determined cross sections for the the deuterium-tritium (D-T), deuterium-^{3}He (D-^{3}He), and deuterium-deuterium (D-D) fusion reactions as a function of the deuterium average kinetic energy $K_\mathrm{D} = \frac{1}{2} m_\mathrm{D} v_\mathrm{D}^2$ [2].

The large amount of released energy per fusion reaction led to the idea of using controlled fusion for a power plant. The most efficient reaction to utilise fusion on earth is the D-T reaction because it has the lowest necessary average kinetic energy for starting fusion reactions, the highest cross section up to a few hundred keV and a high energy yield. It generates a helium (He) nucleus and a free neutron (n) and releases 17.6 MeV binding energy apportioned according to the mass ratio (figure 1.3). Some other possible reactions for controlled fusion are:

$$\mathrm{D} + \mathrm{D} \rightarrow {}^3\mathrm{He}\ (0.82\ \mathrm{MeV}) + \mathrm{n}\ (2.45\ \mathrm{MeV}) \tag{1.1}$$

$$\mathrm{D} + \mathrm{D} \rightarrow \mathrm{T}\ (1.01\ \mathrm{MeV}) + \mathrm{H}\ (3.02\ \mathrm{MeV}) \tag{1.2}$$

$$\mathrm{D} + {}^3\mathrm{He} \rightarrow {}^4\mathrm{He}\ (3.6\ \mathrm{MeV}) + \mathrm{H}\ (14.7\ \mathrm{MeV}) \tag{1.3}$$

It is also expected to manage the D-D reaction in the future since it has some advantages with respect to irradiation processes and absence of tritium. One concern which will

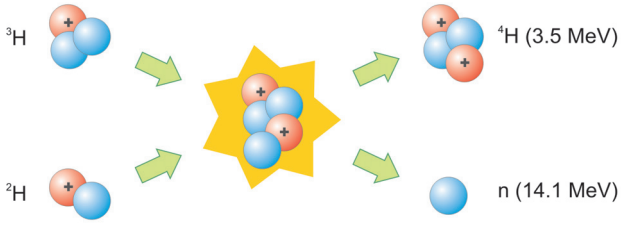

Figure 1.3. The deuterium-tritium fusion. Deuterium and tritium form an intermediate state ^{5}He with a half-life time of 0.6 MeV ($\sim 5.5 \cdot 10^{-22}$ s) [3]. It decays into a stable ^{4}He nucleus and a free neutron with kinetic energies of 3.5 MeV and 14.1 MeV respectively.

still remain is the radiation of energetic neutrons that will activate the materials in fusion devices. Nevertheless, if low-activation materials are utilised, the most active wastes created by fusion will need to be confined a few hundred years only compared to millions of years for wastes created by nuclear fission. Fusion is thus said to be free of long-term wastes. Furthermore, there would be no direct contribution to greenhouse gases or acidic emissions during the nuclear fusion reactions. Therefore, nuclear fusion offers an energy-conversion process with abundant resources and major environmental advantages.

The fuel ressources for controlled fusion are available in great quantities. Deuterium is abundant as it can be extracted from all forms of water (10 g of deuterium can be extracted from 500 l of water). Tritium, not available on Earth in sufficient amounts due to its high decay rate (it has a radioactive half-life of about 12.5 years), is planned to be breeded in-situ in the fusion device by bombarding a lithium wall with the neutrons from the deuterium-tritium reaction itself:

$$^6\mathrm{Li} + \mathrm{n} \rightarrow {}^4\mathrm{He}\ (2.05\ \mathrm{MeV}) + \mathrm{T}\ (2.73\ \mathrm{MeV}) \tag{1.4}$$

$$^7\mathrm{Li} + \mathrm{n} \rightarrow {}^4\mathrm{He} + \mathrm{T} + \mathrm{n} - 2.47\ \mathrm{MeV} \tag{1.5}$$

In stars, the tendency of the plasma to disperse and therefore to cool down is balanced out by the gravitational force. For controlled fusion, the problem arises how to prevent the plasma from dispersing and touching any cold matter, possibly damaging its environment and eventually loosing its kinetic energy. Practical efforts to harness fusion energy involve two approaches: *inertial* and *magnetic* confinement. Within the international fusion community, the magnetic confinement is nowadays the one perceived as being able to provide successful results faster. The two strategies for inertial confinement are laser fusion and ion-beam fusion. Directed onto a tiny fuel pellet (for example a D-T mass), the energy influx evaporates the outer layer of the pellet, producing energetic collisions against the remainder of the pellet, pushing it inward. The shock waves compress the inner core to densities 10^3 to 10^4 times greater than

normal by generating a pressure as high as 10^{17} Pa for periods as short as 10^{-9} s. At maximum compression of the fuel, the energy in converging shock waves is sufficient to heat the very centre of the fuel to temperatures high enough to induce fusion reactions. While the inertial confinement strategy tends to fuse nuclei so fast that they do not have time to move apart, the magnetic confinement seeks to extend the time that ions spend close together by trapping the plasma within magnetic fields. The charged particles of the plasma are forced into circular and helical orbits around the magnetic field lines, thereby confining the particles. On the other hand, they are able to move freely both along and across the magnetic lines. In a suitably shaped magnetic field cage it is therefore possible to confine a plasma and keep it perpetually in looping paths which do not touch the wall.

However, when confined magnetically, the plasma is continuously losing energy due to particle transport over the plasma boundary and radiation, namely *Bremsstrahlung* radiation) related to collisions between free electrons and ions (Coulomb collisions), line radiation related to collisions between free electrons and atoms or impurities scratched off from the inner wall of the plasma chamber, and synchrotron radiation related to the motion of charged particles in a magnetic field. All plasma's energy losses (P_{loss}) have to be balanced by the energy sources. The main energy source comes from the alpha particles (He nuclei) which transfer their energy to the plasma by collision (P_{alpha}). To heat the fuel, additional energy is supplied by an auxiliary heating system (P_{heat}). The energy balance of the plasma is in equilibrium when the energy sources feeding the plasma compensate the energy losses cooling it down:

$$P_{\text{loss}} = P_{\text{alpha}} + P_{\text{heat}}$$

The total power produced by the D-T fusion reaction P_{fus} is divided between the products of the reaction, the alpha particles and the neutrons:

$$P_{\text{fus}} = P_{\text{alpha}} + P_{\text{neut}}$$

The efficiency of a nuclear fusion reactor can be characterised by the factor Q, which is the ratio of the fusion power to the input power required to heat the fuels:

$$Q = \frac{P_{\text{fus}}}{P_{\text{heat}}}$$

The situation corresponding to $P_{\text{fus}} = P_{\text{heat}}$ (Q = 1) is called *break-even*. As a D-T plasma is heated to thermonuclear conditions, the alpha particle heating provides an increasing fraction of the total heating. When a point is reached where the energy losses are completely balanced by the alpha particle heating ($P_{\text{loss}} = P_{\text{alpha}}$) the externally supplied power can be removed ($P_{\text{heat}} = 0$) and the plasma temperature is sustained by internal heating. The situation corresponding to $P_{\text{heat}} = 0$ ($\text{Q} \to \infty$) is called ignition. By putting the plasma power balance into terms of practical plasma physical parameters, namely the plasma temperature (T), ion density (n) and energy

confinement time (τ_E), the conditions for ignition are met when:

$$n\tau_E T \geq 3 \cdot 10^{21} \text{ keV} \cdot \text{s} \cdot \text{m}^{-3} \tag{1.6}$$

This product is called the fusion (or triple) product derived from the so-called *Lawson Criterion*. In case of a D-T plasma, ignition would be reached for example by $n = 10^{20}$ m^{-3}, $T = 10$ keV and $\tau_E > 3$ s. The japanese tokamak JT-60U achieved the highest value of triple product up to now (2010): $1.53{\cdot}10^{21}$ keV·s·m^{-3} [4].

1.2 Magnetic confinement fusion devices

There are two main types of magnetic confinement device: *tokamak* and *stellarator*. A tokamak is a toroidal (doughnut-shaped) chamber with magnetic coils. The plasma is confined in the shape of a torus by means of superposed magnetic fields: a toroidal magnetic field externally generated by toroidal field coils and a poloidal field generated by electric currents flowing within the plasma. The resulting magnetic lines of force are helixes that spiral around the torus to minimize particle leakage. A third, poloidal field generated by vertical field coils, fixes the position of the current in the plasma (figure 1.4). The plasma current is induced by a transformer and increases continuously

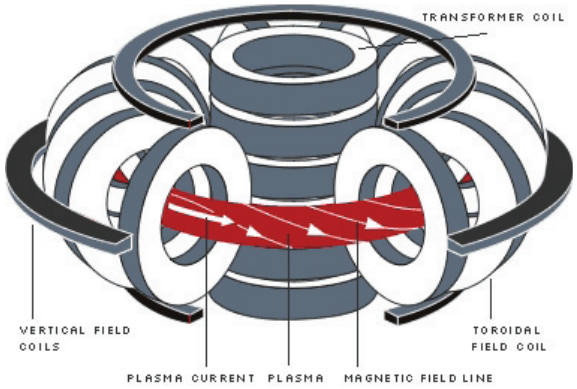

Figure 1.4. Scheme of the magnetic circuits of a tokamak [5].

for a limited time. The transformer must be "discharged" frequently and the current started up afresh. This is why a tokamak does not work in continuous but in pulsed mode. In a stellarator the magnetic cage is produced with a single coil system without a longitudinal net-current in the plasma (without a transformer). This makes stellarators suitable for continuous operation in opposition to tokamaks. In order to achieve steady state operation in a future tokamak power plant, investigations are being conducted on methods of generating current in continuous mode, e.g. using high-frequency waves. Various magnetic confinement devices were designed among which the tokamak is the most highly developed.

The magnetic configuration of a tokamak confines individual particles, namely ions and electrons. This means that the charged particles which does not interact with charges and currents generated by other particles follows a trajectory that stays close to the toroidal magnetic surface. However, the particles undergo other phenomena resulting in more complex transport mechanisms. The Coulomb collisions between particles make them deviate from their initial trajectory and lead to a transport of matter and heat transverse to the magnetic field lines. Additionally, the plasma turbulence driven largely by the ion temperature gradient (hot plasma at the center, colder at the edge) produces electric and magnetic field fluctuations that cause random perturbations in the guiding center orbits of the particles. The randomness of the fluctuations leads to a collision-like transport of particles and heat. The Coulomb collisions and the plasma turbulence are two mechanisms by which the particles diffuse from the discharge core towards the outside, giving rise to a confinement loss. The particles end up by leaving the magnetic trap and encounter the surrounding wall of the plasma vessel. The high energy of the incident particles may overcome the binding energy of the wall atoms which are then ejected, eventually entering and contaminating the plasma. Unlike light hydrogen atoms, the heavy atoms (with a high atomic number Z) of the wall element are not completely ionised even at the high fusion temperatures. The higher the atomic number of these impurities, the more electrons are still bound to the atom core. Electron collisions give rise to an excitation of the bound electrons and the deexcitation of the excited electron level produces a photon that escapes from the plasma. Therefore, the impurities make the plasma electron population to loose energy during each deexcitation by radiation. In this way, the impurities cool down the plasma, rarefy it, and thus reduce the fusion power.

In order to reduce the fraction of impurities in the plasma core as much as possible, a special magnetic field configuration tends to exclude the region where the so-called plasma-wall interaction [6] takes place: this is the divertor magnetic configuration (figure 1.5). The core plasma is characterised by closed field lines whereas the edge field lines are open and directed towards a solid obstacle, the so-called divertor. The border magnetic surface between the two zones is called *Last Closed Magnetic Surface* (LCMF) or separatrix and the region of open field lines is called the *Scrape-Off Layer* (SOL). The flow of particles and heat leaving the plasma by diffusion is guided by following the open field lines towards the divertor which is situated relatively far away from the central plasma. After interaction, the potential impurities are thus more likely to be ionised in the SOL, swept by it and collected by the divertor plates. They then remain in a closed circuit without interfering with the central plasma. It was while testing this new configuration that the improved confinement H-mode was discovered on the German machine ASDEX during the eighties, which definitively ensured the success of this system. The largest present tokamaks, like JET and JT-60U, are fitted with this type of device.

The next important step on the road to nuclear fusion power plants, ITER [8, 9], will be based on the divertor magnetic configuration as well. ITER is a large-scale

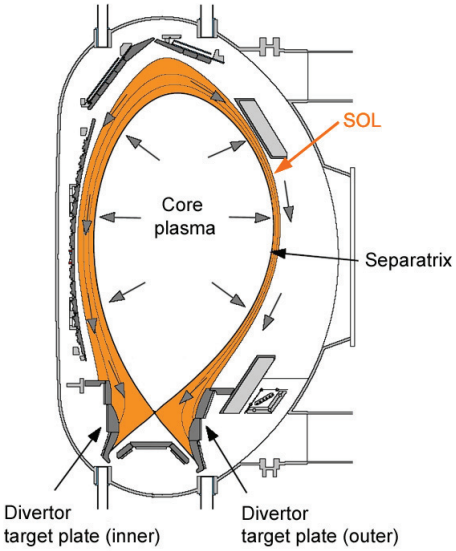

Figure 1.5. Scheme of the poloidal cross section of a tokamak equipped with the divertor configuration [7]. The diffusing particles are guided along the magnetic field lines (grey arrows in the orange field) to a remote location away from the plasma core where they are intercepted by the divertor.

scientific experiment intended to prove the viability of fusion as an energy source (i.e. producing more power than it consumes) and to collect data and technologies necessary for the design and the operation of the first electricity-producing fusion power plant [10]. For 50 MW of input power, 500 MW of fusion (or output) power (Q = 10) will be produced continuously for at least 400 seconds [11, 12]. In comparison, JET succeeded in generating 70 % of input power with a record fusion power of 16 MW. As seen in existing tokamaks the confinement time increases with the major radius of the machine and so does the tokamak performance. Therefore, to achieve the high fusion power foreseen in ITER, it is necessary to increase the size of the tokamak. Consequently, ITER will be a superconducting tokamak of a size yet unequalled with a major radius two times larger than that of JET (∼6 m compared to ∼3 m) (figure 1.6). Launched as a bold proposition for international collaboration in 1985 the ITER Agreement includes the European Union (EU), China, India, Japan, Korea, Russia and the United States (US)

Upon the expected success of ITER, a demonstration fusion reactor, DEMO, will be built [15]. DEMO will resemble a commercial fusion power plant as closely as possible. Most of the technologies developed for ITER will be relevant for DEMO. As ITER is already a reactor class machine only a few but very important technological developments will be missing for DEMO to utilize all technologies required in a commercial device. DEMO will demonstrate the large scale production of electrical power (whereas

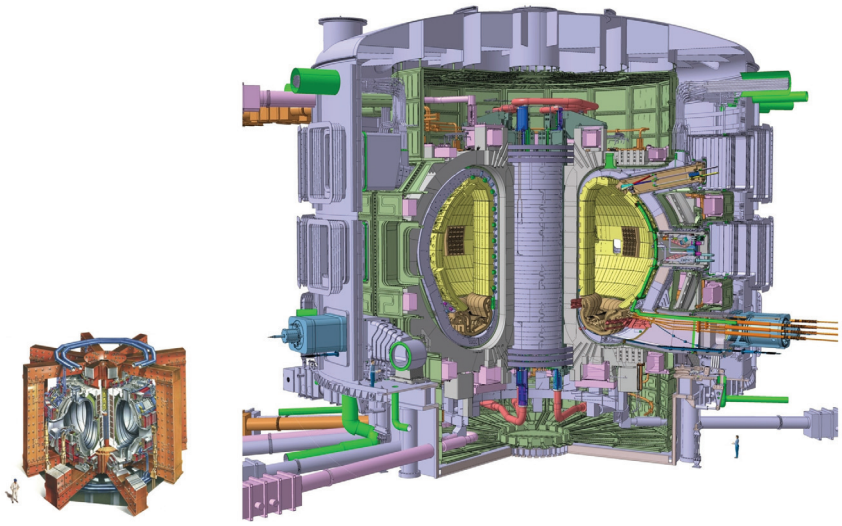

Figure 1.6. Cutaways of tokamak devices JET (left side) and ITER (latin for "the way") [13, 14]. JET is the biggest tokamak in the world up to now. The construction of ITER started January 2007 and the first plasma is scheduled in 2019.

ITER as well as earlier experimental fusion devices will merely dissipate the thermal power they produce into the atmosphere as steam). DEMO is designed to produce at least four times the ITER fusion power continuously (2000 to hopefully 4000 MW of thermal output), thus reaching a level of power production on the scale of a modern electric power plant. DEMO's goal is to produce 25 times as much power as is required for the breakeven (Q = 25). A conceptual design for such a machine could be completed in 2017. DEMO could start operation in the 2030s and put fusion power into the grid as early as 2040.

1.3 Energy deposition on in-vessel walls

The magnetic field confining the plasma occupies the entire volume of the plasma vessel. Consequently, the plasma also propagates till it touches the vessel wall, which absorbs at the areas of contact, apart from the radiation, the entire energy transported by the plasma particles. Due to the shape of the magnetic lines in the divertor configuration (figure 1.5) the plasma energy is not deposited homogeneously all over the vessel components during tokamak operation. Although the highest heat load is concentrated on the divertor, the so-called first wall (the part of ITER coloured in yellow in figure 1.6) also absorbs a fraction of the heat flux. For example, the highest heat loads in ITER during normal (quasi-stationary) plasma operation are expected to be

around 0.5 MW·m^{-2} on the first wall and up to 10 MW·m^{-2} on the divertor [16]. On top of the steady state heat loads another type of loads, more intense, exists. Once a plasma equilibrium is reached (when the Lorentz force balances the pressure gradient force of the plasma, which tries to expand like a gas) plasma instabilities arise. These instabilities are classified as transient thermal loads. During transient events a large amount of energy with densities up to several MJ·m^{-2} is deposited in extremely short time periods (in the ms range) on local surface areas [17]. There are three main classes of instabilities, each with specific energy densities, durations and occurrences: the *edge localized modes* (ELMs), the *plasma disruptions*, and the *vertical displacement events* (VDEs) (figure 1.7).

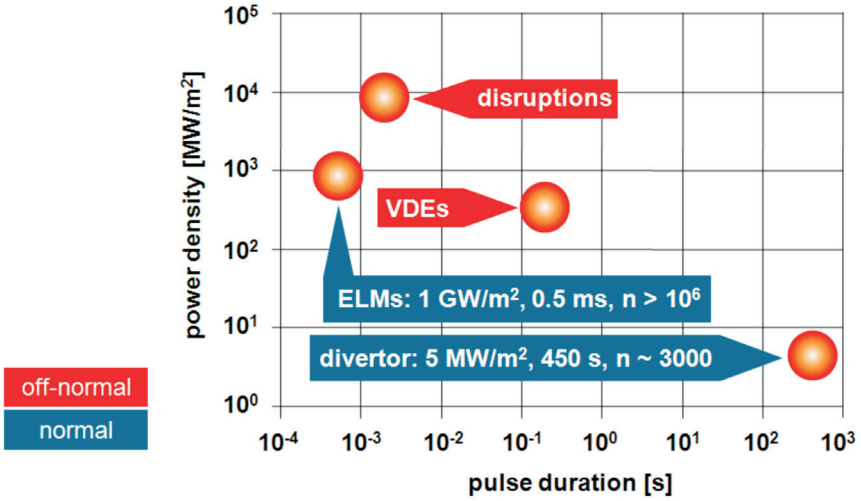

Figure 1.7. Plasma induced thermal loads on divertor surfaces in ITER [18]. The quasi-stationary plasma operation is associated with periodic edge localized modes. In addition, off-normal events (plasma disruptions and vertical displacement events) occur at random times.

ELMs are instabilities occurring in short periodic bursts during the H-mode operation in divertor tokamaks [19]. The H-mode is a high confinement regime that develops when a tokamak plasma is heated above a characteristic power threshold. It is characterised by a steep pressure gradient at the plasma edge just inside the separatrix. The pressure gradient rises to a high level until an instability, the ELM, prevents the pressure build-up by ejecting energy and particles into the divertor [20]. Unlike disruptions, ELMs lead to a partial confinement loss. ELMs are classified into three types [21]. The type I ELMs are short (0.2 to 0.5 ms) but intense outbursts that reach power densities up to 1 GW·m^{-2}, thus depositing energy densities of ∼0.5 MJ·m^{-2} [22, 23]. They repeat with a frequency of several Hz and are also called "giant" ELMs. The repetition frequency increases with increasing the plasma heating power. They cause a sudden loss of up

to 10-15 % of the plasma stored energy in a few milliseconds. The type II ELMs are weaker than type I ELMs and have a higher frequency up to several thousands Hz. They are also called "grassy" ELMs [24]. The type III ELMs are characterised by weak and frequent outbursts. As their repetition frequency decreases with increasing plasma heating power,+ those ELMs disappear at some point. They are also called "small" ELMs. A single ELM does not cause significant damage in the components of the wall. However, due to their high frequency of occurrence (since a large number of ELMs, $\geq$1000, are expected in each discharge [23]) ELMs may amount to more than 1 million of events in ITER (during the expected 3000 pulses, each with a duration of 400 s).

A plasma disruption is a sudden breakdown of the plasma current caused by instabilities in the spatial confinement of the plasma. The process of plasma disruption can be described in three classical phases. Plasma disruptions typically start with a *precursor phase* during which distortions of the shape of the magnetic field occur. These distortions result in the destruction of the internal magnetic surfaces, which leads to a rapid loss of the plasma energy called *thermal quench*. The latter is followed by a *current quench*, a rapid decay of the plasma current. Each plasma disruption is expected to deposit an energy density of 5 to 20 MJ·m^{-2} in a pulse duration of 0.1 to 5 ms (a power density of 1 to 10 GW·m^{-2}) on the divertor plates and to occur in less than 10 % of operational cycles [25]. Plasma disruptions result in rapid plasma heat loss and termination of the discharge.

VDEs are instabilities during which the whole plasma moves vertically away from its equilibrium position [26]. High elongation plasmas (i.e. high ratio of the plasma cross-sectional height to its cross-sectional width such as those obtained with the divertor configuration) are more prone to this motion due to the more strongly shaped magnetic field required to produce them [27]. The plasma collides with the vessel, causing its current to flow through the vessel components and transfers a substantial fraction of its stored energy to them. This is followed by the onset of a plasma disruption and the loss of vertical control. Each VDE is expected to deposit an energy density of $\sim$60 MJ·m^{-2} in a pulse duration of 100 to 300 ms (200 to 600 MW·m^{-2}) and to occur in about 1 % of operational cycles. Furthermore, VDEs induce a lifetime limiting damage because, due to their relatively long duration, they do not produce a shielding vapor cloud as it happens during any intense but shorter power depositions (disruptions and ELMs) [28]. Thus, in addition to erosion and melting [29], VDEs can severely damage the structural materials and coolant channels beneath the in-vessel surfaces.

Additionally in-vessel components are subjected to high fluxes of energetic neutrons in D-T-burning plasma devices, a critical issue both from a safety point of view but also under the aspect of the component's lifetime [30]. The predicted neutron damage in ITER is $\sim$1 dpa (displacements per atom; for low-Z materials 1 dpa corresponds to $\sim 10^{25}$ n·m^{-2}). Future thermonuclear confinement devices such as DEMO and commercial fusion reactors will exhibit integrated neutron wall loads up to 150 dpa [31].

1.4 Plasma-facing components

In-vessel components, so-called plasma-facing components (PFCs), are key components of a fusion power plant because on the one hand they are submitted to extremely severe operating conditions in terms of heat loads and neutron damage [32, 33] and on the other hand they have a large impact on the overall plant design, performance, availability, safety, and associated cost of electricity. All PFCs are cooled (1) to sustain steady state operation as the heat flux received by these components is extremely intense and (2) to remove the plasma particles energy that is further used in a heat conversion process.
The main PFCs are the the *first wall* and the *divertor* [34]. The first wall covers the inner surfaces of the vacuum vessel [35]. Directly facing the plasma its function is to remove the heat flux. The neutron flux is intercepted by the blanket, which is located immediately behind the first wall [36]. When made of lithium the additional function of the blanket is to produce tritium (*tritium breeding blanket*) through the reaction 1.4 [37]. The ensemble first wall and blanket provides shielding from the heat and neutron fluxes to the vessel and magnets [38]. The divertor is situated along the bottom of the vacuum vessel. Its function is to exhaust the flow of energy from charged particles produced in the fusion reactions and to extract the helium ashes (He ions are burnt in the fusion process and must be replaced by new fuel), the unburned fuel and eroded particles (i.e. impurities) from the plasma [39]. After a collision with the divertor plates, charged particles neutralize (i.e. become atoms or molecules by recombination with electrons) until they either ionise once again in contact with the plasma or are taken out of the chamber thanks to a pumping system installed near the divertor.

The divertor remains an experimental device that needs to be replaced and upgraded several times during the life of ITER. To enable rapid replacement the ITER divertor is made up of 54 remotely-removable cassettes [40]. This approach provides an accurate mechanical support and the flexibility to change the configuration of the PFCs. Each cassette holds three PFCs: the inner and the outer vertical targets, and the dome (figure 1.8) [41]. The PFCs include a thick stainless steel back support with water coolant manifolds for an array of copper alloy heat sinks covered with armour materials, so-called plasma-facing materials (PFMs). The stainless steel structure is bolted to rails on the vessel floor.
Different design options for the attachment of the PFMs to the heat sink have been developed, manufactured and tested [42–48]. Two geometrical configurations can be adopted for the PFCs: *flat tile* and *monoblock* (figure 1.9) [49–51]. The heat sink, in general a precipitation-hardened or a dispersion-strengthened copper (Cu) alloy (e.g. CuCrZr) with an integrated high pressure coolant tube has now become the standard technology for ITER or other existing medium- and long-pulse fusion devices [52–55]. To reduce stresses that might affect the integrity of the PFM or the joint (stresses due to the thermal expansion mismatch between the armour and the heat sink material as well

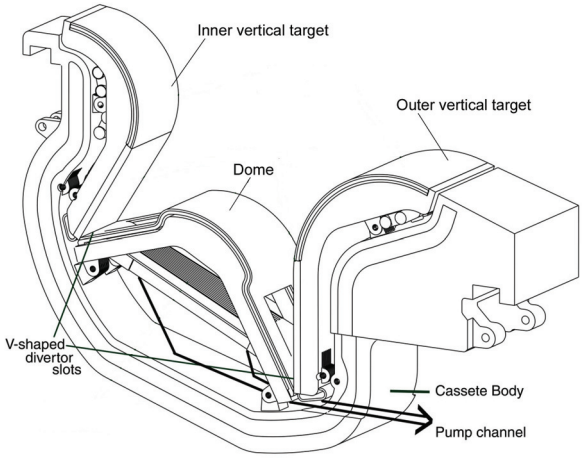

Figure 1.8. ITER divertor cassette [11]. The plasma flux arrives at the edge zone where it neutralises on the divertor plates. The neutral flux is then collected through chevrons and guided to a pump.

as thermally induced stresses due to the thermal gradient during plasma exposure), a segmentation of the PFM using thin slots (or castellations) perpendicular to the surface down to the heat sink (*macrobrush*) is frequently used. The so-called *monoblock* design consists of cube-shaped monolithic tiles with a cylindrical hole in their center in which the water cooled tube is inserted and joined to the armor material by means of a soft Cu interlayer. Small scale components like those shown in figure 1.9 are usually fabricated to test the PFMs under fusion relevant thermal loads using for example electron beam facilities [56, 57].

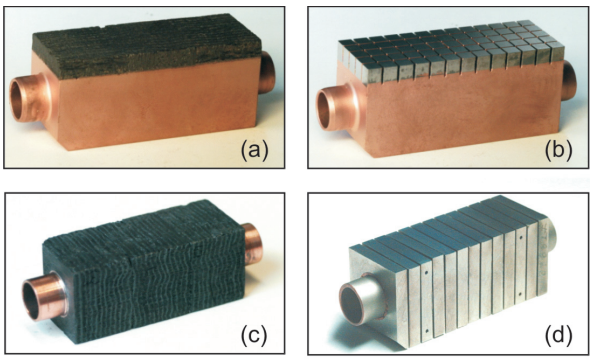

Figure 1.9. Mock-up designs for the ITER divertor plasma-facing components: (a) carbon fibre composite flat tile, (b) tungsten flat tile (macrobrush), (c) carbon fibre composite monoblock, and (d) tungsten monoblock [58].

For DEMO, helium-cooled divertor concepts have been investigated. The advantages of He as coolant compared to water are explained in [59]. The approach for the layout of the divertor is similar to ITER with the division of the component into cassettes composed of outer and inner targets, a dome, and the backbone structure or bulk which houses the manifolds for the coolant. But the design of the divertor PFCs is different because for DEMO and power plant divertors the high operating temperature and irradiation levels preclude the use of Cu and the required thermal conductivity ($\sim$100 W$\cdot$m$^{-1}\cdot$K^{-1}) and maximum allowable temperature (>1000°C) rules out ferritic steel as structural material (for the assumed heat fluxes of 10 MW$\cdot$m^{-2}). The only possibility is then a refractory alloy, e.g. tungsten alloy. Thus, most recent DEMO or power plant divertor design studies in the EU and the US utilise a He-cooled W alloy configuration to provide high-temperature operation and high power cycle efficiency [60].

1.5 Plasma-facing materials

The PFCs have to withstand severe thermal, particle and neutron fluxes. Therefore, the selection of suitable materials for high-end projects such as ITER and DEMO is a challenging task being the object of numerous studies [6]. Ideally, the PFMs have to meet the following requirements [61, 62]:

- high thermal conductivity
- high melting or sublimation point
- high neutron bombardment resistance
- high thermal shock resistance
- low tritium inventory
- low erosion rate
- low plasma contamination (i.e. low Z)
- technical requirements (availability, cost, workability)

Additionally the PFMs have to operate at a broad temperature range from 100 (temperature of the coolant in ITER) up to 2000-3000°C. No known material meets all these requirements at a time but Beryllium (Be), Carbon Fibre Composite (CFC), and tungsten (W) meet most of them. Table 1.1 shows their respective advantages and disadvantages.

In the present design of ITER the armor material for the first wall is Be [59, 63, 64] whereas for the divertor vertical targets, W is employed at the upper curved part and

Beryllium	Carbon fibre composite	Tungsten
+ good thermal conductivity (∼190 $W \cdot m^{-1} \cdot K^{-1}$ at RT)	+ excellent thermal conductivity (up to ∼450 $W \cdot m^{-1} \cdot K^{-1}$ at RT)	+ good thermal conductivity (∼170 $W \cdot m^{-1} \cdot K^{-1}$ at RT)
+ low plasma contamination due to low Z	+ no melting point at all (sublimation starts at ∼3800 K)	+ thermal conductivity hardly influenced by neutron irradiation
+ low activation	+ high thermal shock resistance	+ extremely high melting point (∼3695 K)
+ oxygen getter ⇒ improves vacuum conditions	+ low plasma contamination due to low Z	+ low erosion rate
- low melting point (∼1560 K)	- high erosion rate at high temperature	+ good thermal shock resistance
- short erosion lifetime (melt layer loss)	- high tritium inventory	+ low tritium inventory
- thermal conductivity decreases with temperature	- thermal conductivity decreases significantly with temperature and neutron irradiation	- high Z ⇒ possible plasma contamination
- low neutron radiation resistance	- poor oxidation resistance	- rather poor mechanical properties ⇒ poor workability
- special safety rules related to toxicity		

Table 1.1. Advantages and drawbacks of plasma-facing materials.

CFC is used at the lower straight part around the strike point, where the heat flux is the highest (figure 1.10) [62, 65]. Be, W and CFC armored areas are about 700 m^2, 70 m^2, 50 m^2, respectively [66]. Tungsten only is considered as armor material for the vertical target of the future ITER divertor sets. In fact, W materials were selected as the plasma-facing material of the divertor in the European DEMO reactor design; the use of CFC will be avoided to reduce the tritium inventory [67] and massive erosion [68–73] expected to follow the reduction of thermal conductivity as a result of the neutron irradiation [74–76].

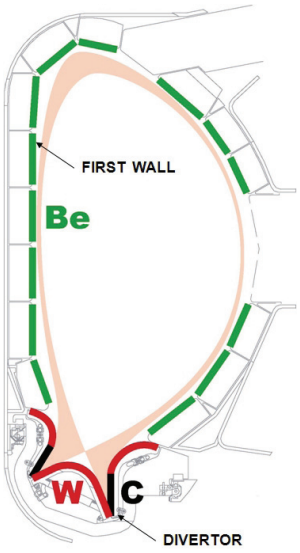

Figure 1.10. Poloidal cross section of ITER showing the layout for the plasma-facing components with the armour materials for the initial operation phase [77].

1.6 Tungsten as plasma-facing material

Tungsten has good thermo-physical properties, namely a high melting point (the highest of all metals) [78], good thermal conductivity and low vapor pressure [79]. Disadvantages of tungsten are melting under intense transient thermal loads, poor machinability, high neutron activation and high volatility of the oxides. Also, W has a relatively low coefficient of thermal expansion (CTE) and is very brittle below the ductile to brittle transition temperature (DBTT), which is in the range of 400 to 600°C [80]. Consequently, cracks occur during thermal shock or thermal fatigue when W is utilised below DBTT. Crack formation is critical because as soon as cracks propagate to the heat sink material the whole component has to be replaced (i.e. cracks can cause component failure). The operating temperature windows of solid pure W is thus limited by the DBTT and the recrystallisation temperature, which is about 1300°C [81]. However, the DBTT varies with the annealing temperature and increases after neutron irradiation.

On the other hand tungsten is desirable because of its low tritium retention and lower sputtering yield enabling longer operation time compared to Be and CFC. Tungsten-armoured components were successfully experimented in fusion devices, for example in the ASDEX Upgrade tokamak [82–85], and W-armoured divertor concepts for DEMO were already investigated [86]. Furthermore, W coatings, deposited on PFMs (e.g. CFC) to increase their loading resistance, were synthesised by vapor plasma spraying (VPS) [87, 88] or chemical vapor deposition (CVD) [89, 90] and investigated under fusion relevant loading conditions [86, 91–99].

The required amount of W for PFCs in ITER is about 85 t. This value stands for a small fraction of the world annual production. Consequently, sufficient W is available at industrial levels even if additional W is necessary to exchange the reactor components [100].

1.7 Thermally induced damage in tungsten

The plasma-wall interaction causes irreversible damage that shortens the lifetime of the components. Typically thermally induced mechanical stresses in W lead to damages such as roughening, swelling, cracking, erosion, and melting, depending on the energy deposition on the material and its base temperature. Electron beam facilities are often used to test materials under high temperatures. Thereby, it has to be taken into account that unlike the conditions in a thermonuclear fusion device the electron beam deposits its energy in the volume of the material. The penetration depth of electrons strongly depends on the acceleration voltage and the density of the material. The thermal response of W under electron beam loading is shown in figure 1.11. As the

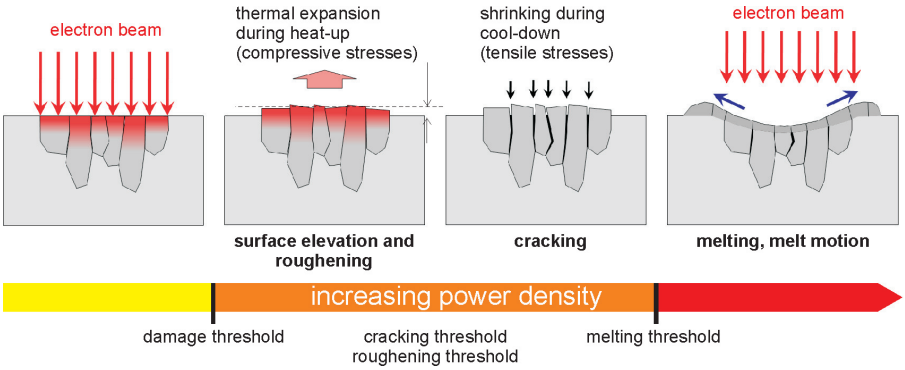

Figure 1.11. Damage types induced in tungsten as a function of the power density applied by electron beam loading.

material is heated up the heat affected grains expand in response to the temperature increase. Due to thermal expansion, grains are subjected to compressive stresses that induce plastic deformation leading to roughening or surface elevation. During cooling down, W shrinks and is subjected to tensile stresses that lead to cracking (once the tensile strength of W is exceeded). Typically cracks occur at grain boundaries where the strength of the material is lower. The cracks proceed along the grain boundaries and lead to particle erosion once the crack depth exceeds the grain size. Thus, the material's degradation is strongly related to its microstructure. Increasing the applied energy density causes melting of the material.

1.8 Scope of the work

The design studies for ITER and DEMO and their success are based on the technical feasibilities of the plasma-facing components which can guarantee a reasonable lifetime from safety and economical points of view. This lifetime is limited by thermally induced damages in the plasma-facing materials. Thus, one of the most critical issues on the utilisation of plasma-facing materials is their performance under high thermal loads. The weak point of W materials is the poor mechanical properties (e.g. the high transition temperature from brittle to ductile, the low toughness) that result in the low cracking resistance under thermo-mechanical loads. To understand the behaviour of W materials and to develop high cracking-resistant W grades, many thermal loading tests were performed with various W grades in the fusion community. However, there are only limited results from the steady-state thermal loads (or thermal fatigue loads) and, moreover, the data only concerned a fraction of W materials. Furthermore, the impact of machining induced defects on the performance is unknown. Therefore, it is still not sufficient to extrapolate the performance of W and predict the components lifetime and failure mode under the cyclic thermal fatigue loads in the fusion relevant conditions (e.g. in ITER and DEMO).
Besides the investigation of high-performance W materials the technology suitable for W machining is also of significant importance. Depending on the machining process and parameters, defects can be introduced in W surfaces during manufacturing due to the brittleness of the material at room temperature. The impact of process induced surface modification on the performance of W under fusion relevant loading conditions has not been studied in detail yet.

The objective of this work was to find key parameters for high-performance W materials (1) and components (2) under cyclic thermal fatigue loads. The ultimate objective was to contribute to the lifetime prediction of W component in terms of cracking resistance (damage threshold, damage development rate).

For this purpose a qualification program for W was launched and experiments were performed under fusion relevant thermal loads in the electron beam facility JUDITH 1 at Forschungszentrum Jülich, Germany. This required the design of specific test modules and Finite Element (FE) calculations to achieve ITER and DEMO specific surface temperatures.
As W materials, pure W supplied by Plansee (Austria) and Polema (Russia) were investigated. Different material's geometries and deformation processes were selected, namely forged rods as well as forged or rolled plates. As it was essential to know the initial states of the W materials to discuss the failure, the microstructure (grain size distribution, porosity, and grain orientation) was analysed in detail by microscopy and metallography before high heat flux loading. Those material characterisations were carried out after each thermal load tests.

Pre-cracked and defect-free (polished) samples were prepared and tested under cyclic thermal fatigue loads. Here, the loading parameters were the various loading surface temperatures (∼1000-2000°C) that generate thermal stress at the loaded surfaces. The surface modification induced by loads were characterised and discussed in terms of (i) material characteristics including (ii) pre-cracking effects, (iii) loading parameters such as surface temperatures, (iv) cycle number and (v) power density (chapter 3).

Within the European Power Plant Conceptual Study (PPCS) [86] a helium-cooled divertor concept for DEMO was developed. The concept is based on the assembly of small W-armoured PFCs so-called fingers. The W components were fabricated and tested under DEMO specific steady-state thermal loads in the electron beam facility TSEFEY using helium cooling. The failure mode of the components was analysed by metallography and material characterisation (chapter 2).

Finally, the fabrication technology for W components was investigated in terms of the damage in machined surfaces and the efficiency. This study included machining techniques such as turning, grinding and electric discharge machining (appendix A).

2 Failure mode of plasma-facing components for the European DEMO divertor

2.1 Introduction

Divertor armour materials for future power plants to be built after ITER (e.g. DEMO) are supposed to be exposed to steady-state thermal loads with a power density of several $MW \cdot m^{-2}$ as well as transient themal loads with a power density of a few $GW \cdot m^{-2}$ [58]. The consequential requirement of an armour material with high resistance to high heat and particle fluxes similar to ITER led to the choice of W as the most suitable material for the divertor [101].
In contrast to ITER, DEMO shall act as a prototype for commercial reactors and therefore provide higher energy conversion efficiency. For this purpose helium(He)-cooled divertor concepts were developed [31]. The use of He at temperatures above 600°C, in addition to increase the thermal efficiency of the power conversion systems [102], enables to keep the temperature of W above its ductile to brittle transition temperature (DBTT), thus lowering the risk of potential damages and improving the general armour material's performance. In addition, He-cooled divertor concepts are compatible with other concepts for the blanket [103–106].
For the European DEMO divertor a so-called He-cooled modular jet (HEMJ) concept was defined as the reference design [107]. It uses small tungsten PFCs, so-called fingers, which are assembled into bigger parts, namely divertor target plates relying on an impingement cooling with high-pressure helium jets (figure 2.1). Among others, Research & Development (R&D) activities towards the DEMO divertor comprise the development and the testing of He-cooled W components under cyclic thermal loads as well as analysis by metallography and material characterisation to study the failure mode of the components [108]. The latter will be described in detail in this chapter.

2.2 Design of the divertor component

The HEMJ design is based on the assembly of small plasma-facing components, the fingers, cooled by He. The requirement of armour materials with a high resistance against sputtering, high thermal conductivity and high mechanical strength led to the selection of W (or its alloys) as the most promising plasma-facing material for the

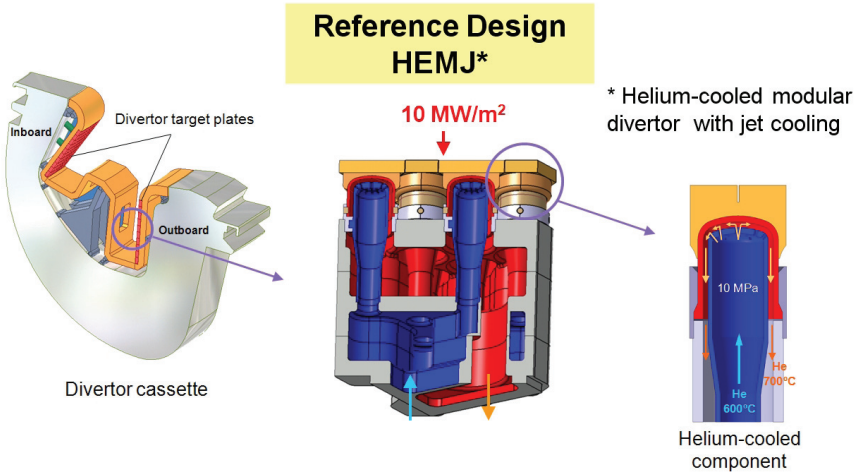

Figure 2.1. Scheme of the helium-cooled modular jet (HEMJ) concept for the European DEMO divertor [109]. The divertor requirement is to withstand a high heat flux of at least 10 MW·m^{-2}. The concept is based on small helium-cooled tungsten plasma-facing components (right) so-called fingers assembled into divertor target plates (left and middle).

components. Drawbacks of W are its high DBTT and low recrystallisation temperature, which restrict the designed operating temperature window of the material as structural part. However, the ductility of W can be increased by adding fine oxide particles to it. Thus, the alloy W-1%La_2O_3 (WL10) is regarded as a reliable option for the structural part of the divertor yet [107].

Each finger is made of five parts: the tile, the thimble, the conic sleeve, the supporting structure and the cartridge (figure 2.2). The tile is made from pure W and directly exposed to the plasma, acting as sacrificial layer and thermal shield for the heat sink or structural part located underneath, the thimble, made of W alloy (W-1%La_2O_3). The hexagonal shape of the tile is 18 mm wide and 5 mm thick, whereas the thimble, hollow in the inside, has a cylindrical shape with an outer diameter of 15 mm and a wall thickness of 1 mm. The purpose of designing two separate W parts is to stop at the interface between the tile and the thimble possible damages due to thermal stresses. This addresses, in particular, the propagation of cracks from the plasma-facing part to the heat sink part that would cause He leakage. Castellations with a width of 0.2 mm and a depth of 5 to 3 mm are machined in the tile to reduce thermal stresses during loads. The thimble is connected to the front plate of a supporting structure made of steel (oxide dispersion-strengthened reduced activation ferritic and martensitic steel in the design) with a sleeve locked mechanically around both the thimble and the supporting structure and secured by means of brazing or casting. A steel cartridge is then inserted inside of the hollow thimble. There are 24 holes in the cap of the

cartridge, which acts as a sprinkler head (each hole has a diameter of 0.6 mm, except the one at the center which has a diameter of 1 mm). The distance between the top of the cartridge and the thimble is 0.9 mm [107]. The cartridge (in particular the dimension of the holes) was the object of careful thermohydraulic analysis [110, 111]. The finger has a height of about 30 mm and a width of about 20 mm [112]. The components are cooled through the cartridge by He jets (10 MPa, 600°C) impinging on the inner surface of the thimble [113]. The design and its evolution was described in detail elsewhere [114].

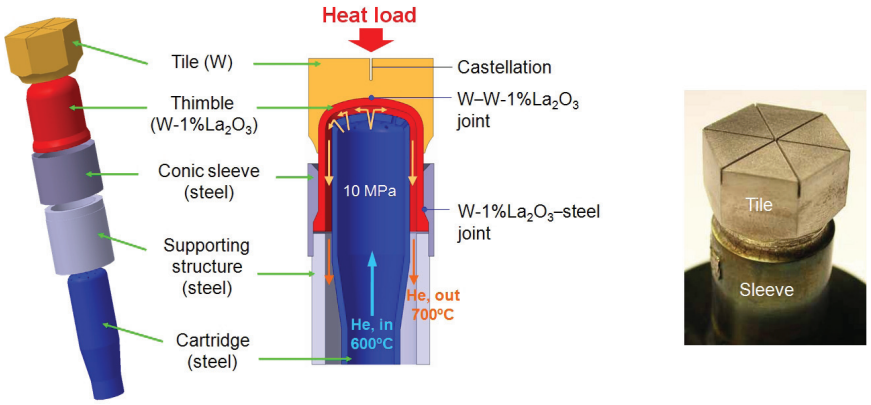

Figure 2.2. (Left) Scheme of the finger design and (right) view of a component fabricated according to this design [115]. The tile (pure tungsten) directly facing the plasma acts as a thermal shield for the structural or heat sink part below, the thimble (tungsten alloy, W-1%La_2O_3), which is cooled by helium jets through a steel cartridge impinging on the thimble's inner surface.

Computational fluid dynamics (CFD) simulations showed that for the nominal case of components exposed to a power density of 10 $MW{\cdot}m^{-2}$ and cooled by He with an internal pressure of 10 MPa and a mass flow rate (MFR) of 6.8 $g{\cdot}s^{-1}$, the yielded maximum temperatures in the tile and the thimble were about 1700°C and 1170°C respectively (figure 2.3).

2.3 Fabrication of divertor modules

For design verification and proof-of-principle, several modules were manufactured and tested under high heat flux. The R&D on the technologies for the shaping of the W parts (tile and thimble) and the joining (of W to W-1%La_2O_3 and W-1%La_2O_3 to steel) were performed at the Karlsruhe Institute of Technology (KIT) in Karlsruhe, Germany, and at D.V. Efremov Scientific Research Institute of Electrophysical Apparatus (NIIEFA) in St. Petersburg, Russia [107, 117–120].

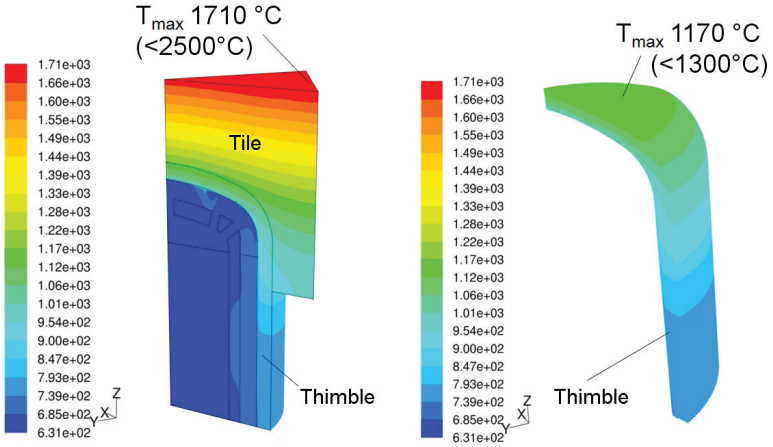

Figure 2.3. Temperature distributions in the tile and the thimble calculated by computational fluid dynamics (CFD) simulations under the following conditions: power density 10 $MW \cdot m^{-2}$, helium gas' internal pressure and mass flow rate of 10 MPa and 6.8 $g \cdot s^{-1}$ respectively [116].

2.3.1 Material selection

The pure W and W-1%La_2O_3 materials (for tile and thimble respectively) were produced by powder metallurgical routes that typically end with the deformation by forging or rolling of the sintered blanks into rod- or plate-like geometries. The deformation processes induce preferential grain orientations as illustrated below (figure 2.4).

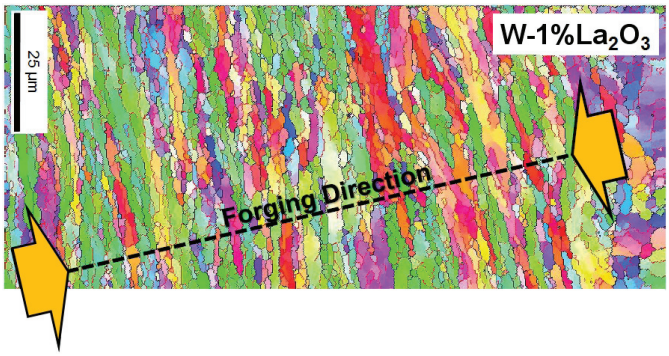

Figure 2.4. EBSD micrograph of the cross section of a W-1%La_2O_3 forged rod [121]. The microstructure showed a preferential grain orientation characteristic of the deformation process (here forging).

Typically cracks in W occur and propagate along the grain boundaries. The cracking behaviour depends on the orientation of the heat flux with respect to the grain orien-

tation. Hereby the performance of the modules was investigated with respect to the grain orientation of the plasma-facing material (for the tile) that was either parallel or perpendicular to the heat flux (the grain orientation of the structural material for the thimble was always parallel to the heat flux).

Here, the materials were forged rods (pure W and W-1%La_2O_3) provided by Plansee AG (Austria) or JSC Polema (Russia) or rolled plates provided by JSC Polema only. The cutting scheme of the materials for the armour with respect to the grain orientation is shown in figure 2.5. They were then shaped using machining techniques, namely turning, milling and electric discharge machining (EDM) [122, 123]. A surface finishing, namely mechanical grinding, was applied to most of the W parts to remove any defect induced by the above-mentionned machining processes.

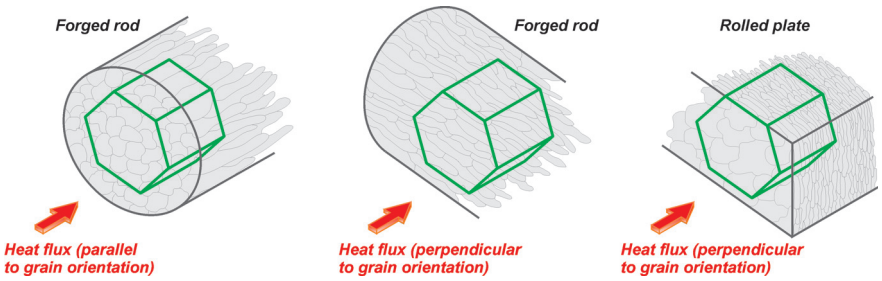

Figure 2.5. Sketches of the cutting schemes for the plasma-facing part with respect to the material's grain orientation. The heat flux (indicated by the red arrow) was applied either parallel (forged rod materials) or perpendicular (forged rod and rolled plate materials) to the grain orientation.

2.3.2 Joining technology

The joining of the parts (tile to thimble and thimble to supporting structure) was performed as follow: first the brazing (or casting) of the thimble and sleeve and then the brazing of the tile and thimble. The latter was performed with a nickel (Ni) alloy filler metal, STEMET® 1311 (Ni-based, 16.0 cobalt (Co), 5.0 iron (Fe), 4.0 silicon (Si), 4.0 boron (B), 0.4 chromium (Cr)) with a brazing temperature of 1050°C, or with a Cu-based alloy filler metal, CuNi44 with a brazing temperature of 1300°C. For the joining of the thimble to the conic sleeve, either Cu casting or brazing with a cobalt (Co) alloy filler metal, 71KHCP® (Co-based, 5.8 Fe, 12.4 Ni, 6.7 Si, 3.8 B, 0.1 manganese (Mn)) with a brazing temperature of 1100°C, was used.

Table 2.1 summarizes the fabrication matrix of the components along with the detailed testing parameters.

2.4 Testing under cyclic thermal loads

After fabrication the divertor modules were tested under steady-state thermal loads in the electron beam facility TSEFEY (figure 2.6) [124–126], which has a maximum beam power of 200 kW and an acceleration voltage of 40 kV. For the beam guidance a TV-like scanning mode was used with frequencies of 0.2 and 0.5 kHz in x- and y-direction respectively. Because of the large beam diameter (20 mm) the power was not only deposited on the component itself but also on a beam dump in a plane immediately below the component. The absorbed power density was measured by water calorimetry. A digital camera and an infrared camera were used to measure surface temperatures above and below 600°C respectively while a two-color pyrometer was available for temperatures above 900°C. A He loop was connected to the facility to ensure the cooling of the modules by He. The He mass flow rate was gained from a measurement of pressure drop over a defined hole.

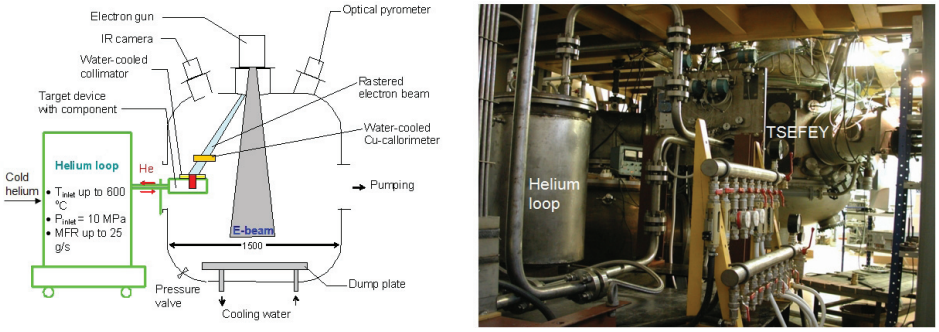

Figure 2.6. (Left) Scheme and (right) view of the electron beam facility TSEFEY connected to a helium loop used for the testing of the components under high thermal loads [109]. It has a maximum beam power of 200 kW and an acceleration voltage of 40 kV.

The modules were exposed to power densities in the range of 5 to 13 $MW \cdot m^{-2}$. The He parameters were an internal pressure of 10 MPa, inlet and outlet temperatures in the range of 495 to 635°C, and a MFR in the range of 9 to 13 $g \cdot s^{-1}$. The cyclic thermal loading was simulated by switching the beam on and off periodically. The cycle duration was 60 s (typically 30 s beam on and 30 s beam off). A few components were tested with a so-called "soft ramp" during which the power was increased slowly for 20 s until it reached the desired power density, then maintained for 20 s, then decreased for 20 s and finally shutdown for 20 s. The "soft ramp" had no impact on the modules' performance [109]. The testing parameters per module are listed in table 2.1.

Component number	Power density ($MW \cdot m^{-2}$)	Cycle number	Helium mass flow rate ($g \cdot s^{-1}$)	Helium inlet/outlet temperature (°C)	Helium pressure loss (MPa)
5(a)*	9	(i) 100, (ii) 24	(i) 13,5, (ii) 7,2	(i) 580/600, (ii) 605/635	(i) 0.29, (ii) 0.08
11(b)*	not tested	-	-	-	-
12(b)*	10	18	9-10	560/610	0.2
13(c)	9	70	9	570/620	0.19
14(c)	9	90	9	560/610	0.17
16(c)*	not tested	-	-	-	-
17(b)	10	89	9	570/620	0.18
21(b)	9.5	100	13	550/590	0.35
24(d)	10	45	9-13	530/595	0.16-0.35
26(d)	not tested	-	-	-	-
29(e)	(i) 11, (ii) 12, (iii) 12-14	(i) 20 , (ii) 12, (iii) 7	13	495/550	0.30
32(f)	10	10	11-13	550/590	0.25-0.35

*surface finishing was not applied

	W material	W grain orientation	W-1%La_2O_3 material	W/W-1%La_2O_3 joint	W-1%La_2O_3/steel joint
(a)**	Polema forged rod	Parallel to the heat flux	Plansee forged rod	Nickel-based (STEMET® 1311)	Cobalt-based (71KHCP®)
(b)	Plansee forged rod	Parallel to the heat flux	Plansee forged rod	Nickel-based (STEMET® 1311)	Cobalt-based (71KHCP®)
(c)	Plansee forged rod	Parallel to the heat flux	Plansee forged rod	Nickel-based (STEMET® 1311)	Copper casting
(d)	Polema forged rod	Perpendicular	Plansee forged rod	CuNi44	Cobalt-based (71KHCP®)
(e)	Polema rolled plate	Perpendicular	Plansee forged rod	Nickel-based (STEMET® 1311)	Cobalt-based (71KHCP®)
(f)	Polema rolled plate	Perpendicular	Plansee forged rod	CuNi44	Cobalt-based (71KHCP®)

**no castellations in the tile

Table 2.1. Testing parameters of the helium-cooled divertor modules and material selection for their fabrication.

2.5 Results

2.5.1 Plasma-facing part

During testing cracks occurred in the loaded surfaces due to thermally induced mechanical stresses, too high compared to the strength of W materials (figure 2.7). The fracture mode was cracking by tensile forces (as described in section 1.7). The crack distance was in the range of the grain width (∼100 μm). The ground surfaces were easily recognisable as they showed a smooth aspect even after thermal loads (figure 2.7(a)) whereas the as-machined surfaces appeared rougher (figure 2.7(b)). Thus, the grinding process did not prevent crack formation by thermal fatigue. In addition to cracking the components #14 and #32 (table 2.1) showed surface melting; the grains were molten individually (figure 2.7(c)). Surface melting was related to a defective bond between the

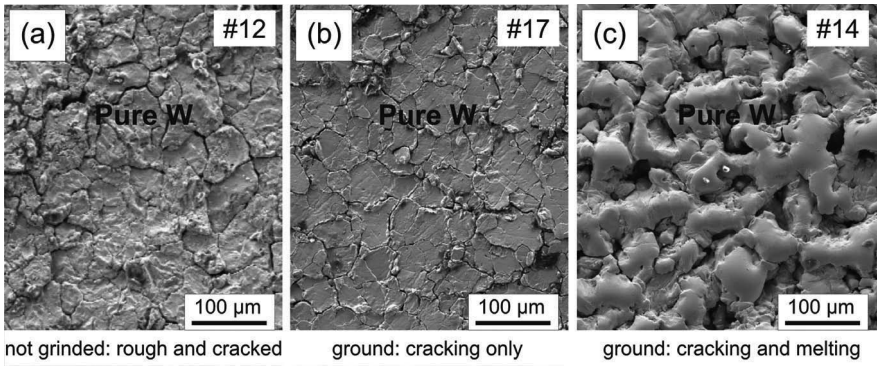

Figure 2.7. SEM micrographs of the loaded surfaces after (a) 18 cycles at 10 MW·m^{-2}, (b) 89 cycles at 10 MW·m^{-2} and (c) 90 cycles at 9 MW·m^{-2} showing cracks due to thermal stresses. A few components showed surface melting on top of surface cracking due to a defective bond between the plasma-facing and heat sink parts.

plasma-facing and heat sink parts that led to partial or complete detachment of the tile from the thimble. Complete detachment led to significant crack opening (figure 2.8).

The examination of the cross section of the loaded surfaces revealed that cracks induced by thermal fatigue formed dense crack networks in the plasma-facing part (figure 2.9).

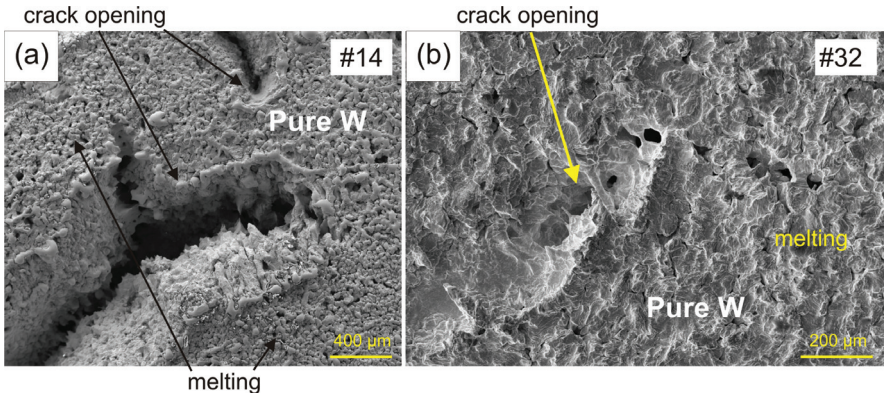

Figure 2.8. SEM micrographs of the loaded surfaces area after (a) 90 cycles at 9 MW·m^{-2} and (b) 10 cycles at 10 MW·m^{-2} showing surface melting and significant crack opening due to overheating of the plasma-facing part after its detachment from the heat sink part.

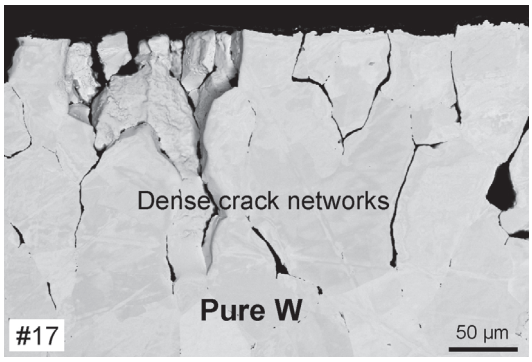

Figure 2.9. BSE micrograph of the cross section of the loaded area after 89 cycles at 10 MW·m^{-2}. Cracks induced by thermal stresses in the plasma-facing parts propagated and formed dense crack networks.

The crack depths in components #12, #13, #17 (table 2.1) were about 118, 163, 180 μm respectively. The crack depth showed a tendency to increase with the cycle number among the components tested with a He MFR of 9 to 10 g·s^{-1} (figure 2.10). The crack depths in components #5 and #21 (table 2.1) were shallower (43 and 69 μm respectively) although they were tested at higher cycle numbers (more than 100 cycles). It indicated that the increase of the mass flow rate (from 9 to 13 g·s^{-1}) led to a decrease of the crack depth. The higher the mass flow rate, the greater the cooling efficiency. Consequently, the surface temperature during the thermal loading was lower and so were the thermal stresses. Therefore, the decrease of the operation temperature prevented the crack development to a certain extent. The crack depths of the components #14, #24 and #32 (table 2.1) were not measured because these components showed

a particularly severe failure mode related to joining issues between the plasma-facing and heat sink parts.

Among the components tested with a He MFR of 13 $g \cdot s^{-1}$, component #5 (with a tile made of a Polema W rod) showed a lower crack depth compared to component #21 (with a tile from a Plansee W rod). The behaviour of the Polema W has to be rated even higher based on the fact the tile of component #5 had no castellation slots, implying greater thermal stresses, and was subjected to a higher cycle number than the tile of component #21. This difference in terms of crack depth and crack density showed that the resistance to crack propagation depended on the W grade.

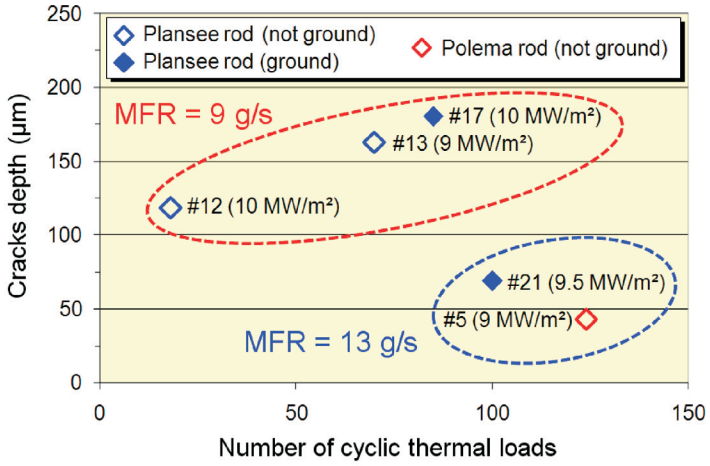

Figure 2.10. Crack depth in the plasma-facing part as a function of the cycle number. Among the components tested with a helium mass flow rate (MFR) of 9 to 10 $g \cdot s^{-1}$, the crack depth showed a tendency to increase with the cycle number. The increase of the MFR enhanced the cooling efficiency, reduced the thermal stresses and minimised the crack propagation in the loaded surface.

Due to differences in terms of testing parameters (cycle number, power density and mass flow rate) and material selection between the divertor modules, the impact of the surface finishing on the crack development could not be accurately determined.

The cracks induced by thermal stresses propagated along the grain boundaries. Thus, in the rods with a grain orientation parallel to the heat flux the cracks followed the direction of the grain orientation and propagated perpendicular to the loaded surface, towards the heat sink (figure 2.11(a)-(c)). The W plate used for the tile of the component #29 (table 2.1) surprisingly showed no particular grain orientation. Consequently, the cracks were remarkably shallow although the component was tested at a relatively high power density (14 $MW \cdot m^{-2}$) (figure 2.11(d)).

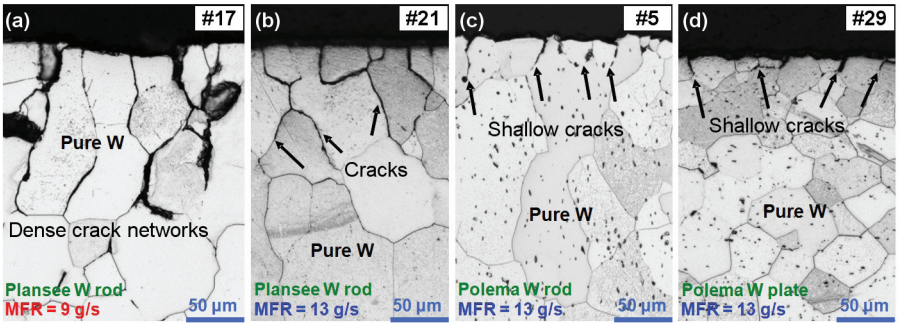

Figure 2.11. BSE micrographs of the cross sections of the loaded surfaces after (a) 89 cycles at 10 $MW{\cdot}m^{-2}$, (b) 100 cycles at 9.5 $MW{\cdot}m^{-2}$, (c)124 cycles at 9 $MW{\cdot}m^{-2}$, and (d) 39 cycles up to 14 $MW{\cdot}m^{-2}$. At the same helium mass flow rate (13 $g{\cdot}s^{-1}$) Polema materials (rod and plate) showed better resistances to crack propagation compared to Plansee materials.

The as-machined components #11 and #16 (table 2.1) showed discrete microcracks that occurred in the surfaces (contours and castellations) of the plasma-facing part during machining. These microcracks resulted from stresses due to the rapid heating and cooling effects induced by the discharges during the EDM process [127]. The crack depth was typically about 30 μm (figure 2.12).

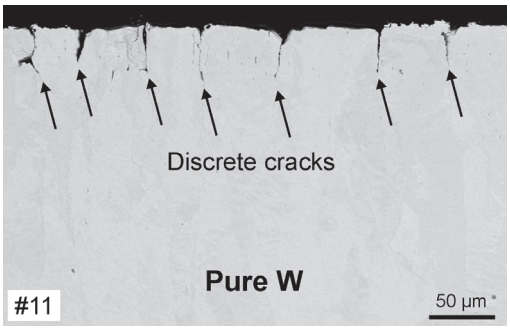

Figure 2.12. BSE micrograph of the cross section of the as-machined plasma-facing part (e.g. component #11) showing microcracks induced in tungsten surfaces by electric discharge machining (EDM).

As the grinding process removed 0.2 mm thick W layers, it also removed the discrete cracks induced by EDM except in the castellations that were too narrow (0.2 mm large) to allow any finishing tool to penetrate in-between (figure 2.13(a)). In the tested components, defects were observed on top of cracks in regions close to the castellations (figure 2.13(b)). Those defects could be related to pre-existing defects (e.g. cavities) in the raw W materials (i.e. rods and plates) that developed under thermal loads. It could also be related to machining-induced defects that developed by thermal stresses. Or the combination of both.

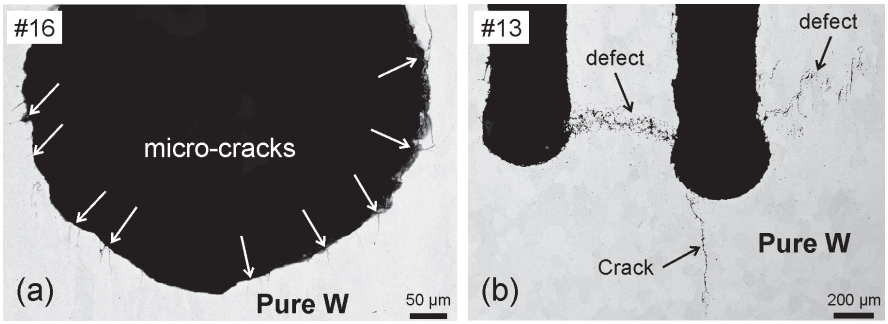

Figure 2.13. BSE micrographs of the cross sections of the tile (a) after machining and (b) after 70 cycles at 9 MW·m^{-2} showing microcracks in the castellations' surfaces induced by EDM and cracks as well as defects in the same region respectively. The microcracks induced by EDM could have grown and futher damaged the components during thermal loads.

2.5.2 Structural-heat sink part

At the edge of the joint between the plasma-facing (tile) and the structural (thimble) parts brazed with the Ni-based filler metal (STEMET® 1311), cracks occurred inside of the as-machined brazing layer due to residual stresses and propagated in the W materials (figure 2.14(a)). During thermal loads, a multi-phase formed at the joint's interfaces (figure 2.14(b)) and grew up with increasing the cycle number (figure 2.14(c)). The energy-dispersive X-ray (EDX) spectroscopy of the multi-phase showed W mixed

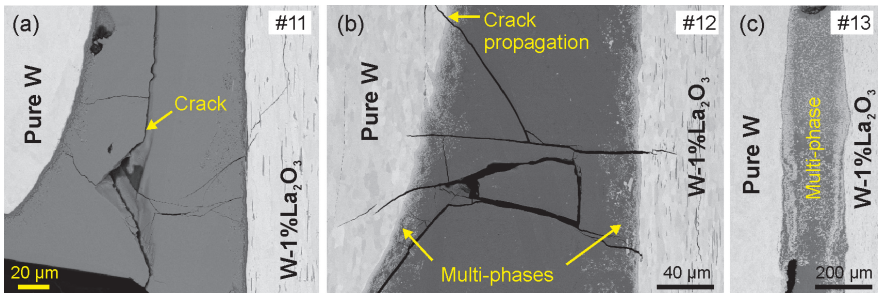

Figure 2.14. BSE micrographs of the cross sections of the tile-thimble joint (edge) brazed with the nickel-based filler metal (a) before testing, (b) after 18 cycles at 10 MW·m^{-2} and (c) 70 cycles at 9 MW·m^{-2}. Cracks occurred in the as-machined brazing layer and propagated in the tungsten-based materials. In addtion, a multi-phase occurred at the joint's interfaces during thermal loads.

with elements contained in the brazing metal, namely Ni, Si, Fe, and Co (figure 2.15). Thus, the multi-phase resulted from a metallurgical reaction between the tungsten-based materials and the brazing metal.

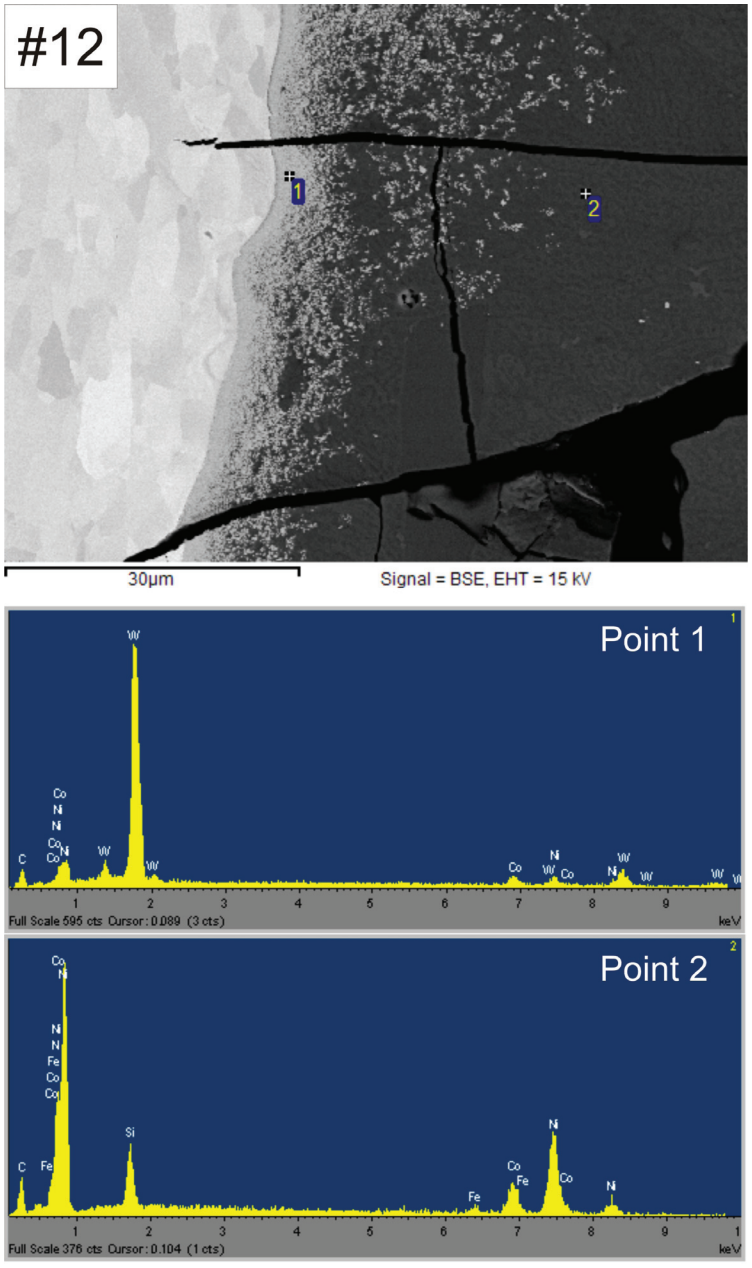

Figure 2.15. (Top) BSE micrograph of the cross section of the tile-thimble joint (edge) after 18 cycles at 10 $MW \cdot m^{-2}$ and (bottom) EDX analysis of the brazing layer. The multi-phase that contained tungsten and elements of the nickel-based brazing metal (Ni, Si, Fe, Co) resulted from the metallurgical reaction between the tungsten-based materials and the brazing metal.

In the middle of the same joint (near the top of the thimble) this multi-phase was also observed but in addition there was a large cavity after thermal loads (figure 2.16). For a

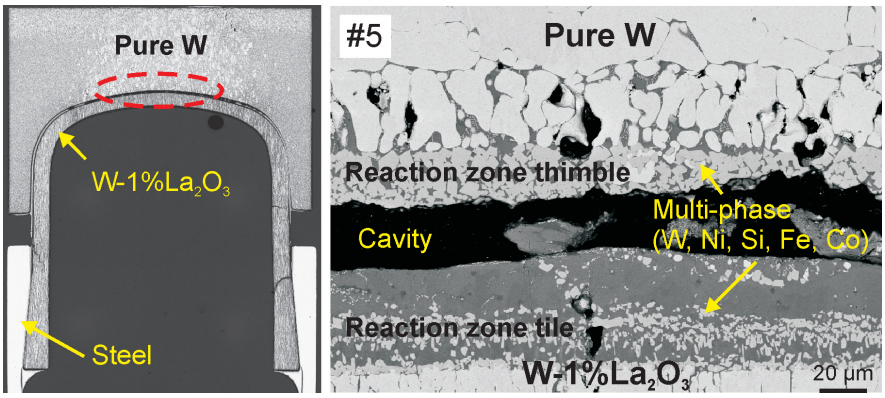

Figure 2.16. (Left) Optical micrograph of the cross section of the divertor module after 124 cycles at 9 MW·m^{-2} showing a gap in the tile-thimble joint (in the red dotted circle) that formed after the leak of the nickel-based brazing metal. (Right) BSE micrograph showing a closer view of the brazing layer with the cavity as well as an intermetallic phase formed after the reaction of the tungsten-based materials with the brazing material.

power density of 10 MW·m^{-2} and a MFR of 6.8 g·s^{-1} the temperature in this region of the joint was calculated about 1170°C (figure 2.3 in section 2.3), higher than the brazing temperature of the filler metal (1050°C) that melted and leaked away. Furthermore, the plasma-facing part was covered by a layer that had a typical aspect of re-solidified structure (figure 2.17). The EDX analysis of the layer enabled to identify traces of Ni, Co, Fe and Si (grey contrasts), which composed the brazing metal, forming different brittle phases with the W material (the bright contrast). Therefore, the cavity in the joint, characteristic of the tested components, resulted from the loss of the brazing metal after its migration through the tile by capillary forces, towards the top surface. In addition, a hole (with a diameter of 60 μm) was observed in the re-solidified brazing layer covering the plasma-facing part (figure 2.18(a)). This hole characterised by a smooth outline formed after the erosion of cracks by the molten Ni-based brazing metal. During its migration towards the top surface the liquid brazing metal eroded W and led after cooling down to that top surface layer containing the same multi-phase as that observed in the tile-thimble joint (figure 2.18(b)). The thickness of the re-solidified layer reached hundreds of μm (figure 2.18(c)).

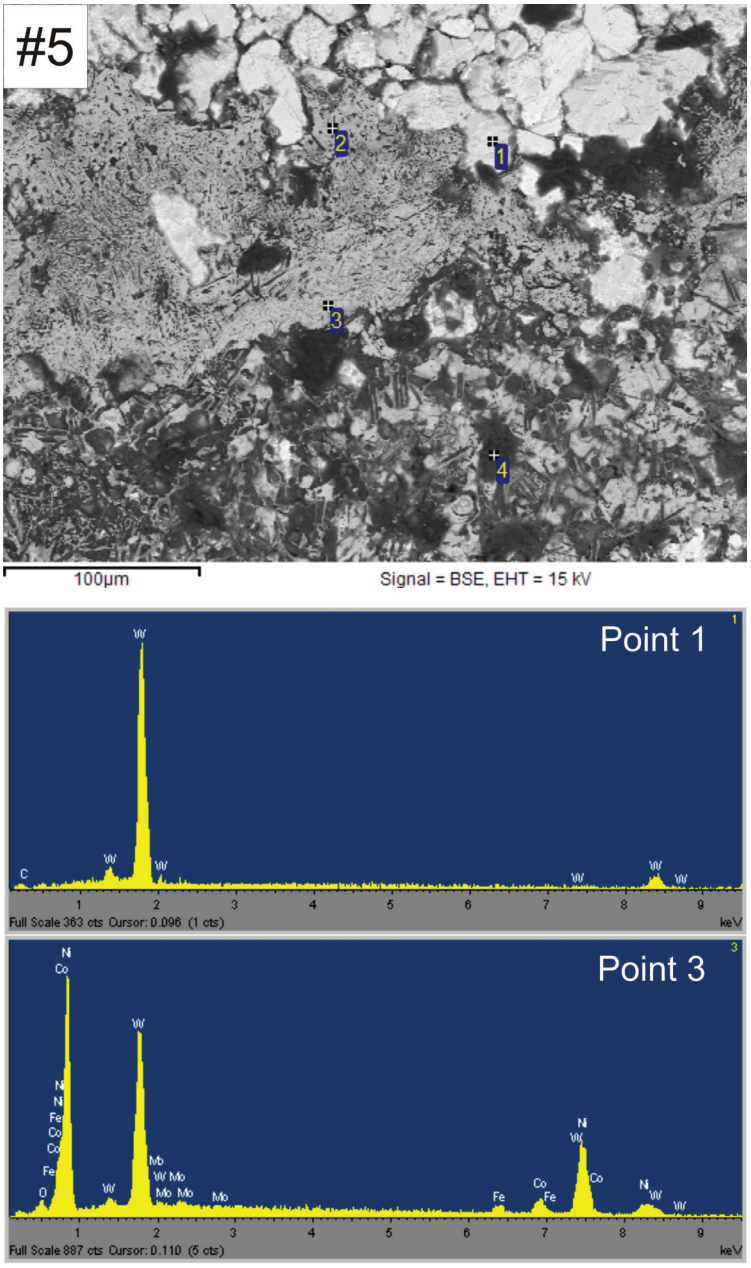

Figure 2.17. (Top) BSE micrograph of the loaded surface after 124 cycles at 9 MW·m^{-2} showing a re-solidified layer and (bottom) EDX analysis of this layer revealing W and brazing metal elements (Ni, Co, Si, Fe). The plasma-facing part was covered by the nickel-based brazing metal that melted, migrated through the tile to the top surface and re-solidified on it.

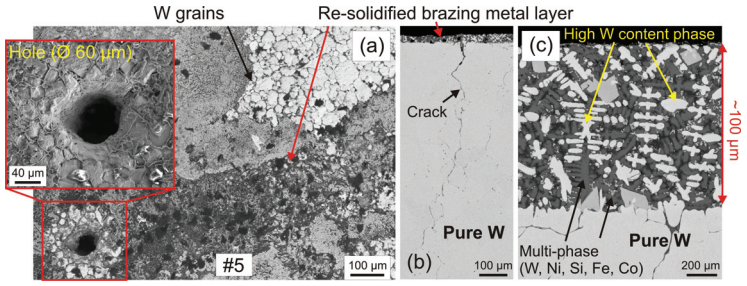

Figure 2.18. (a) SEM micrograph of the loaded surface after 124 cycles at 9 MW·m^{-2} showing a hole that resulted from the erosion of cracks by the molten nickel-based brazing metal. (b) and (c) BSE micrographs of the cross section of this region showing a multi-phase in the re-solidified layer resulting from the dissolving of tungsten in the brazing metal.

The Ni-based brazing filler metal led to a noticeable degradation of the components after it melted during the cyclic thermal loading. Its melting point was too low with regard to the calculated average operation temperature in the tile-thimble joint (∼1170°C) . The brazing filler metal CuNi44 that has a higher brazing temperature (1300°C) was used as an alternative. Like STEMET® 1311, CuNi44 led to the formation of a multi-phase in the as-machined brazing layer due to the reaction of the W-based materials with the Ni contained in the brazing metal (figure 2.19). The

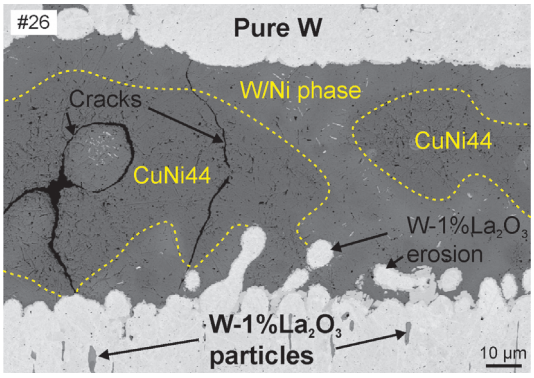

Figure 2.19. BSE micrograph of the cross section of the as-machined tile-thimble joint brazed with the copper-based brazing metal (CuNi44). The reaction between the tungsten-based materials and the nickel contained in the brazing metal led to the formation of a multi-phase (the light grey contrast between the dotted lines) before thermal loads already.

analysis of the braze layer by EDX identified a multi-phase containing W and Ni. Furthermore, cracks also occurred in the CuNi44 as-machined brazing layer due to residual stresses.

Beside the multi-phase a large cavity occurred probably due to improper filling of the gap between the tile and the thimble during the brazing procedure (figure 2.20(a)). Consequently, cavities were also observed after thermal loads (figure 2.20(b)). Such cavities appeared systematically in the few components brazed with CuNi44 components, provoking their early (i.e. at small cycle number) failure (less than 50 cycles and 10 cycles only for components #24 and #32 respectively) or their exclusion from the testing campaign (e.g. component # 26). At the edge of the joint there were no cavities but large cracks occurred inside of the brazing layer of the tested components (figure 2.20(c)).

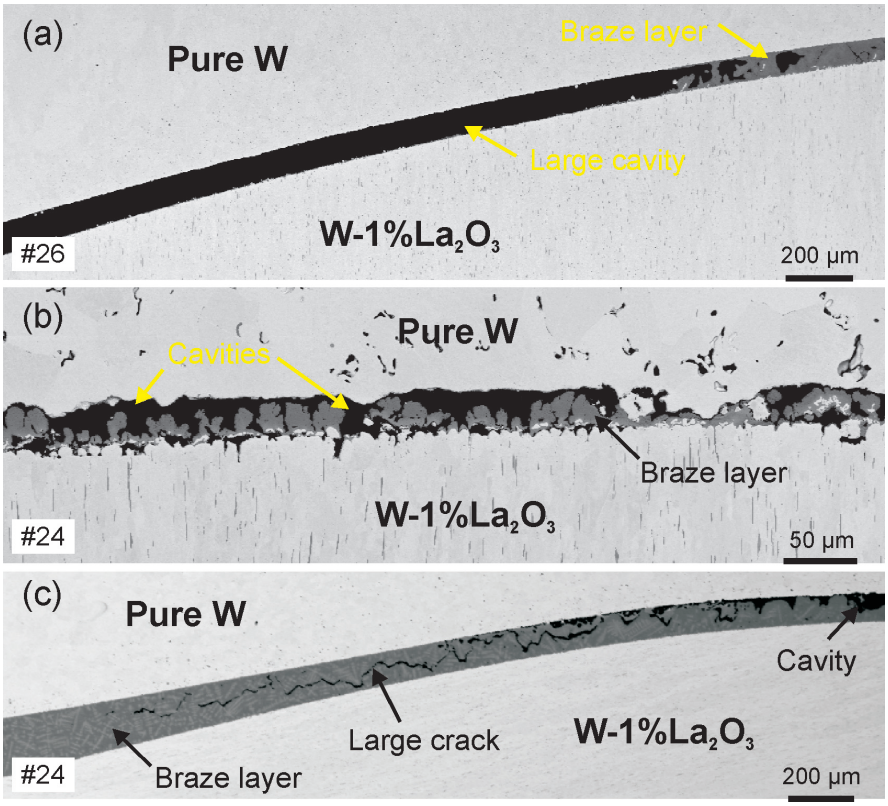

Figure 2.20. BSE micrographs of the cross sections of the tile-thimble joint performed with CuNi44 (a) as-machined showing a gap due to an improper filling during the brazing process, (b) and (c) after 45 cycles at 10 $MW{\cdot}m^{-2}$ showing cavities (middle of the joint) and large cracks (edge of the joint).

The cavities in the tile-thimble joint, regardless of the brazing material, acted as thermal barriers and caused the overheating of the plasma-facing part during thermal loads therefore facilitating the crack development in the loaded surface. Below the joint, on the thimble's inner surface cooled by He during thermal loading, the thick oxide layer

(∼60-100 μm) that formed from the residual oxygen in the helium coolant loop also acted as a thermal barrier. Such remarkable thickness of the oxide layer in this short time indicated that the operation temperature was high or there was a high residual oxygen content. Furthermore, cracks occurred both along and across the grain orientation of the W-1%La_2O_3 material, creating a path for the helium gas (figure 2.21). Thereby, the crack propagation was probably facilitated by the strong anisotropic microstructure of the W alloy material.

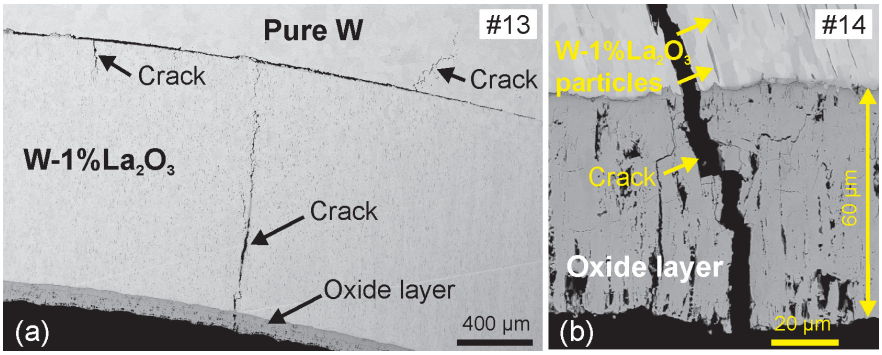

Figure 2.21. BSE micrographs of the cross sections of the structural heat sink part (a) after 70 cycles at 9 MW·m^{-2} and (b) 90 cycles at 9 MW·m^{-2} showing an oxide layer covering the inner surface of the thimble. Cracks occurred in both the oxide layer and the thimble creating a path and the leakage of helium gas.

2.5.3 Tungsten-steel interface

At the upper edge of the joint between the thimble and the conic sleeve (figure 2.22(a)), the brazing (or casted) layer formed a conical shaped solid ring on top of the sleeve (figure 2.22(b)). After thermal loads, large cracks appeared inside of the brazing layer as well as in the thimble (figure 2.22(c)). In this region the mismatch between the coefficients of thermal expension (CTE) of the materials is large (∼4-6·10^{-6} K^{-1} for W-1%La_2O_3 and ∼10-14·10^{-6} K^{-1} for steel in a temperature range between 20 and 1000°C) [118] and so were the cracks.

As observed in the joint between pure W and W-1%La_2O_3, intermetallic phases, mainly Fe-Cr-W, formed also in the joint between W-1%La_2O_3 and steel (figure 2.23).

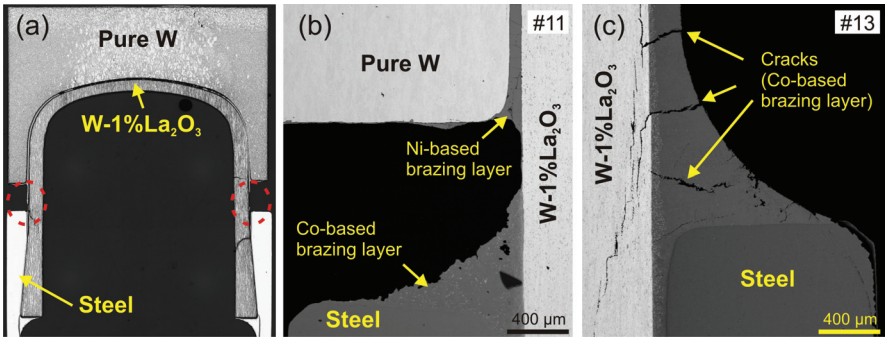

Figure 2.22. (a) Optical micrograph of the cross section of the divertor module (e.g. component #5) showing the upper edge of the joint between the thimble and the conic sleeve (in of the red dotted circles). (b) and (c) BSE micrographs of this region showing respectively small defects in the as-machined brazing layer and large cracks in both the brazing layer and the thimble after 89 cycles at 10 MW·m^{-2}. The large crack width was probably related to the large mismatch of thermal expansion coefficients between the tungsten alloy and steel. In the thimble, cracks tended to follow the grain orientation of the material.

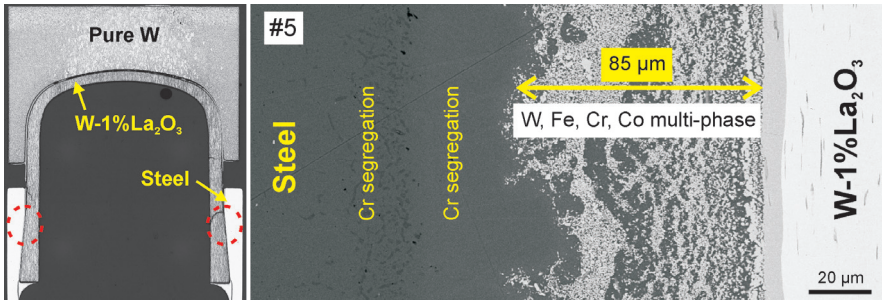

Figure 2.23. (Left) Optical micrograph of the cross section of the divertor module (e.g. component #5) showing the joint between the thimble and the supporting structure (in the red dotted circles). (Right) BSE micrograph of this region after 124 cycles at 9 MW·m^{-2} showing an intermetallic phase.

3 Performance of tungsten grades under steady-state thermal loads

3.1 Introduction

Tungsten (W) was selected as plasma-facing material (PFM) in the next-step fusion device ITER and the European design of DEMO due to its attractive thermo-mechanical properties, namely its high melting point, high thermal conductivity, low tritium inventory and low erosion rate under plasma loading [101]. In those devices, the materials will have to withstand thermo-mechanical stresses generated by a large number of cyclic steady-state heat loads (thermal fatigue loads) with a power density of several $MW \cdot m^{-2}$ as well as transient events (thermal shock loads) with a power density of a few $GW \cdot m^{-2}$ at low and high repetition rates. Former studies showed that the microstructural response at high temperatures as well as the thermal fatigue and the thermal shock resistance of W differ from one grade to another [128].

When produced by powder metallurgy W is going through many processes from mining to finished products, namely hydrogen reduction (of W oxide), die and cold isostatic pressing (of the W powder), sintering (of the pressed W blanks), and deformation (of the sintered blanks). Those steps are performed at specific temperature ranges. Many parameters, like the raw powder materials, the geometry of the densified blanks (rod or plate), the degree and the type of deformation of the sintered blanks (rolling, forging, swaging) and the working temperature have an impact on the microstructure (grain size, grain orientation, density) and the thermo-mechanical properties (strength, ductile-to-brittle transition temperature, recrystallisation temperature) of the achieved material [129]. Consequently, the performance of W under high thermal loads varies depending on the production history, as illustrated in chapter 2 (the inspection of the W components for the European DEMO divertor) with the observation of different cracking resistances depending on the provenance of the W grade (Plansee or Polema).

The combination of material suppliers and production routes leads to a strong variation of commercially available W grades. There is a lack of data with respect to the lifetime of W under fusion relevant loading conditions. The variation of the performance observed between the Plansee and the Polema W grades was based on the comparison of a few components only. To make a qualitative and quantitative statement a statistical approach is required. For this purpose, a W qualification program was performed

at FZJ and was focused on the evaluation and the comparison of the performance of pure W grades under fusion relevant thermal loads. This included the design and the fabrication of actively cooled components, the material characterization, the metallographic failure mode analysis, the thermo-mechanical finite element (FE) analysis, and the testing of materials under the combined thermal load (transient and steady-state thermal loads).
Furthermore, to investigate the impact of process induced surface modifications on the material's performance, both specimens with cracked and defect-free (i.e. mirror polished) surfaces were included within the tests.

3.2 Materials selection

The W materials selected for this study were produced by Plansee or Polema using the powder metallurgical process. Tungsten products achieved by powder metallurgy are highly pure (99.95% and above 99.97% in purity for Polema and Plansee products respectively). Powder metallurgy includes several steps described in figure 3.1. Once mined, minerals are filtered to obtain W oxides which are then reduced to obtain W powder. Steps to extract W oxides from ores are described in detail elsewhere [130]. After reduction, alloying and mixing, W powders are densified to various plate and rod geometries, predominently by die pressing and cold isostatic pressing. Pressed compacts are then sintered. Finally, the sintered blanks are deformed before being annealed. Several processes such as swaging, forging, and rolling, might be employed for the deformation of the blanks.

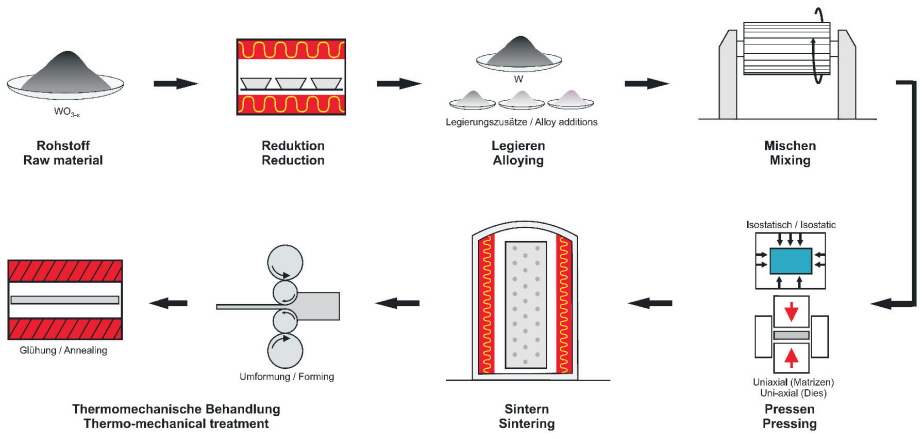

Figure 3.1. Scheme showing the steps of the powder metallurgy process employed for the production of the tungsten grades [130].

The combination of several powders, deformation (or forming) processes and product geometries results in various material's microstructures, in particular the deformation

processes induce a strong microstructural modification, an elongation (or deformation) of the grains along one or two orthogonal directions (figure 3.2). The grain orientation is an important parameter as it has a clear impact on the response of the material under thermal loads [128].

Materials investigated in this work were rods and plates deformed either by forging or rolling. All four Plansee materials were forged rods each with a specific diameter: 12, 30, 60 or 80 mm. The Polema materials were a forged rod with a diameter of 30 mm and two plates, one deformed by forging and one deformed by rolling, both 25 mm thick. Samples were cut with the top surface (the loaded surface) perpendicular to the grain orientation (i.e with the heat flux parallel to the grain orientation) as shown in figure 3.2.

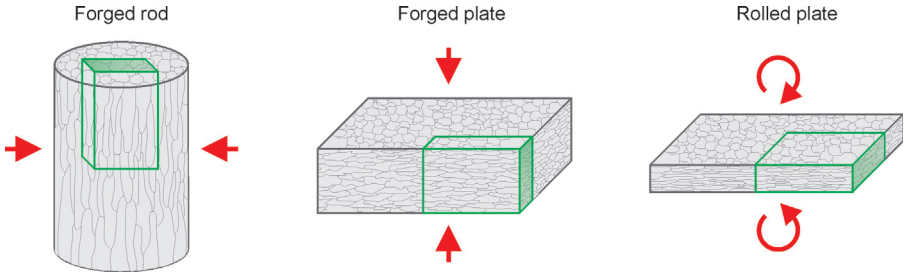

Figure 3.2. Sketches of typical tungsten microstructures for rod and plate geometries after forging and rolling. The cutting scheme of the samples is indicated by the top surface drawn as a shaded hexagon.

Materials characterization

The grain area was measured on the top surface and side (or cross section) of the samples. To do so, several pictures of the surfaces were taken after etching of the samples and transparent foils were put on the pictures to reproduce the microstructures with a pencil. The foils were then scanned in a computer where the grain areas were calculated numerically. The numerical processing also gives an aspect ratio A (A=1 corresponds to a perfectly symmetrical shape of the grain). Average grain areas as well as aspect ratios are given in table 3.1.

As expected, the microstructures of the materials were anisotropic, except in the forged plate which showed no particular grain orientation. In the rods, the aspect ratio of the cross section was smaller than that of the top view indicating a strong deformation of the grains on the cross section (as shown in figure 3.2 above). Overall, the grain areas of the Plansee rods increased with the rod diameter. It has been observed that the Plansee 30 mm diameter rod was characterised by two distinct grain areas (it was not deformed homogeneously). The grain areas of the Polema materials were smaller.

Materials	Average grain area measured on the top surface (average/min/max in μm^2)	Aspect ratio top surface	Average grain area measured on the cross section (average/min/max in μm^2)	Aspect ratio cross section
Plansee rod Ø12 mm	780/42/6226	0.67	1137/99/3605	0.40
Plansee rod Ø30 mm	(1)821/28/3281-(2)5887/3142/33830	(1)0.64/(2)0.63	(1)2178/87/10543-(2)6785/243/25229	(1)0.25/(2)0.29
Plansee rod Ø60 mm	9134/627/29635	0.60	13206/1042/28640	0.37
Plansee rod Ø80 mm	16381/359/73073	0.58	63264/4741/18543	0.40
Polema rod Ø30 mm	1130/42/31978	0.60	893/103/3243	0.52
Polema forged plate	1399/14/52589	0.58	506/89/2242	0.48
Polema rolled plate	1431/23/37726	0.34	1239/89/6725	0.48

(1) small and (2) large grain areas of the material

Table 3.1. Average grain areas of the tungsten grades measured on the top surface and cross section of the samples. The Plansee 30 mm diameter rod showed two specific grain areas. Overall, the grain area increased with the rod diameter. The Polema materials showed smaller grain areas. The aspect ratios indicated anisotropic microstructures except in the forged plate, which showed no particular grain orientation. Thus, in the rods grains had no particular orientation on the top surface and were strongly deformed on the cross section, whereas the opposite was observed in the rolled plate.

Figure 3.3 shows the as-received microstructures of the investigated materials from the top surface and cross section views as well as the heat flux orientation with respect to the grain orientation. The heat flux was applied parallel to the grain orientation (perpendicular to the top surface) in the rods. As cracks induced in W materials typically propagate along the grain boundaries, therefore following the direction of the grain deformation, it was expected to study different cracking behaviours in rods and plates.

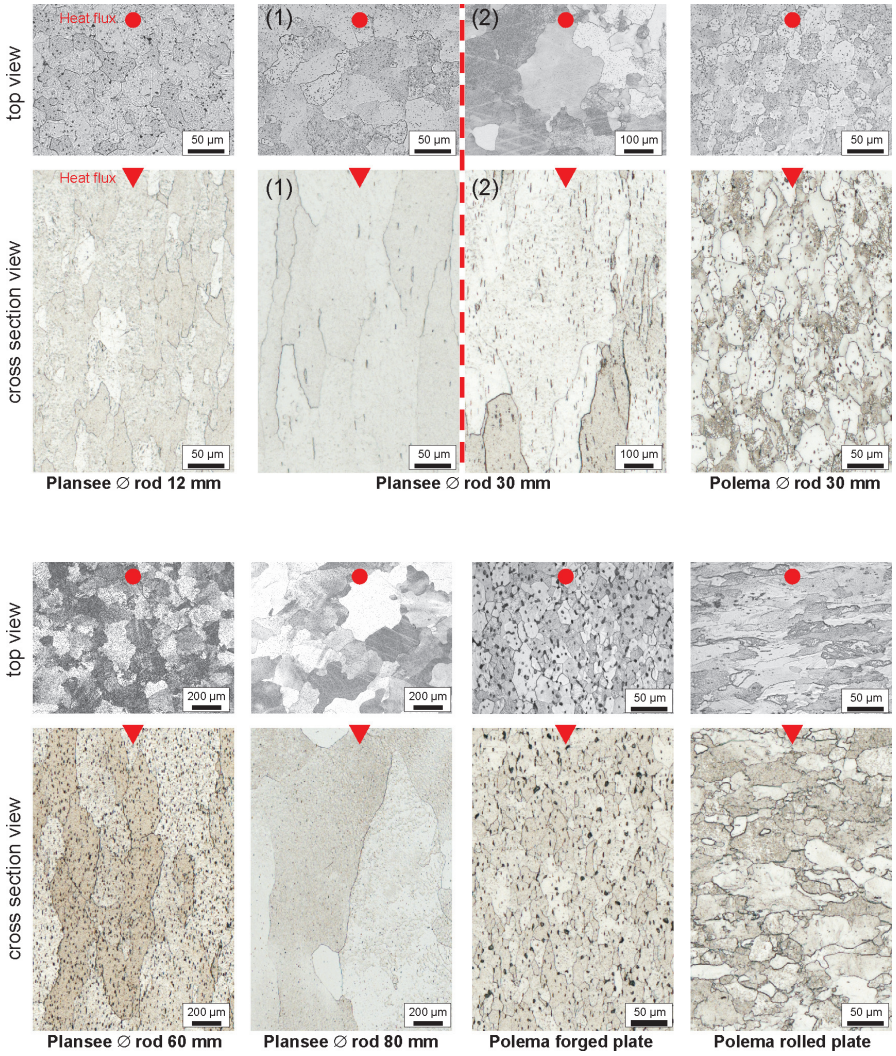

Figure 3.3. Optical micrographs (after etching) of the as-received microstructures from top surface and cross section views. The red dots and arrows represents the orientation of the heat flux, applied perpendicular to the top surface.

3.3 Components for testing under thermal loads

3.3.1 Design of the components

For the testing of the materials under steady-state thermal loads, the loading parameters were the cycle number and the various surface temperatures: ∼1200°C (ITER-designed surface temperature), ∼1600°C (surface temperature achieved in the European DEMO design) and ∼2000°C. All surface temperatures were achieved on one single component to avoid set-up variations from one component to another (when changing the cycle number) and to reduce the machine time, in particular the time required for the loading and unloading of the components in the testing facility. To achieve the different surface temperatures it was decided to modify the effective thickness of the samples (i.e. the distance between the sample's top surface and the heat sink interface) while keeping the power density in a defined range. Thus, each component included three sets of specimens, each set having a specific thickness corresponding to a specific surface temperature.

Calculations of the temperature gradients by Finite Element (FE) methods were performed for W sample's thicknesses (or heights) of 5, 10, and 15 mm (figure 3.4). The component modeled by FE calculation was identical to the one used experimentally (further shown in figure 3.8). The distance from the W-to-copper (Cu) interface to the center of the cooling tube (10 mm diameter) was 7 mm. The heat sink was cooled by water with a flow rate of 60 l·min^{-1}. Each set of blocks was loaded independently and within each set the loading was applied on all blocks simultaneously. For a power density of 15 MW·m^{-2}, calculated surface temperatures were about 792°C (h = 5 mm), 1462°C (h = 10 mm), and 2229°C (h = 15 mm), thus temperature gaps of 380°C, 138°C and 229°C (compared to the designed surface temperatures).

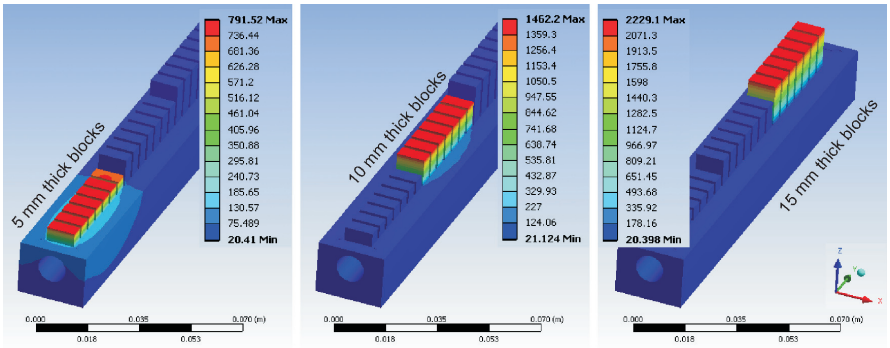

Figure 3.4. FE calculations of the temperature gradients obtained for a thermal load of 15 MW·m^{-2} in (left) 5 mm, (middle) 10 mm and (right) 15 mm thick blocks. The flow rate of the water cooling was 60 l·min^{-1}. The distance between the bottom of the blocks and the center of the cooling tube was 7 mm.

Higher temperatures were expected experimentally since the thermal contact between W and Cu was considered as perfect in the simulation. Therefore, it was decided to keep the specimen's thicknesses selected for the simulation (5, 10, and 15 mm) for the components' fabrication and to adjust the power density when necessary to achieve the desired surface temperatures.

3.3.2 Fabrication of the components

In total, three components were fabricated: component #1 for the testing of cracked surfaces and components #2 and #3 for the testing of defect-free surfaces at two cycle numbers. Surfaces are automatically cracked after cutting of the raw products (rods, plates) by electric discharge machining (EDM). For components #2 and #3 the cracks induced by EDM were removed by polishing.
The components #2 and #3 comprised all W grades (four from Plansee and three from Polema), whereas component #1 comprised the Plansee grades only (due to a lack of Polema materials). The allocation of W materials per component is shown in table 3.2.

Company	*Component #1	Block no.	Component #2	Component #3	Block no.
Plansee	rod Ø 12 mm	1	rod Ø 12 mm	rod Ø 12 mm	2
Plansee	rod Ø 30 mm	2	rod Ø 30 mm	rod Ø 30 mm	4
Plansee	rod Ø 60 mm	3	rod Ø 60 mm	rod Ø 60 mm	1
Plansee	rod Ø 80 mm	4	rod Ø 80 mm	rod Ø 80 mm	3
Polema	-	-	rod Ø 30 mm	rod Ø 30 mm	5
Polema	-	-	plate (forged)	plate (forged)	6
Polema	-	-	plate (rolled)	plate (rolled)	7

*the tungsten surfaces comprised cracks induced by machining

Table 3.2. Materials distribution per component. The block number refers to the position of the material on the plasma-facing component (see figure 3.8). In component #1, the surfaces of the materials were cracked. In components #2 and #3, the surfaces of the materials were defect-free.

The rods and the plates were cut by EDM in the form of small blocks with a base area of 5 by 10 mm^2 and various heights (5, 10 and 15 mm). The cutting scheme with respect to the grain orientation was shown in figure 3.2.

During exposure to steady-state thermal loads, the pulse duration lasts several tens of seconds and quasi-stationary thermal conditions are achieved on the surface of the material. To reach this thermal equilibrium in our tests, it was necessary to cool the materials with a heat sink (figure 3.5). The latter was a pure Cu block with dimensions of 109 mm (component #1) or 156 mm (components #2-3) in length, 24 mm in width and 30 mm in height. The high pressure coolant tube integrated in the Cu block had a diameter of 10 mm. The distance between the W-to-Cu interface and the center of the cooling tube was 7 mm. A shallow pool with a depth of 0.2 mm was grooved in the

top of the Cu block to accommodate the thin brazing filler metal foil for the joining process of the samples and prevent the brazing from flowing away when molten. The distances from the edges of the Cu block to the pool were 4 mm (small edge) and 5 mm (big edge).

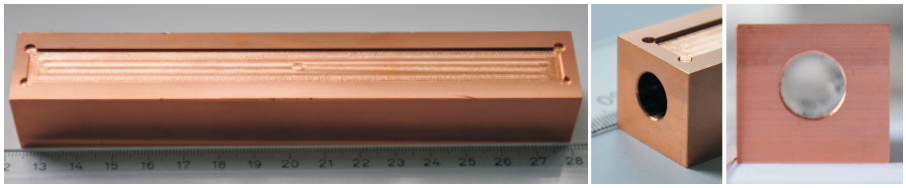

Figure 3.5. The heat sink made of pure copper used for the cooling of the samples. A shallow pool (0.2 mm deep) was grooved on the top surface to accommodate the brazing foil for the joining of the samples to the heat sink.

For the bonding of W to Cu four brazing filler metals were qualified: three Cu-based and one silver(Ag)-based, all in the form of foils except one Cu-based brazing metal in the form of powder. To qualify the brazing metals, three tests were performed: (1) wetting test of the brazing metal with Cu, (2) wetting test of the brazing metal with W, and (3) joining of W to Cu with the brazing metal. These tests were realized on

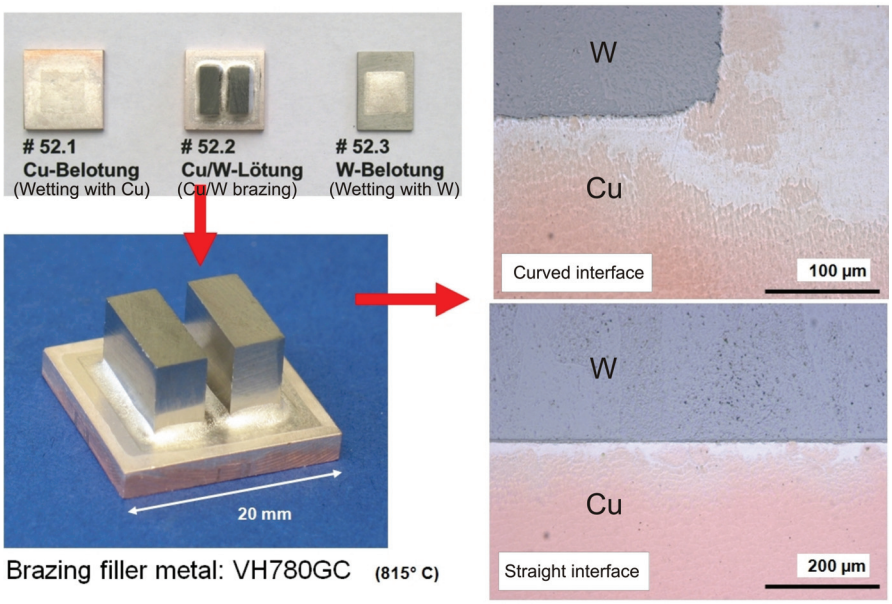

Figure 3.6. Test coupons for brazing studies, here with the silver-based brazing filler metal VH780GC. (Left) Wetting tests with copper and tungsten (#52.1 and #52.3 respectively) and joint of copper to tungsten (#52.2). (Right) optical micrograph of the cross sections of curved and straight interfaces of the joint.

small Cu and W plates with a section of 20 mm^2 and a thickness of 3 mm. The request of smooth wetting and sound joints were best met by VH780GC (Ag-based, 28.0 Cu, 2.0 Ge, 0.3 Ni; brazing temperature of 815 °C) shown in figure 3.6. Therefore, this brazing metal was selected for the joining of the samples to the heat sink.

A graphite holder was built to keep the W blocks in position during the brazing process (figure 3.7). The dimensions of the holder and sink were identical in length and width, except the holder's height was 10 mm. A rectangular hole with a length of 97 mm (component #1) or 144 mm (components #2-3) and a width of 10.4 mm was machined in the centre of the graphite block. On the inner surfaces of this hole, small slots (1 mm wide and 1 mm deep) were machined along the height of the holder to insert thin graphite plates (section: 12 by 8 mm^2; thickness: 0.8 mm) between the samples and prevent them from touching each others. The distances between the slots were 5 mm for component #1 and 5.5 mm for components #2-3.

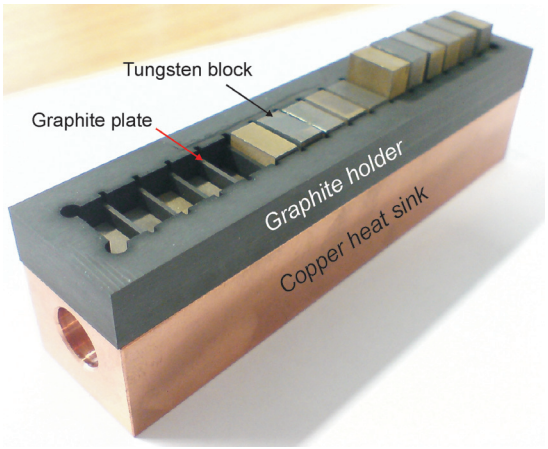

Figure 3.7. Graphite holder positioned on the copper heat sink before the brazing process (component #1). Vertical slots were machined in the inner surfaces of the holder to insert thin graphite plates, which enabled to keep the samples upright and distant from each others during the brazing process.

The brazing cycle consisted of several steps: temperature increased from RT to 350°C (11.7 $K{\cdot}min^{-1}$), then hold at 350°C for 30 min; temperature increased up to 750°C (13.3 $K{\cdot}min^{-1}$), then hold at 750°C for 15 min; temperature increased up to 815°C (3.3 $K{\cdot}min^{-1}$), then hold at 815°C for 10 min. Finally, the temperature was decreased to RT with cooling rates of 13.25 $K{\cdot}min^{-1}$ between 815 and 550°C and 1.5 $K{\cdot}min^{-1}$ between 550°C and RT. Figure 3.8 shows the components after brazing.

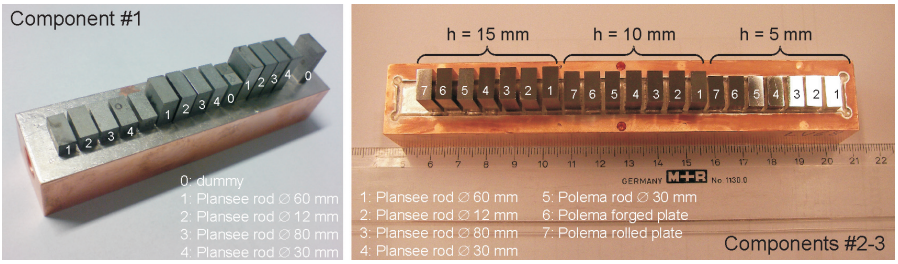

Figure 3.8. Views of (left) component #1 and (right) components #2-3 after brazing.

3.4 Testing under fusion relevant thermal loads

3.4.1 The electron beam facility JUDITH 1

The materials were exposed to thermal loads in the electron beam facility JUDITH 1 (Juelich Divertor Test Facility in Hot Cells), located in Forschungszentrum Jülich, Germany. JUDITH has a maximum power of 60 kW and generates electrons with energies of 120 kV. It can experimentally simulate transient thermal loads such as plasma disruptions, edge localized modes and vertical displacement events in terms of power density and pulse duration. Actively cooled components can also be implemented when simulating steady-state thermal loads (figure 3.9).

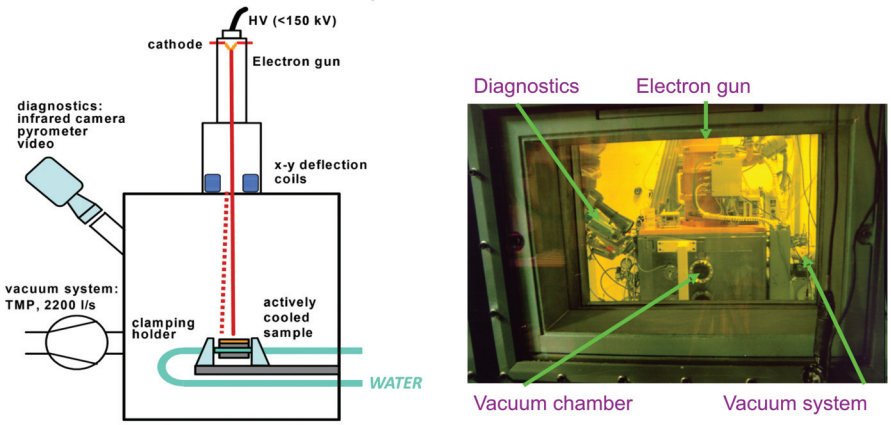

Figure 3.9. (Left) Schematic view of the electron beam facility JUDITH 1 used to simulate fusion relevant thermal loads. (Right) view of the hot cell in which JUDITH 1 is installed.

The electron beam is generated inside the electron gun using a W filament. The electron generation is based on the emission of free electrons, their acceleration in an

electrostatic field and beam focusing via magnetic and electric fields. The electron beam from a cathode type beam generator operates at relatively high acceleration voltages. The beam is characterised by a small beam diameter with a full-width half-maximum (FWHM) of about 1 mm and is swept across the sample surface using a triangular signal. The beam scanning is realised in the x-y plane typically at frequencies of 40 kHz (x-direction) and 31 kHz (y-direction). It enables a relatively homogeneous heating of the sample surface. The beam is impinging perpendicular to the sample surface. The pulse duration can be selected in a range from 1 ms (for transient thermal loading tests) to continuous (for steady-state thermal loading tests). The generation and unrestricted propagation of the beam is only possible in high vacuum. Therefore, it is necessary to evacuate the beam generator, the guidance systems and the working chamber. The vacuum required in the beam-generating chamber is usually in the order of 10^{-2} to 10^{-4} Pa. Cooling of actively cooled components is performed with water at room temperature at a (maximum) flow rate of 60 l·min^{-1}. The flow rates were monitored with two turbine flow meters.

JUDITH 1 is equipped with various diagnostics, which allow the measurement of the absorbed current through the specimen and of the surface temperature during transient and steady-state thermal loads (fast single color pyrometer, two-color pyrometer, infrared camera). A digital camera is available as well to capture pictures during an experiment.

Due to the small diameter of the e-beam in JUDITH 1 (1 mm diameter), especially compared to the large loaded areas of our components (up to 445 mm^2), the beam was scanned with very high frequencies in order to generate heat load distributions as homogeneous as possible. The beam was swept over the samples' surfaces with a triangular signal. Figure 3.10(a) shows the beam scanning pattern after 1 ms with beam frequencies of f_x=40 kHz and f_y=31 kHz on an area of 445 mm^2. The figure 3.10(b) shows the resulting local power absorbed at the center of the scanned area as a function of time for an acceleration voltage of 120 kV and a current of 100 mA. It can be seen that the heat load distribution is not exactly homogeneous as it consists of a sequential deposition of high power peaks up to 6 GW·m^{-2}, higher than those of transient events in fusion devices. However, in the frame of this study, we considered that the terms "steady-state" or "thermal fatigue" referred to loads with power densities of the order of tens of MW·m^{-2} and long pulse durations (several tens of s) and the terms "transient" or "thermal shock" to loads with power densities of several hundreds of MW·m^{-2} and short pulse durations (a few ms) (figure 3.11).

The absorbed power densities P_{abs} [W·m^{-2}] were calculated according to equation 3.1.

$$P_{abs} = \frac{U \cdot I \cdot \epsilon}{S} \tag{3.1}$$

where I is the current [A], U the acceleration voltage [V], ϵ the absorption coefficient for electrons, assumed to be 0.55 for W [131], and S the loaded surface's area [m^2].

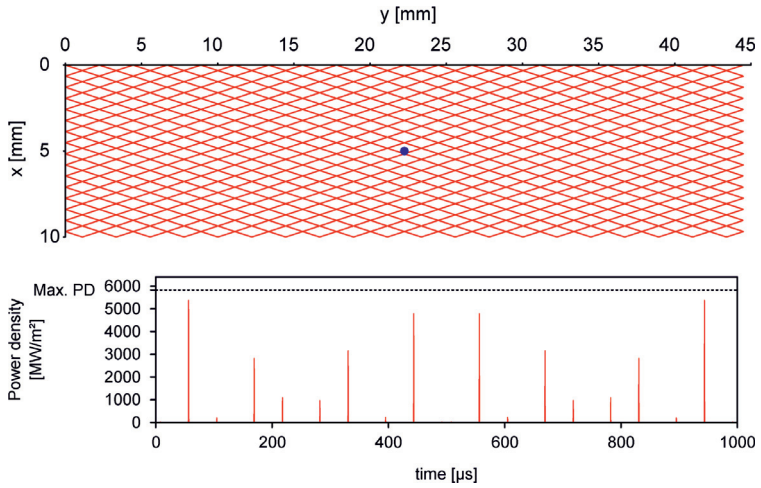

Figure 3.10. (a) Scanning pattern of the beam of JUDITH 1 after 1 ms with scanning frequencies of 40 kHz (x-direction) and 31 kHz (y-direction); (b) resulting local power densities absorbed at the center of the scanned area (position of the blue point on (a)) as a function of time (with U = 120 kV and I = 100 mA). After 1 ms the full area (445 mm^2 in the present simulation) is scanned but the scanning is just fairly homogeneous as it consists of sequential depositions of power peaks.

Assuming that the beam has a Gaussian profile the local power density P_{local} [$W{\cdot}m^{-2}$] absorbed by the area just below the beam can be calculated using the formula 3.2.

$$P_{local} = \frac{U \cdot I}{2\pi \cdot \sigma^2} \tag{3.2}$$

where σ is:

$$\sigma = \frac{\mathrm{FWHM}}{2\sqrt{2\log(2)}} \tag{3.3}$$

and FWHM is the full-width half-maximum of the Gaussian shaped electron beam.

Figure 3.11. Scheme illustrating the loading types: "thermal fatigue" (or "steady-state") refer to loads with power densities of the order of tens of $MW{\cdot}m^{-2}$ and pulse duration of several s (e.g. 15 $MW{\cdot}m^{-2}$ for 20 s) and "transient" (or "thermal shock") to loads with power densities of several hundreds of $MW{\cdot}m^{-2}$ and pulse durations of a few ms (e.g. 500 $MW{\cdot}m^{-2}$ for 5 ms).

The time t during which the power locally loads this area is calculated using the beam velocity. As mentioned previously the beam velocity is governed by two frequencies (f_x, f_y). As the distances d_x and d_y of the scanned (or loaded) area and the frequencies are known the beam velocities (v_x, v_y) can be calculated according to equation 3.4. The mean beam velocity is calculated using a vector sum of the x and y components and the time the beam needs to go back and forth and therefore return to its starting position can be determined.

$$v = \frac{d}{1/f} \tag{3.4}$$

The product of $\sqrt{t}$ and the local power density P_{local} is called the heat flux factor (HFF) (equation 3.5). This useful factor is used within the fusion community as an indicator of damage thresholds of PFMs.

$$\mathrm{HFF} = P_{local} \cdot \sqrt{t} \tag{3.5}$$

Table 3.3 shows the calculated HFF per component for U = 120 kV, f_x=40 kHz and f_y=31 kHz, FWHM = 1 mm. The detailed testing parameters are given in subsections 3.4.2 and 3.4.3.

	Steady-state loads		Transient loads
	Comp. #1	Comp. #2-3	Comp. #2-3
Scanned area dim. d_x/d_y (mm)	10/23	10/44.5	5/5
Mean beam velocities v (m/s)	1635	2873	506
Dwell time t (μs)	0.61	0.35	2.0
Current I (mA)	(1) 65, (2) 55, (3) 40	100	133
Abs. power density P_{abs} (MW/m^2)	(1) 19, (2) 16, (3) 11	15	500
Local power density P_{local} (GW/m^2)	(1) 3.8, (2) 3.2, (3) 2.3	5.8	7.7
Heat flux factor (MW$\sqrt{\mathrm{s}}$/m^2)	(1) 3.0, (2) 2.5, (3) 1.8	3.4	10.8

(1) 5 mm thick blocks (1200°C), (2) 10 mm thick blocks (1600°C), (3) 15 mm thick blocks (2000°C)

Table 3.3. Calculated heat flux factors for the components.

The temperature rise ΔT during transient events is given by the following equation:

$$\Delta T = 2P_{abs}\sqrt{\frac{\Delta t}{\pi \rho c_p \lambda}} \tag{3.6}$$

where Δt is the pulse duration [s], λ the thermal conductivity [W·m^{-1}·K^{-1}], c_p the specific heat [J·kg^{-1}·K^{-1}] and ρ the density [kg·m^{-3}] of the material [132]. This represents a solution for the unidirectional heat conduction equation and gives a rough approximation without taking radiation cooling or evaporation into account.

3.4.2 Thermal loading of cracked surfaces

The cracked specimens were subjected to cyclic steady-state thermal loads only. As in the FE calculations, the three sets of specimens (5, 10 and 15 mm high) were loaded independently. The power density was adjusted on each set to achieve the desired surface temperatures (1200°C, 1600°C, 2000°C); power densities of 19, 16 and 11 MW·m^{-2} were applied on the 5, 10 and 15 mm high blocks respectively. The resulting surface temperatures, measured by two-color pyrometer, were in the ranges of 1185-1208°C (5 mm), 1590-1605°C (10 mm) and 1992-2013°C (15 mm). The cycling was simulated by switching the beam on and off. The cycle duration was 20 s (15 s beam on, 5 beam off) and the cycle number was 1000.

The cycle number was valued over the cycle duration, therefore the time the beam was on (heating time) was reduced just enough to reach a thermal equilibrium (even at the highest temperatures) and the time the beam was off was chosen to cool the samples down to RT between each cycle. Due to cycling between RT and above 1000°C the DBTT of W was crossed periodically.

3.4.3 Thermal loading of defect-free (polished) surfaces

The polished specimens were subjected to cyclic steady-state thermal loads as well as a single transient event, the latter being performed beforehand. The purpose of the combined load was to introduce cracks in the materials and study the further development of the damage under thermal fatigue loads in terms of (i) surface temperatures and (ii) initial surface damage introduced by the thermal shock load. The strategy was to apply the transient load on half of each block (5 by 5 mm^2) and the cyclic steady-state loads on the full surface (5 by 10 mm^2) in order to compare both surfaces' halves (figure 3.12). There were numerous investigations at FZJ that dealt with the response of materials under thermal shock loads [95, 128, 133–143]. Based on these former investigations the testing parameters for the transient load, an absorbed power density of 0.5 GW·m^{-2} with a pulse duration of 5 ms applied at RT, were chosen to induce cracks in the W surfaces. The temperature rise calculated using the equation 3.6 was about 1973,3 K (with P_{abs}=500.10^6 W·m^{-2}, Δt=5.10^{-3} s, λ=161.53 W·m^{-1}·K^{-1}, c_p=131.45 J·kg^{-1}·K^{-1}, ρ=19250 kg·m^{-3}), well below the melting threshold of W.

For the testing under cyclic steady-state thermal loads the approach differed than that employed for component #1 as the power density was fixed at 15 MW·m^{-2} to avoid set-up variations, in particular the variation of the e-beam scanning scheme. The cycle duration was 20 s (15 s beam on, 5 beam off) and the cycle numbers were 50 and 1000 cycles to investigate the damage resistance (damage threshold, damage development rate) of the W materials.

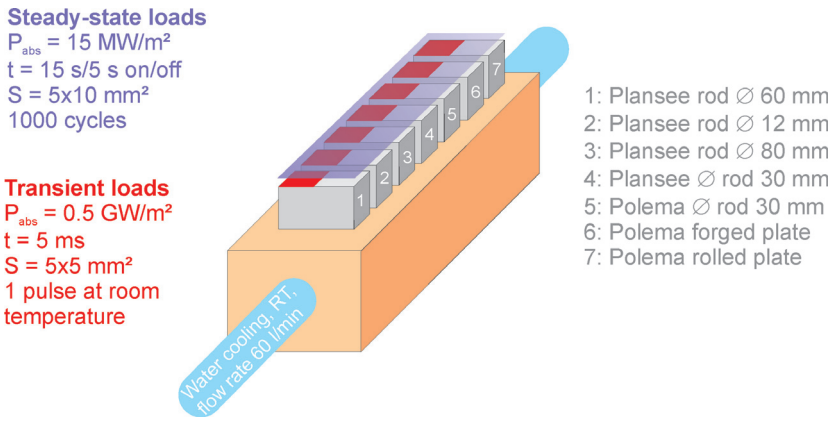

Figure 3.12. Schematic view of the loading scheme applied to components #2 and #3. Half of each surface was subjected to one thermal shock load whereas the full surface was subjected to the thermal fatigue loads.

Two components were necessary to test the materials at two cycle numbers. For component #2 (1000 cycles) the experimental surface temperatures were about 1000°C, 2000°C and 2200°C on the 5, 10, and 15 mm high blocks respectively and for component #3 (50 cycles) about 1900°C and 2600 °C on the 10 and 15 mm high blocks respectively (the 5 mm thick blocks were not tested). The surface temperature on the highest blocks (15 mm) was particularly high because the pyrometer was positioned on a overheating block (the second one starting from the bottom, the 12 mm diameter rod as shown in figure 3.13). The infrared camera indicated that the temperature of the other blocks was 200°C to 300°C lower. Thus, the temperature range was about 2300 to 2600°C on the 15 mm thick specimens.

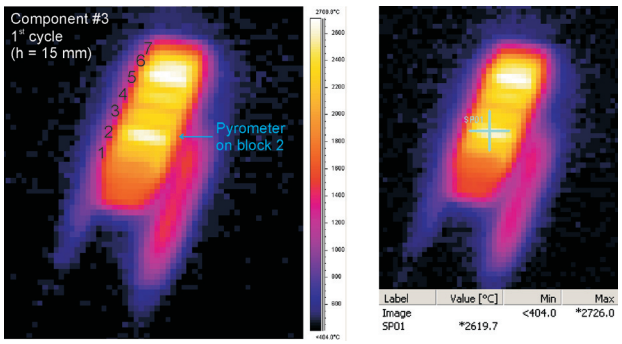

Figure 3.13. Infrared image of component #3 during the steady-state thermal loading of the 15 mm blocks (first cycle). The pyrometer indicated a abnormal surface temperature of about 2600°C because it was set on an overheating block (the second block from the bottom).

3.5 Results

To analyse the surfaces after thermal loads, metallography and material characterisation were performed, in particular the crack pattern was characterised using parameters such as the crack distance, crack width and crack depth (figure 3.14).

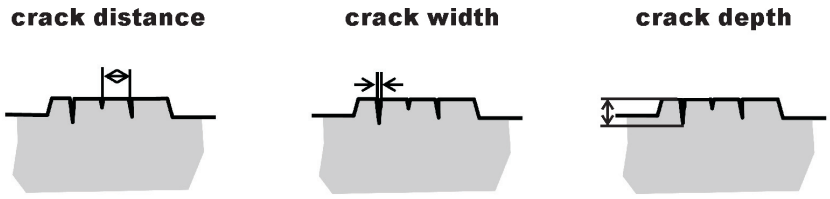

Figure 3.14. Parameters used to characterise the crack pattern.

To measure the crack distance, five equally distanced measurement lines were drawn on pictures of the samples' top surface. Crack distances were measured along each line and then averaged (figure 3.15(a)). The average crack width was determined using the same method (figure 3.15(b)). The crack depth was measured on pictures of the samples' cross section and the measured values were then averaged (figure 3.15(c)).

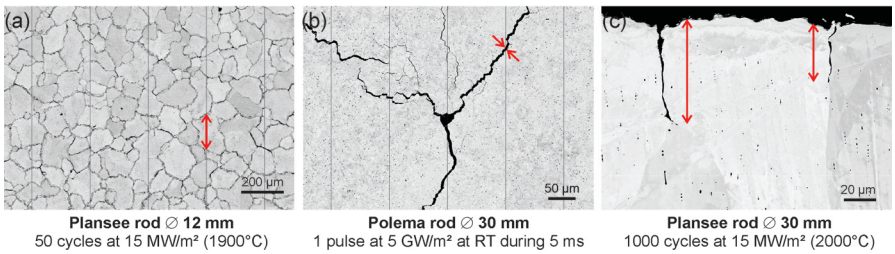

Figure 3.15. Once the top surface of the sample was captured, equally distanced lines were drawn on the picture to measure along the lines (a) crack distances and (b) crack widths. (c) Crack depths were measured on pictures of the cross section and the measured values were then averaged.

3.5.1 Surfaces pre-cracked by electric discharge machining

Before thermal loads (as-machined)

Figure 3.16 shows the materials' surfaces (top surfaces) after EDM. As observed in the He-cooled PFCs for DEMO (chapter 2), discrete cracks occurred in W surfaces. The mechanisms leading to crack formation by EDM were described in [127]. The crack pattern was characterised by a network of curved cracks on the one hand (indicated on the figure by red dotted lines) and discontinuous straight cracks within the areas

marked by the continuous curved cracks on the other hand (indicated by purple arrows). Thus, the crack pattern formed by EDM was characterised by those two distinct types of crack. The crack width was about 5 μm.

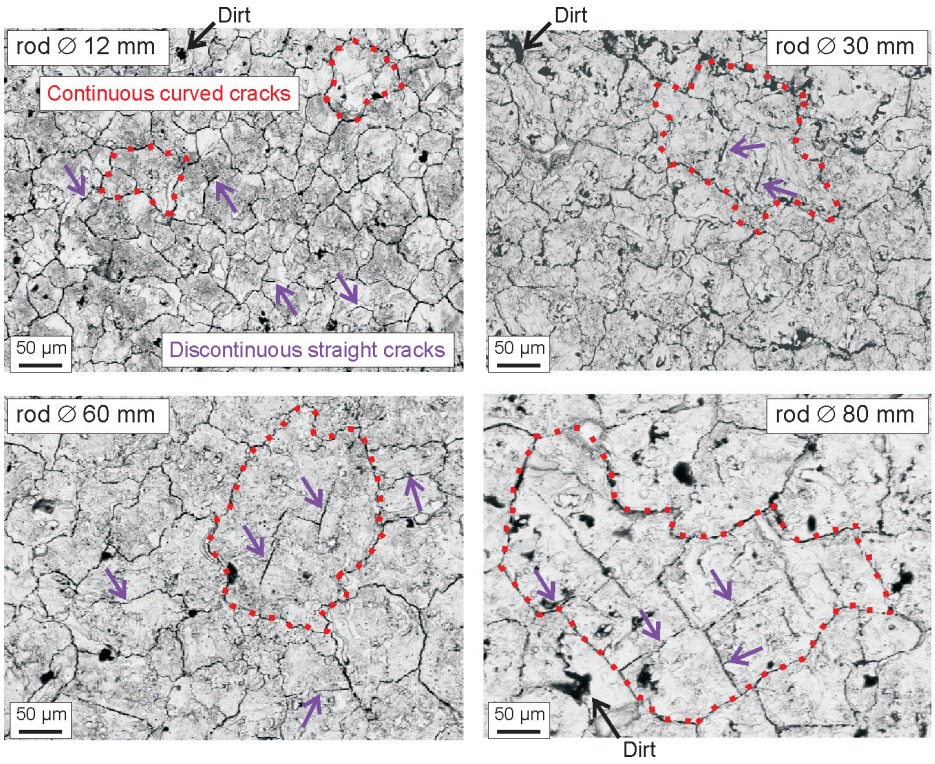

Figure 3.16. BSE micrographs of the as-machined surfaces (top surfaces) showing cracks induced by EDM. The crack pattern was characterised by two different types of crack: continuous curved cracks (red dotted lines) and discontinuous straight cracks (purple arrows). Dirt remained from the wire and the electrolyte employed during the EDM process.

In the 12 mm diameter rod (the smallest rod diameter), the straight cracks were tiny and their crack width was very narrow (less than $\sim$2 μm). In the 80 mm diameter rod (the biggest rod diameter), straight cracks formed clear punctual networks.
Different types of crack were induced by the same machining process, EDM. Obviously, the cause for the formation of different crack types lied in the microstructure of the material. To understand the process of crack formation in W by EDM, the crack distance was measured in two different ways: considering (1) the continuous curved cracks only (as shown in figure 3.17) and (2) both the continuous curved and discontinuous straight cracks (i.e. all cracks). Table 3.4 shows the resulting average crack distances and respective standard deviations. As the discontinuous straight cracks were very tiny

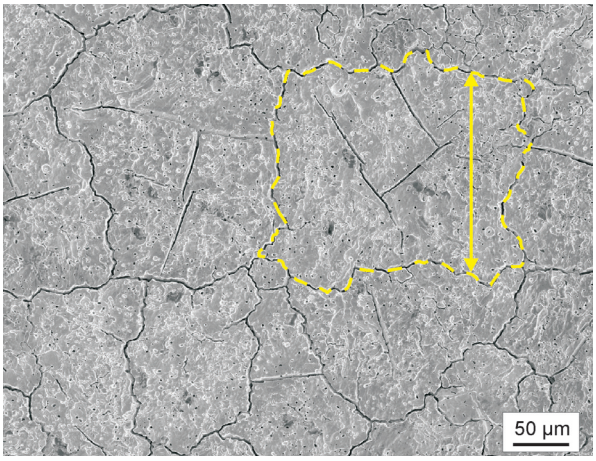

Figure 3.17. SEM micrograph of an as-machined area of the Plansee 60 mm diameter rod showing how the measurement of the crack distance was performed when considering continuous curved cracks only.

and hardly visible in the Plansee 12 mm diameter rod, only the crack distance considering the continuous curved cracks was measured for this material. It was observed

	Average crack distances (in μm)	
Materials	Curved cracks only	Curved and straight cracks
Plansee rod Ø 12 mm	None	30±14
Plansee rod Ø 30 mm	(1)66±34/(2)106±53	(1)66±38/(2)63±36
Plansee rod Ø 60 mm	127±58	59±33
Plansee rod Ø 80 mm	220±141	80±47

Average crack distance on (1) the small grain area and (2)the large grain area of the material

Table 3.4. Average crack distances of the as-machined surfaces considering on the one hand curved continuous cracks only and on the other hand all cracks. Considering curved cracks only, the crack distance increased with the rod diameter, whereas the overall crack distance increased first, and then stabilized.

that the larger the rod diameter, the larger the crack distance of the curved cracks only, whereas the overall crack distance (including all cracks) increased with the rod diameter up to 30 mm and then became relatively (i.e. taking standard deviations into account) stable. It was shown in section 3.2 that within the Plansee rods the grain size also increased with the rod diameter (see table 3.1). Thus, the selective crack distance measurements indicated that the curved cracks might occurred along grain boundaries (inter-granular cracks) whereas the straight cracks might occurred inside the grains (intra-granular cracks). Cracks that occurred at grain boundaries, where the strength

of the material was low, propagated around the grains, forming a network, whereas cracks that occurred inside the grains were discontinuous.
Cracks induced by EDM, independently of their type, showed a shallow crack depth as shown in table 3.5. The cracks were mainly perpendicular to the machined surface as shown in figure 3.18. A few particles were eroded due to crack propagation around the grains.

Materials	Average crack depths (in μm)
Plansee rod Ø 12 mm	32±6
Plansee rod Ø 30 mm	28±9
Plansee rod Ø 60 mm	33±13
Plansee rod Ø 80 mm	28±20

Table 3.5. Average crack depth of the as-machined surfaces (the values of standard deviation are also indicated). The cracks induced by EDM were shallow.

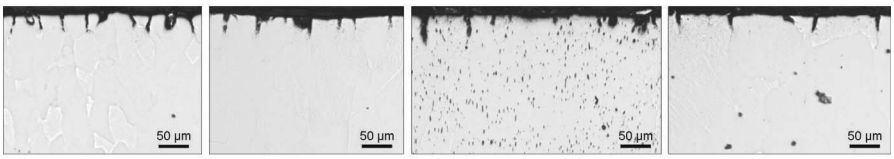

Figure 3.18. Optical micrographs of the cross sections of the as-machined surfaces showing the orientation of the cracks, mainly perpendicular to the machined surfaces.

After thermal loads

The component #1 was tested up to 1000 cyclic thermal loads. However, it was removed from JUDITH 1 after 50, 100, 200, 500 and 1000 cycles for metallographic examinations of the loaded surface to study the development of the surface modifications induced by thermo-mechanical stresses. After 50 cycles at 1200°C the loaded surfaces and the as-machined surfaces showed the same crack patterns, indicating that the thermal stresses induced by the electron beam loading had no impact on the crack pattern formed after machining. Thus, after thermal loads the crack pattern was still characterised by two crack types (continuous curved cracks and discontinuous straight cracks) as shown in figure 3.19.

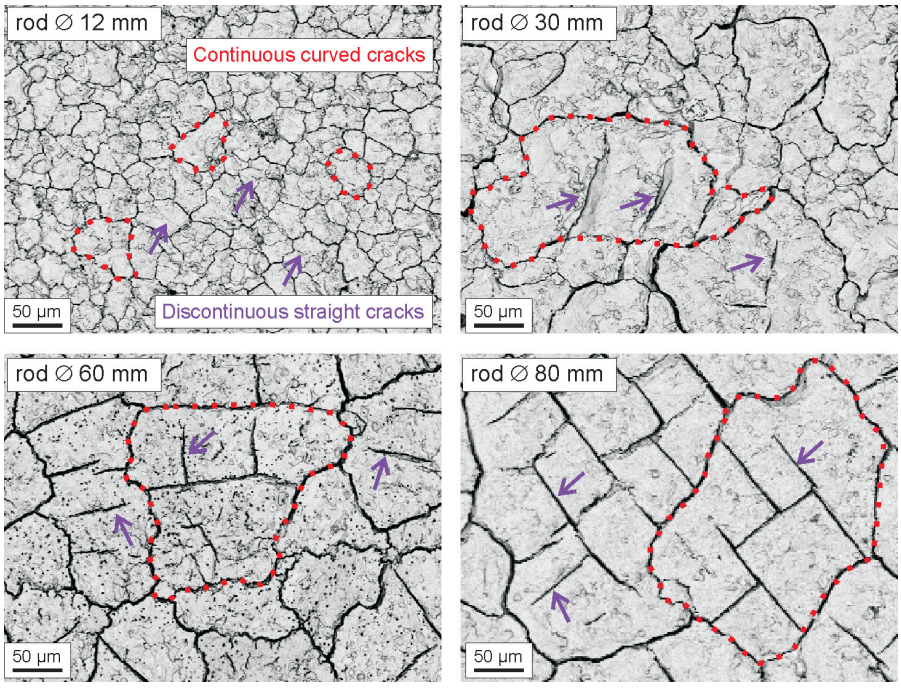

Figure 3.19. BSE micrographs of the pre-cracked surfaces after 50 cyclic thermal loads at 1200°C. The crack pattern was the same to that observed just before thermal loading (i.e. after EDM); characterised by continuous curved cracks (red dotted lines) and discontinuous straight cracks (purple arrows). The stresses induced by thermal fatigue had no impact on the way cracks formed.

Figures 3.20, 3.21, 3.23 and 3.25 show the loaded surfaces of the materials (12, 30, 60 and 80 mm diameter rods respectively) after 200, 100 and 1000 cycles at all surface temperatures (1200, 1600, 2000°C). As observed after 50 cycles (figure 3.19), the crack pattern did not change compared to that of the as-machined surfaces (figure 3.17) despite the accumulation of thermal stresses due to the increase of the cycle number and temperature.

However, the 30 and 60 mm diameter rods (figures 3.21 and 3.23) showed crack opening at the highest surface temperature (2000°C). Before thermal loads, the crack width was less than 5 μm in both materials. The crack width increased between 100 cycles and 500 cycles reaching a maximum value of 11 μm in the 30 mm diameter rod (figure 3.22) while it increased linearly with the cycle number and reached a maximum value of 26 μm after 1000 cycles in the 60 mm diameter rod (figure 3.24).

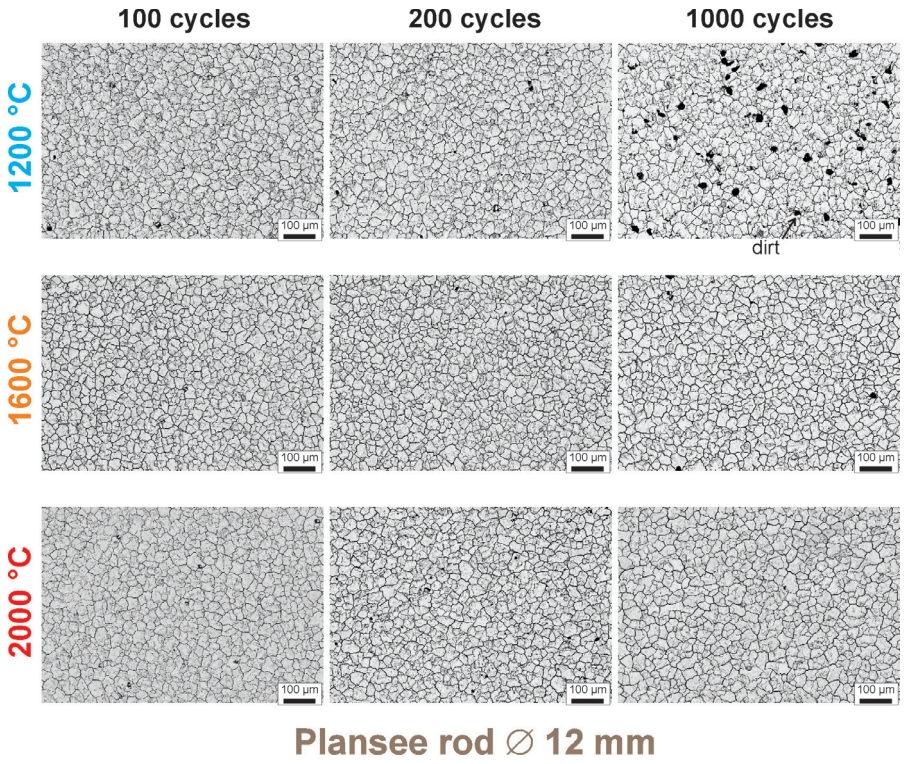

Figure 3.20. BSE micrographs of the loaded areas of the 12 mm diameter rod at various cycle numbers and surface temperatures. The crack pattern showed no variation despite changes in the cycle number and temperature.

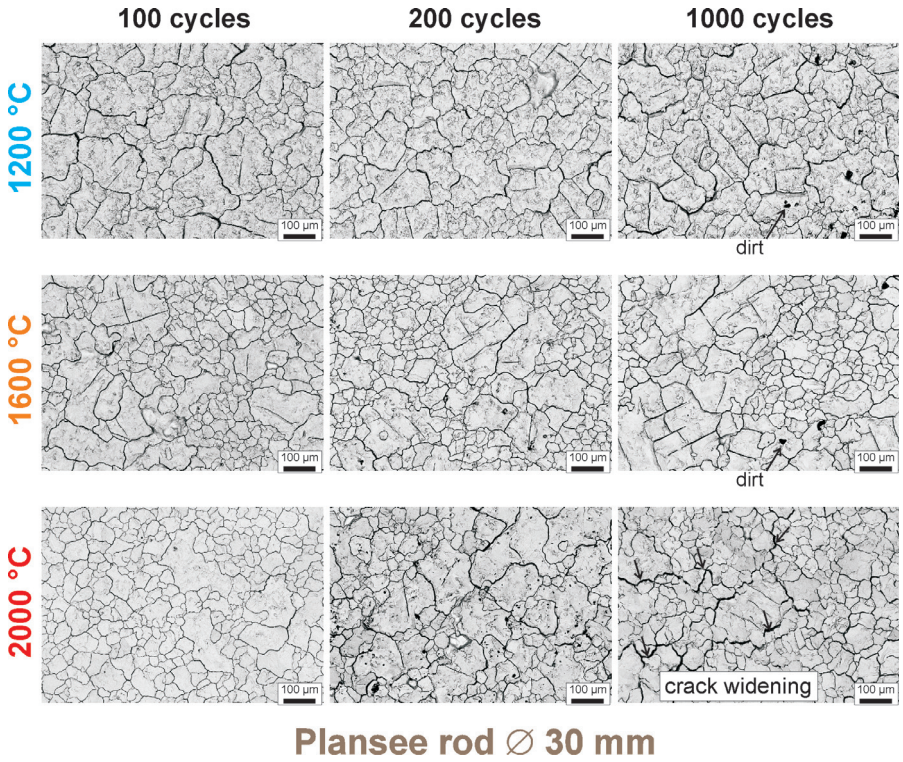

Figure 3.21. BSE micrographs of the loaded surfaces of the 30 mm diameter rod at various cycle numbers and surface temperatures. In general, the crack pattern showed no variation despite changes in the cycle number and temperature. However, crack opening (indicated by the arrows) occurred at 2000°C.

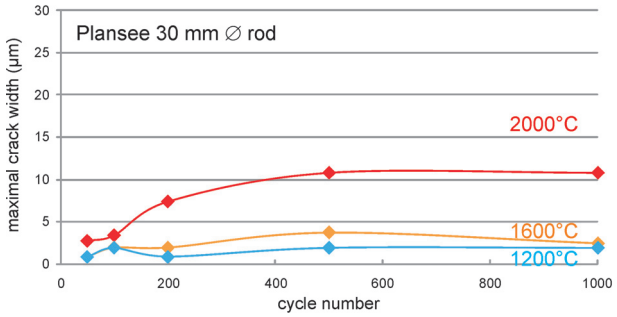

Figure 3.22. Maximal crack width as a function of the cycle number in the 30 mm diameter rod. Crack opening occurred at 2000°C after 100 cycles and the crack width increased up to 11 μm, remaining constant after 500 cycles.

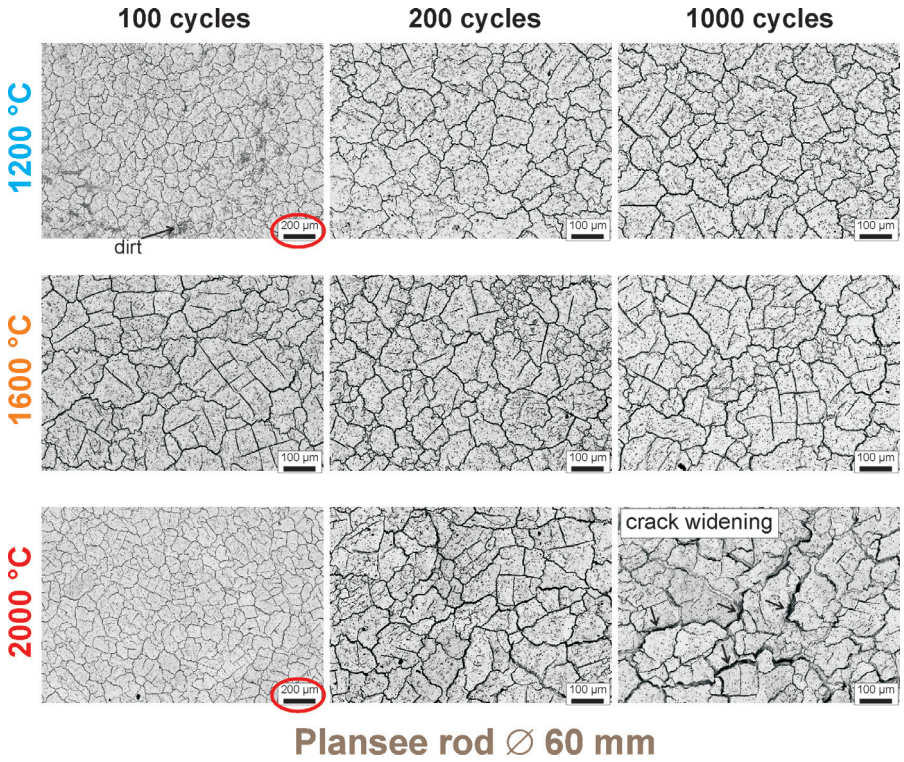

Figure 3.23. BSE micrographs of the loaded areas of the 60 mm diameter rod at various cycle numbers and surface temperatures. In general, the crack pattern showed no variation despite changes in the cycle number and temperature. However, crack opening (indicated by the arrows) occurred at 2000°C.

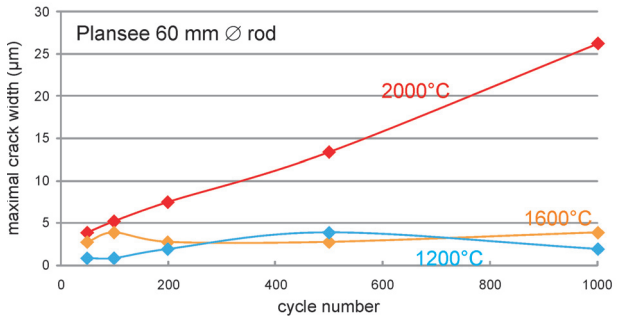

Figure 3.24. Maximal crack width as a function of the cycle number in the 60 mm diameter rod. Crack opening occurred at 2000°C. The crack width increased linearly with the cycle number, reaching up to about 26 μm after 1000 cycles.

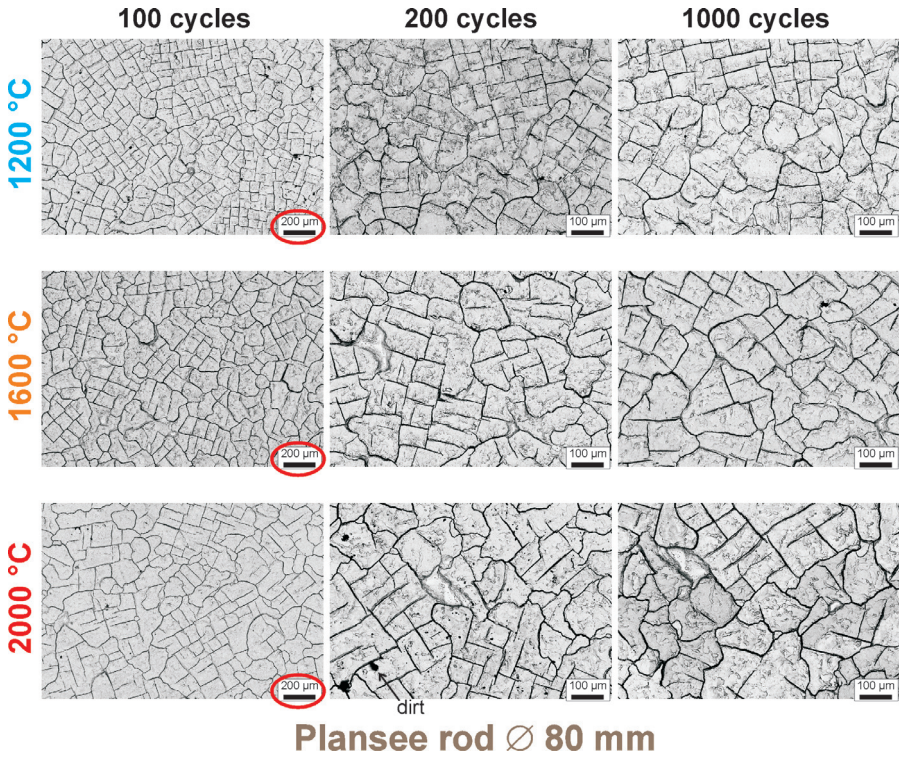

Figure 3.25. BSE micrographs of the loaded surfaces of the 80 mm diameter rod at various cycle numbers and surface temperatures. The crack pattern showed no variation despite changes in the cycle number and temperature.

The crack distance was measured on the loaded surfaces after several cycles numbers (50, 100, 200, 500, 1000 cycles) at all surface temperatures. Table 3.6 shows the resulting average crack distances with standard deviations. In general, like the crack pattern, the crack distance showed no variation despite changes in the cycle number and temperature. Actually, the crack distance was in the same range as that measured in the as-machined samples (table 3.4), indicating that after crack formation by machining no additional cracks formed under thermal fatigue loads (i.e. the crack density was constant).
The crack distance varied more significantly in the 30 mm diameter rod than in other materials but as this material was originally (i.e. before thermal loading) characterised by two specific grain sizes, this variation was probably directly related to the microstructure of the material rather than an impact of the thermal loading.

After 1000 cycles component #1 was cut perpendicular to the loaded surface for cross section analysis (figure 3.26). The cracks were mainly perpendicular to the loaded surface (like in the as-machined surfaces).

	Average crack distances (in μm)											
	Plansee rod Ø12 mm			Plansee rod Ø30 mm			Plansee rod Ø60 mm			Plansee rod Ø80 mm		
Cycle number	1200°C	1600°C	2000°C	1200°C	1600°C	2000°C	1200°C	1600°C	2000°C	1200°C	1600°C	2000°C
50 cycles	31±15	24±13	20±8	52±32	60±44	28±17	67±42	53±28	63±45	63±29	70±41	87±37
100 cycles	29±13	21±11	26±11	71±44	40±32	33±22	91±46	61±25	66±36	68±35	90±46	80±36
200 cycles	25±12	24±11	20±11	56±31	40±29	47±33	55±34	52±36	45±26	56±27	60±28	66±41
500 cycles	31±13	22±10	26±14	92±44	62±43	32±23	49±33	59±28	65±38	57±30	72±47	76±40
1000 cycles	28±14	22±12	25±11	54±31	38±30	38±28	60±31	62±32	52±24	75±44	68±28	67±34

Table 3.6. Average crack distances of the loaded surfaces. The crack distance did not vary despite changes in the cycle number and temperature, indicating that once cracks were formed by EDM no additional cracks were induced by thermal fatigue induced stress.

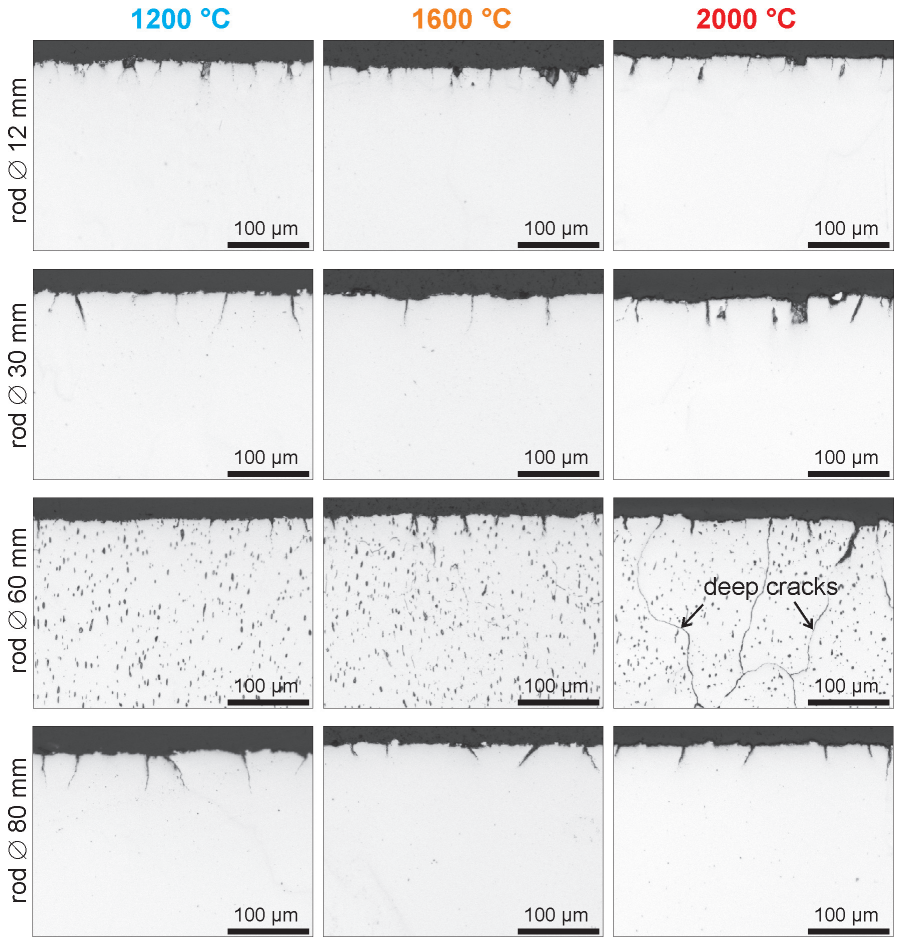

Figure 3.26. Optical micrographs of the cross sections of the pre-cracked surfaces after exposure to 1000 cyclic thermal loads showing that cracks were mainly perpendicular to the loaded surface.

The 60 mm diameter rod was severely degraded at 2000°C. On top of crack opening (figure 3.24), cracks, which occurred at the grain boundaries, propagated around the relatively large grains of the material and then enlarged at random places inside of the bulk resulting in cavities formation (figure 3.27). The crack depth reached hundreds of mm.

In the other materials, the crack depth was shallow (∼20-30 μm). The table 3.7 summarizes the crack depth values measured in as-machined and loaded surfaces. It can be seen as the crack depth was the same before and after thermal loading, the accumulation of thermal stresses by cycling and the increase of the temperature did not induce enough stresses for cracks to proceed.

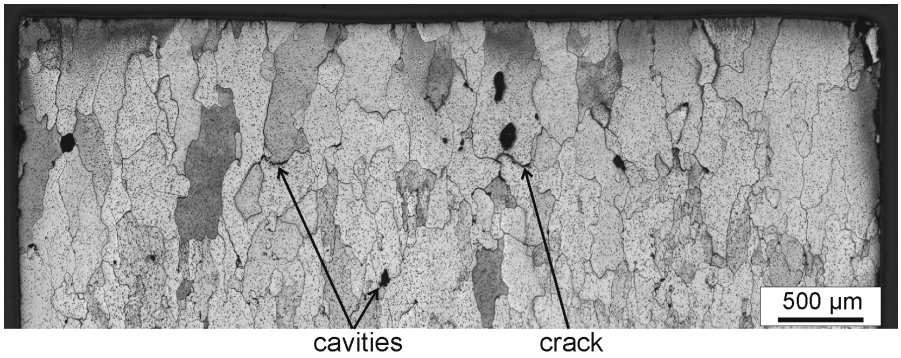

Figure 3.27. Optical micrograph of the cross section of the 60 mm diameter rod after 1000 cycles at 2000°C showing a heavy degradation of this material.

	Average crack depths (in μm)			
Materials	As-machined	1200°C	1600°C	2000°C
Plansee rod Ø 12 mm	32±6	25±4	17±4	19±1
Plansee rod Ø 30 mm	28±9	28±7	40±1	24±13
Plansee rod Ø 60 mm	33±13	27±4	19±8	heavily damaged
Plansee rod Ø 80 mm	28±20	36±9	35±4	22±8

Table 3.7. Average crack depths of cracked surfaces before and after exposure to cyclic thermal loads (1000 cycles). The crack depth remained shallow. The crack depths of the materials were similar.

Grain growth was observed at 1600°C in the 12 and 30 mm diameter rods and at 2000°C in the 60 and 80 mm diameter rods (figure 3.28). The cross section views of the samples after etching showed that for all testing conditions both inter- and intra-granular cracks were observed; cracks occurred in the surfaces regularly regardless of the grain boundaries and grain growth, probably because they were induced before thermal loads.

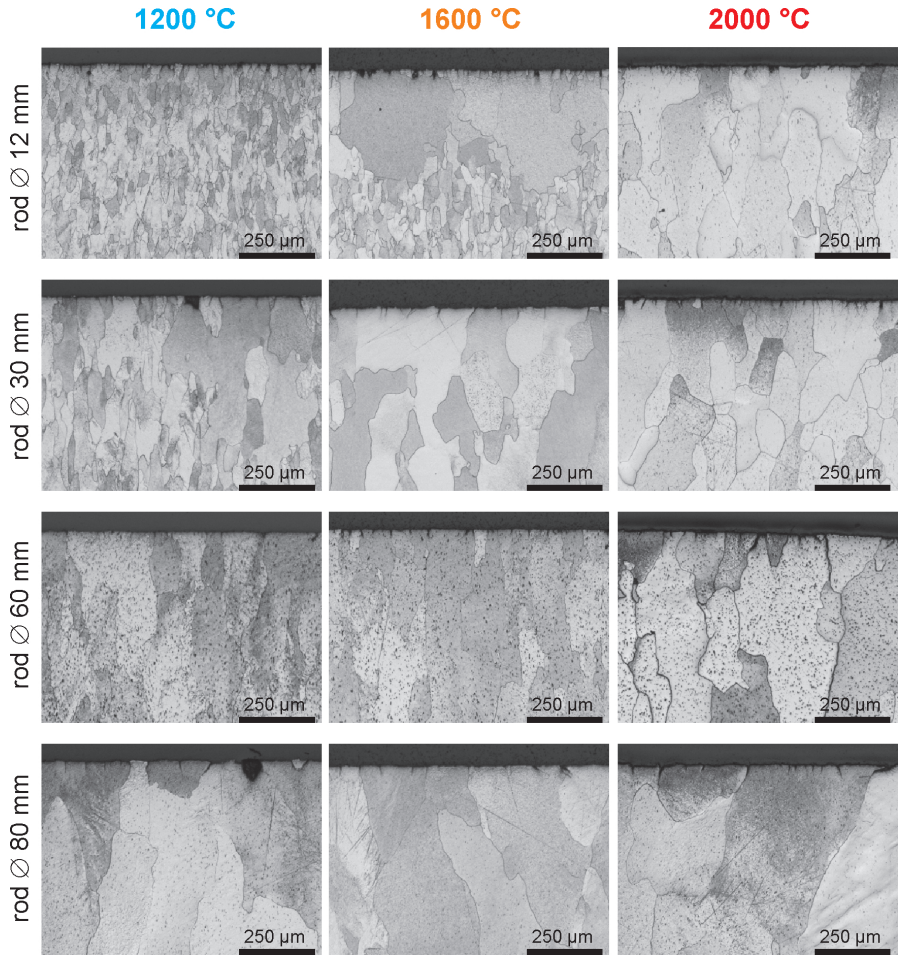

Figure 3.28. Optical micrographs (after etching) of the cross sections of the loaded surfaces. Cracks occurred at regular intervals independently of the grain growth. Thus, both inter- and intra-granular cracks were observed.

Summary

Before thermal loads, cracks were induced in W surfaces by EDM. A characteristic crack pattern was generated with on the one hand continuous curved cracks and on the other hand discontinuous straight cracks. It has been observed that like the grain area, the crack distance of the continuous curved cracks increased with the rod diameter whereas the crack distance of both continuous curved and discontinuous straight cracks slightly increased first and then saturated. It indicated that the continuous curved cracks probably occurred at the grain boundaries (inter-granular cracks) while the discontinuous straight cracks occurred inside the grains (intra-granular cracks).

Cracks that occurred at grain boundaries, where the strength of the material was low, propagated around the grains, forming a network, whereas cracks that occurred inside the grains, where the strength of the material is higher, were stopped in their propagation.

After thermal loads, the accumulation of thermal stresses due to cycling and the increase of the temperature had in general no impact on damage development: the crack pattern (crack formation), the crack distance (crack density) and the crack depth (crack propagation). The thermal stresses induced by the electron beam loading were not high enough for additional cracks to form and for cracks to proceed. This effect was probably related to the stress relaxation provided by the cracks formed by machining (EDM).

The Plansee materials performed relatively similar, except the 60 mm diameter rod which showed a lower resistance by the electron beam induced thermal stresses at high temperature (2000 °C). Crack opening and important crack propagation were observed in this material.

3.5.2 Surfaces prepared by polishing

Before thermal loads (polished)

The cutting of the samples by EDM induced shallow cracks in their surfaces as shown previously. To remove the cracks, the samples surfaces were polished after cutting. A surface finishing such as polishing enabled to remove 100 to 500 μm thick material layers, thus guaranteeing crack-free surfaces (cracks induced by EDM are 30 μm deep) as shown in figure 3.29.

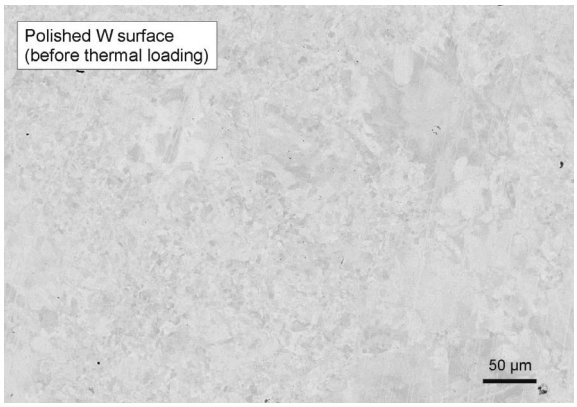

Figure 3.29. BSE image of a tungsten surface (here, the Plansee rod with a diameter of 30 mm) after polishing showing no defects.

After thermal fatigue loads

Note: the Plansee rod with a diameter of 60 mm showed a particular thermal response described separately and further in this report.

The surfaces exposed to 1000 steady-state thermal loads at 1000°C showed no damages (figure 3.30). The thermal stresses induced by thermal fatigue loads did not exceed the strength of W because the surface temperature was too low.

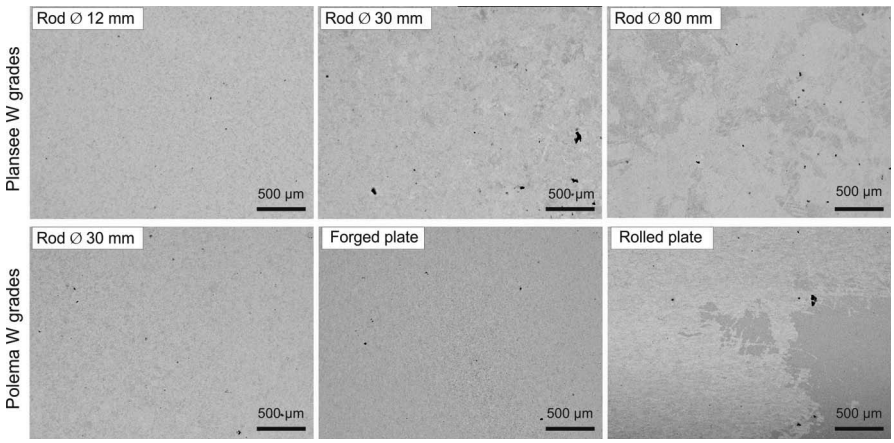

Figure 3.30. BSE images of the loaded surfaces after 1000 cycles at 1000°C showing no damages as the temperature was too low to generate stresses high enough for the material to fail.

After 50 cycles at 1900°C, cracks due to thermal fatigue were observed on the loaded surfaces as shown in figure 3.31(a). The mechanisms leading to crack formation under thermal stresses generated by electron bombardment are described in the introduction (see section 1.7). Beside cracking, surface roughening also occurred on the loaded surfaces except in the rolled plate (figure 3.31(b)). Roughening resulted in a change of the materials reflectivity which became visible by a darkening of the loaded area. On top of cracking and roughening, the Polema forged plate showed particle erosion (grain loss) and surface melting (figure 3.31(c)). Particle erosion was due to crack propagation around the grains, which were then ejected. Some grains were just partially disconnected from the rest of the bulk but it was enough for cracks to act as thermal barriers and lead to surface melting. Melting was indicated by wavelets on the grains and small W fragments that piled up at the cracks edges forming like tiny walls on the cracks contours. All loaded surfaces tested up to 50 cycles at particularly high surface temperatures (∼2300-2600°C) showed cracking and roughening (figure 3.32).

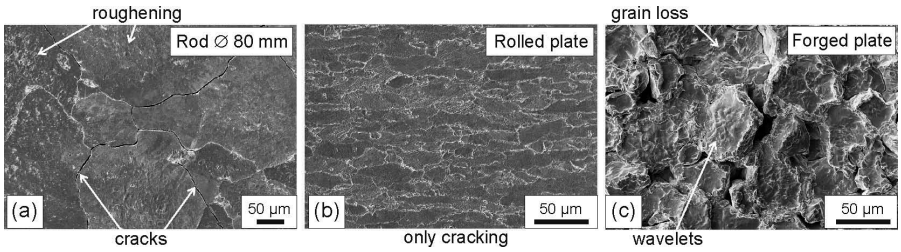

Figure 3.31. SEM micrographs of the loaded areas after 50 cycles at 1900°C showing (a) cracking and roughening (e.g. 80 mm diameter rod) as it happened in almost all materials, (b) cracking only in the rolled plate, and (c) cracking, roughening, particle erosion and surface melting in the forged plate.

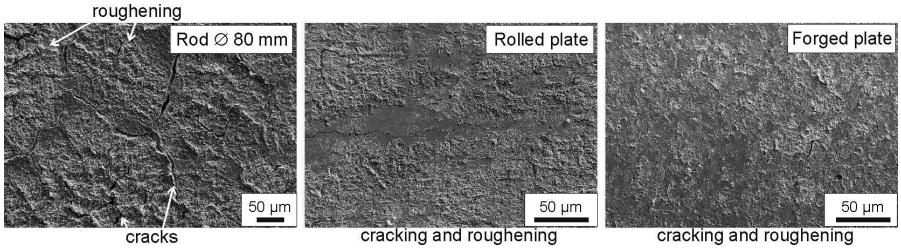

Figure 3.32. SEM micrographs of the loaded areas after 50 cycles at temperatures above 2300°C. Such extreme temperatures induced cracking and roughening in all materials.

After 1000 cycles at 2000°C the loaded surfaces showed a similar degradation tendency as that observed after 50 cycles at almost the same temperature, namely 1900°C: cracking and roughening in all rods (figure 3.33(a)), cracking in the rolled plate (figure 3.33(b)), and cracking, particle erosion as well as melting in the forged plate (figure 3.33(c)). The increase of the cycle number led to crack propagation around the

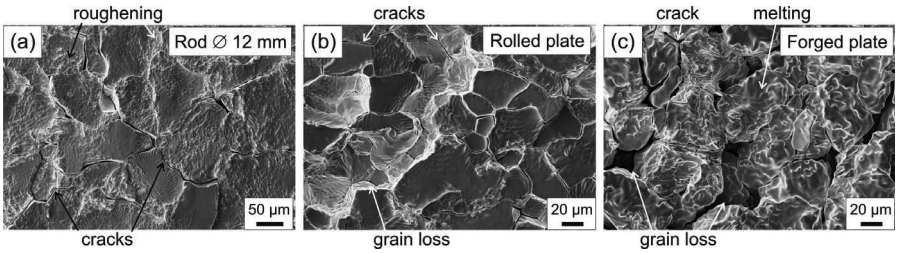

Figure 3.33. SEM micrographs of the loaded areas after 1000 cycles at 2000°C showing (a) cracking and roughening (e.g. 12 mm diameter rod) as it happened in the rod materials, (b) cracking and particle erosion in the rolled plate, and (c) cracking, particle erosion, and melting in the forged plate.

grains, even in the rolled plate (which also showed a crack network). However, even after 1000 cycles, this material showed no roughening, indicating that it has a higher roughening threshold compared to the other materials.

On top of the damages observed at 2000°C (cracking, roughening, and melting), the increase of the temperature up to 2200°C led to material lifting (figure 3.34(a)). After 1000 cycles at 2200°C, the rolled plate also showed surface roughening (figure 3.34(b)). The forged plate showed surface melting again (figure 3.34(c)).

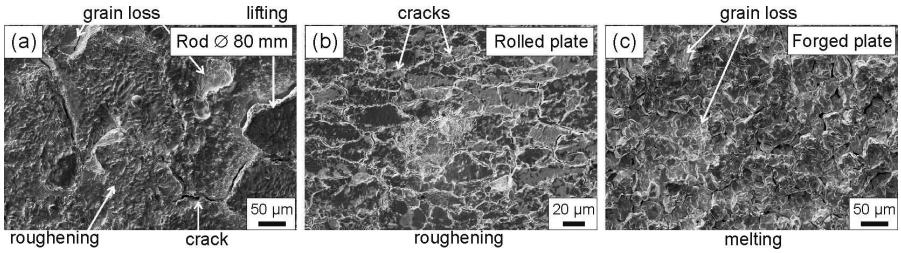

Figure 3.34. SEM micrographs of the loaded areas after 1000 cycles at 2200°C. The increase of the temperature from 2000 to 2200°C led to (a) material lifting on top of roughening and cracking (e.g. Plansee 80 mm diameter rod) in the rod materials, (b) roughening in the rolled plate, and (c) completely molten grains in the forged plate.

In general, the crack patterns after 50 and 1000 cycles were similar: cracks induced by thermal fatigue were curved and formed a network on the whole loaded surface (figure 3.35). Cracks followed the grain orientation on the loaded surface and as a result they tended to describe circles in the rods and the forged plate, which had no preferential grain orientation, while they were parallel to each others in the rolled plate, which showed a strong grain orientation. The rolled plate was the only material showing discontinuous cracks after 50 cycles at 1900°C, indicating a higher resistance to crack propagation.

The average crack distances after 50 cycles at 1900°C and after 1000 cycles (at 2000 and 2200°C) were in the same range (table 3.8). The accumulation of thermal stresses induced by cycling combined to the slight increase of the surface temperature (between 100 and 300°C depending on the samples' thickness) showed no impact on the crack distance (nor the crack pattern). However, smaller crack distances (i.e. higher crack densities as the loaded area was identical for all samples) were measured in the samples tested at temperatures above 2300°C. Thus, the increase of the temperature above 2200°C increased the crack formation. The crack patterns of the surfaces subjected to 50 cycles at very high temperatures (∼2300-2600°C) are shown in figure 3.36. Crack widths up to 15 μm were measured on these surfaces (versus 2.4 μm in the other testing conditions).

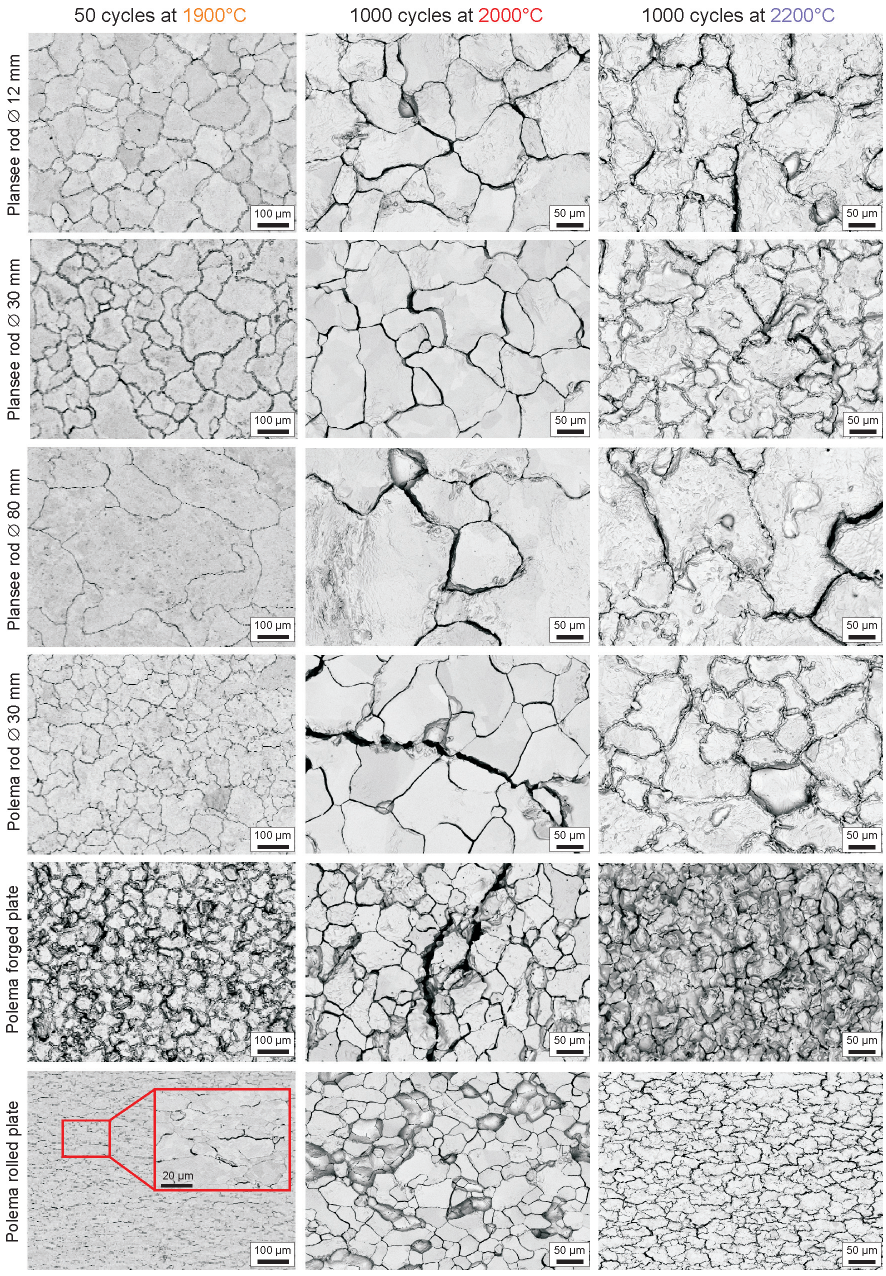

Figure 3.35. BSE micrographs of the loaded areas after 50 cycles (1900°C) and 1000 cycles (2000°C and 2200°C) showing crack network formed by the thermal fatigue induced cracks. Cracks followed the grain orientation on the loaded surface and therefore had no preferential orientation except in the rolled plate (cracks almost parallel to each others). The crack width was about 2.4 μm.

	Average crack distances (in μm)			
	50 cycles		1000 cycles	
Materials	1900°C	≥2300°C	2000°C	2200°C
Plansee rod Ø 12 mm	101±48	63±24	78±42	76±40
Plansee rod Ø 30 mm	92±36	66±25	72±44	79±45
Plansee rod Ø 80 mm	174±101	35±24	246±122	179±37
Polema rod Ø 30 mm	74±40	44±15	73±32	65±29
Polema plate (forged)	42±19	22±12	63±43	38±14
Polema plate (rolled)	21±12	30±14	26±11	16±6

Table 3.8. Average crack distances of the loaded surfaces. The accumulation of thermal stresses induced by cycling and the increase of the surface temperature had no impact on the crack distance (i.e. the crack density), except at extreme temperatures (i.e. ≥2300°C).

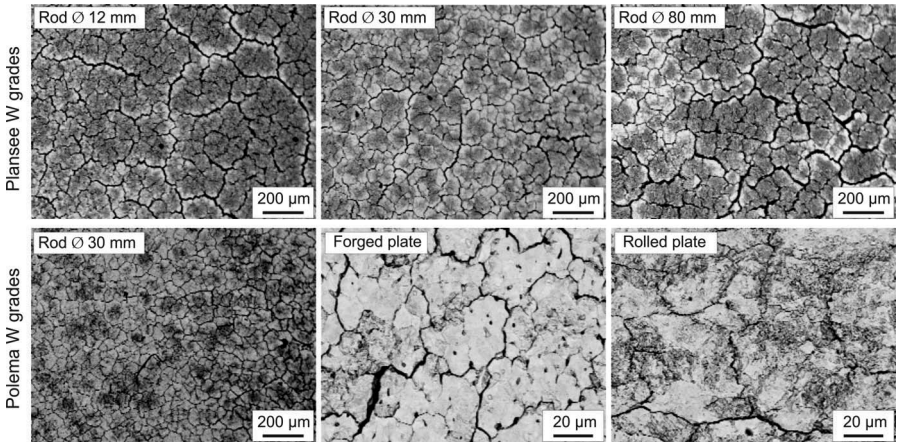

Figure 3.36. BSE micrographs of the loaded areas after 50 cycles above 2300°C. Due to the very high temperatures achieved on those surfaces, the crack density was particularly high and crack opened (crack width up to 15 μm)

.

Two cuts were performed in components #2 and #3 for cross section analysis: one through the side subjected to thermal fatigue loads only and one through the side subjected to the combined thermal load (figure 3.37). The cracks due to thermal fatigue occurred at grain boundaries as shown in the cross section views (figure 3.38). Thus, the increase of cycle number and surface temperature did not induce the formation of intra-granular cracks. However, the accumulation of thermal stresses by cycling had an impact on the crack depth, which increased with the cycle number. The average crack depths after 50 and 1000 cycles are shown in in table 3.9.

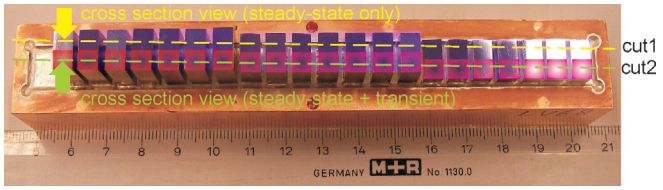

Figure 3.37. Two cuts were performed in components #2 and #3 for cross section examinations, one in the side exposed to thermal fatigue loads only and one in the side subjected to the combined thermal load.

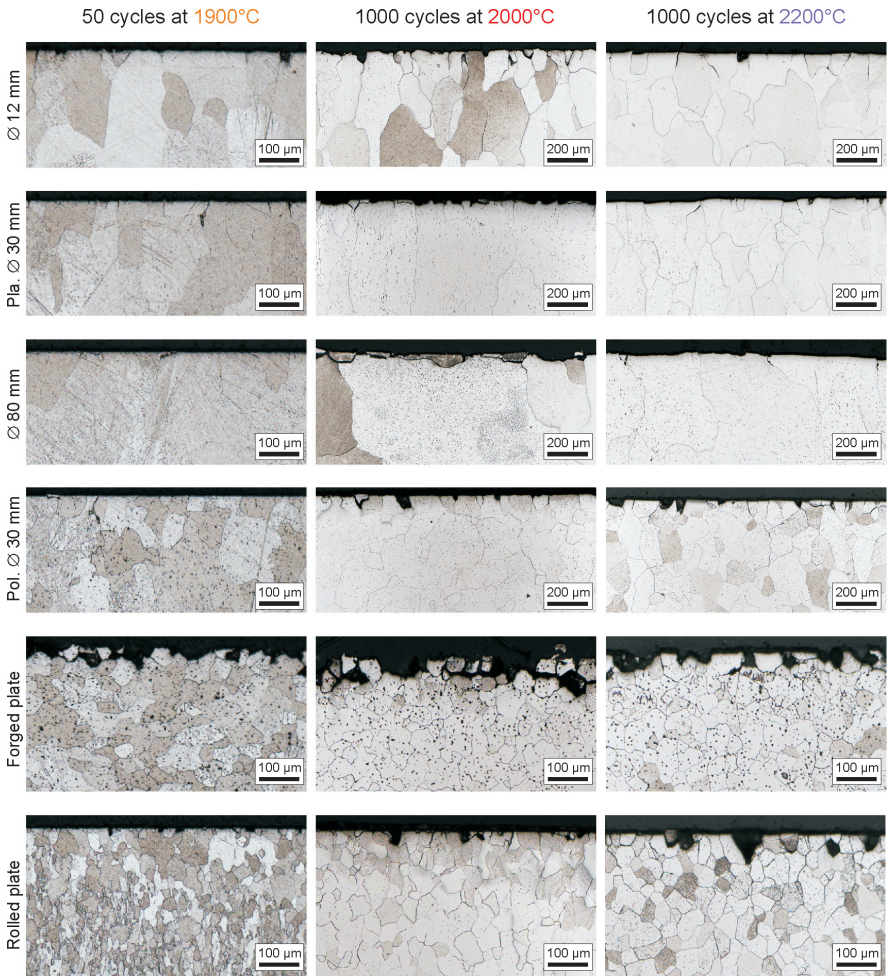

Figure 3.38. Optical micrographs of the cross sections of the loaded areas. The cracks induced by thermal fatigue were inter-granular, under all testing conditions.

At 50 cycles the increase of the temperature (from 1900 to more than 2300°C) showed no impact on the crack depth. The same observation was made at 1000 cycles. Therefore, the accumulation of thermal stresses at the crack tips caused by cycling was probably the main reason for crack propagation. Thermal strain at the crack tips caused cracks to grow further.

	Average crack depths (in μm)			
	50 cycles		1000 cycles	
Materials	1900°C	≥2300°C	2000°C	2200°C
Plansee rod Ø 12 mm	25±10	37±22	98±27	53±21
Plansee rod Ø 30 mm	21±8	26±8	43±18	36±11
Plansee rod Ø 80 mm	15±7	17±6	73±27	47±15
Polema rod Ø 30 mm	8±2	17±7	54±20	49±17
Polema plate (forged)	40±10	21±6	49±14	45±15
Polema plate (rolled)	6±3	5±6	23±12	53±13

Table 3.9. Average crack depths after 50 and 1000 cyclic thermal loads. The crack depth showed a tendency to increase with the cycle number due to the accumulation of stresses at the crack tips (the temperature variation at 50 and 1000 cycles showed no impact on the crack depth).

The 12 mm diameter rod showed a abnormal high crack depth after 1000 cycles at 2000°C because the sample was overheating as shown in figure 3.46 in section 3.5.3 probably due to a defective bond between the block and the heat sink. The rolled plate showed the smallest crack depth in general and consequently the highest resistance to crack propagation. The crack depth of all other materials was in a range of about 45 to 55 μm.

Once inter-granular cracks formed, they showed a tendency to propagate with increasing the cycle number. Cracks propagated along the grain boundaries and consequently followed the direction of the grain deformation. In the rods, the grain size was relatively large compared to the crack propagation range (or depth) therefore, most of the cracks were vertical (figure 3.39). When the crack propagation range was larger than the grain size, cracks propagated horizontally, which led to ejection of particles, hence the particle erosion observed in the plates in which the grain size was small, even after grain growth. The rolled plate, which had a higher resistance to crack propagation, showed a lower erosion than the forged plate.

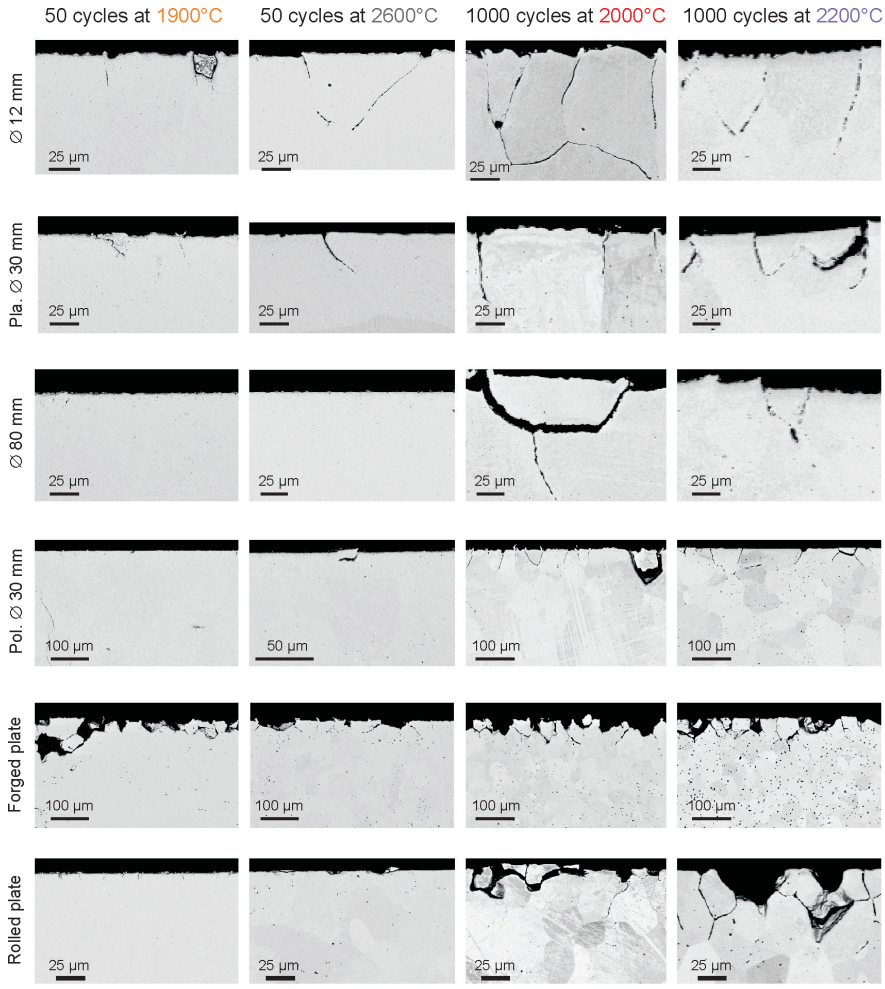

Figure 3.39. BSE micrographs of the cross sections of the loaded surfaces. Intergranular cracks tended to follow the grain orientation during propagation. In the rods, the crack propagation range was smaller than the grain size and therefore, the cracks propagated perpendicular to the loaded surface. In the plates, the grain size was relatively small and as a result, the cracks propagated horizontally, ejecting grains.

Due to the high temperatures achieved during thermal loads the materials starting recrystallisation as shown in figures 3.40 and 3.41 (the pictures were tilted of an angle ±90°C, i.e. the loaded surface is vertical, and as it was necessary to take several pictures to make a panorama of the blocks, different contrasts could appear during the transition from a picture to an other; the arrows indicate the grain growth depth).

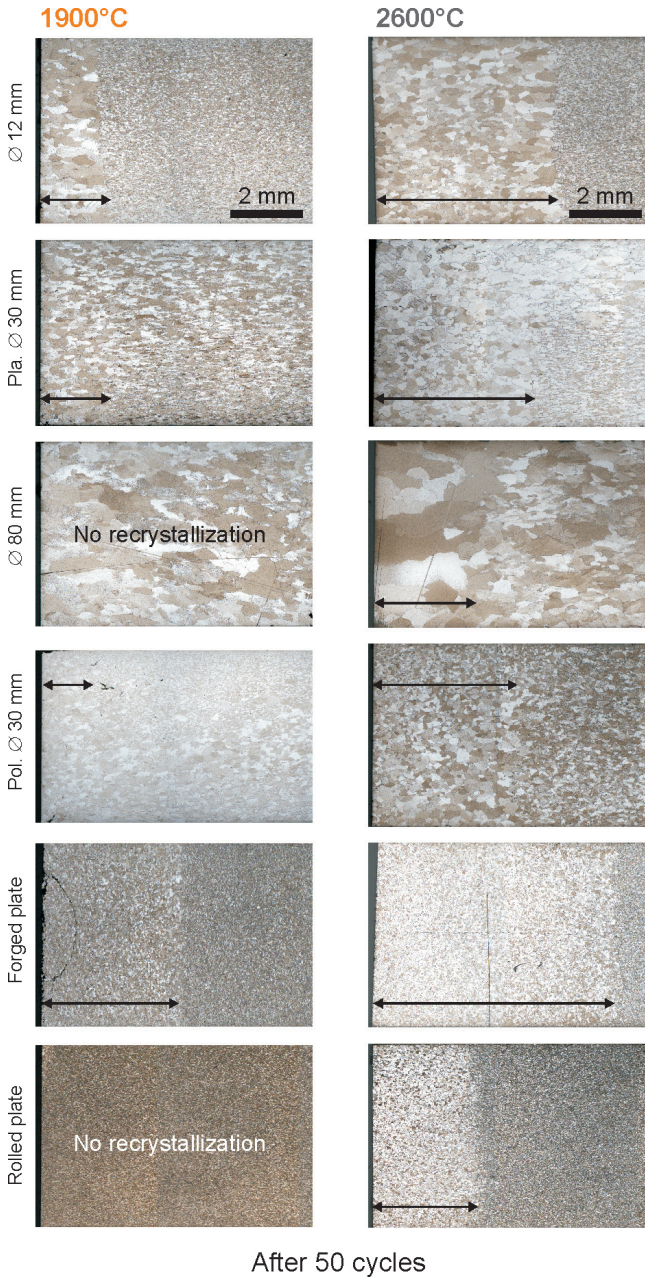

Figure 3.40. Optical micrographs of the cross sections of the loaded blocks after 50 cycles showing grain growth in almost all materials. The arrow indicates the depth up to which grain growth occurred. The forged plate showed the highest grain growth depths. The rolled plate and the 80 mm diameter rod did not recrystallise after 50 cycles at 1900°C.

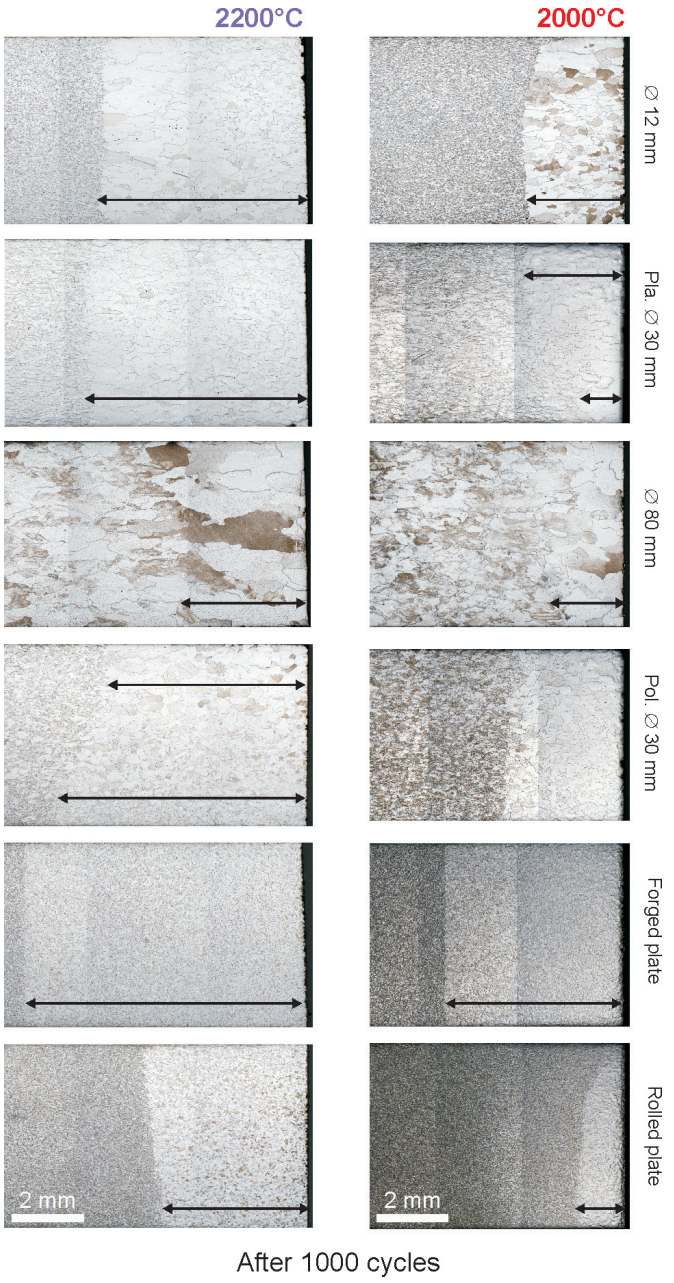

Figure 3.41. Optical micrographs of the cross sections of the loaded blocks after 1000 cycles showing grain growth in all materials. The arrow indicates the depth up to which grain growth occurred. The forged plate showed the largest grain growth ranges whereas the rolled plate and the 80 mm diameter rod showed the smallest ones.

The grain growth depths are shown in table 3.10. After 50 cycles at temperatures above 2300°C the grain growth depths were smaller than those observed after 1000 cycles at lower temperatures (below 2200°C), indicating that the recrystallisation was not complete after 50 cyclic thermal loads despite high temperatures. As a result, the recrystallisation temperature (RCT) could not be directly determined even after 1000 cycles. However, it has been observed that the grain growth per material showed the same tendency under all testing conditions. Thus, the forged plate showed the largest grain growth range, whereas the rolled plate and the 80 mm diameter rod showed the smallest ones. Furthermore, no grain growth was observed in those two materials after 50 cycles at 1900°C. The 12 and 30 mm rods (both Plansee and Polema materials) showed an intermediate grain growth range. As some samples overheated during thermal loads, a clear statement on the recrystallisation effects in those materials could not be made, but based on the tendency observed, the Polema rolled plate and the Plansee 80 mm diameter rod materials had probably the lowest RCT and the forged plate the highest one.

	Grain growth depth (in mm)			
	50 cycles		1000 cycles	
Materials	1900°C	>2300°C	2000°C	2200°C
Plansee rod Ø 12 mm	1.6	4.8	2.5	5.3
Plansee rod Ø 30 mm	1.8	4.4	1.3-2.8	5.8
Plansee rod Ø 80 mm	None	2.8	1.5	3.1
Polema rod Ø 30 mm	2.0	4.1	3.1	5.2-6.7
Polema plate (forged)	3.8	6.4	4.7	7.4
Polema plate (rolled)	None	2.7	1.2	4.1

Table 3.10. Depths of grain growth after cyclic thermal loads. The grain growth per material showed the same tendency under all testing conditions. The largest range was observed in the forged plate and the smallest range in the 80 mm diameter rod and rolled plate. The grain growth depths increased with the cycle number and reached maximum values after 1000 cycles although the temperatures were lower (≤2200°C) than those during the 50 cyclic thermal loads (≥2300°C).

The 12 and 30 mm diameter rod materials, which had similar grain areas before thermal loads (table 3.1 and figure 3.1 in section 3.2), showed similar grain growth ranges. The 80 mm rod, which originally (i.e. before thermal loads) had bigger grain areas compared to the 12 and 30 mm diameter rod materials, showed a smaller grain growth range. The grain area (the grain size in general) could be related to grain growth; the larger the grain size, the smaller the grain growth depth. However, the rolled plate had one of the smallest grain areas and also the smallest grain growth depth. Therefore, the mechanical treatment (i.e. the deformation level during material production) must play the dominant role in the grain growth resistance.

The 60 mm diameter rod showed a particular surface aspect after 50 cycles at 1900°C characterised by (1) an inhomogeneous crack distribution and (2) localised surface melting. The loaded surface could be divided into three regions in terms of surface modification (figure 3.42(a)): region A where cracks only were observed, region B where cracks and surface melting were observed (figure 3.42(b)), and region C without visible surface damage. As shown in figure 3.42(c), the cracks were more apparent in region B than in region A because they were slightly deeper as shown in the cross section views (figure 3.42(d)).

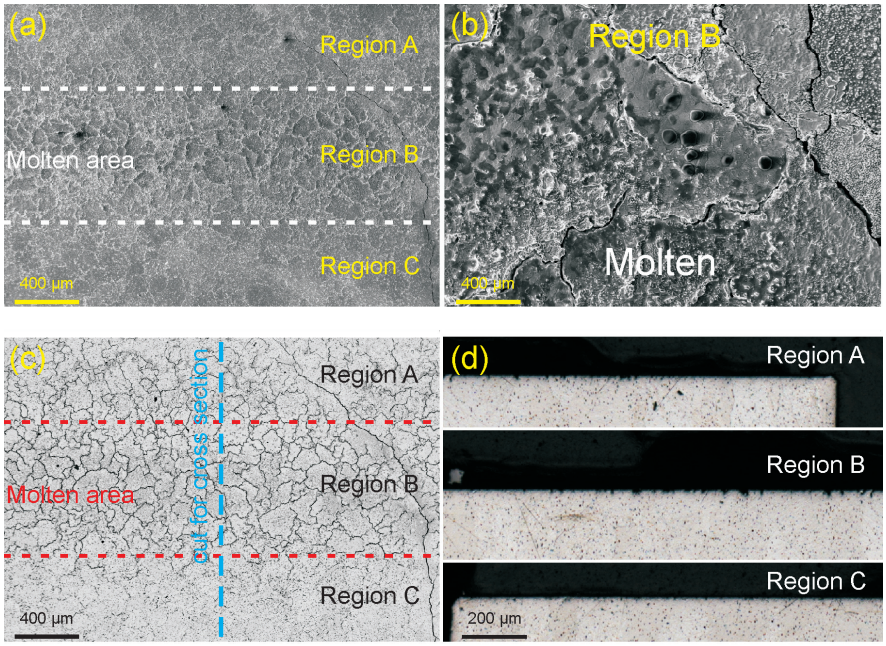

Figure 3.42. (a) and (b) SEM micrographs of the loaded areas of the 60 mm diameter rod (50 cycles, 1900°C) showing three distinct regions in terms of surface damage: region A (cracks), region B (cracks and melting) and region C (no damage). (c) BSE micrograph of the same surface showing wider cracks in region B than in region A. (d) Optical micrographs of the cross section showing deeper cracks in region B than in region A.

In the component's design and fabrication, the blocks #1 (60 mm diameter rod) and #7 (rolled plate) were positioned at the edges of the samples' set. Since no damage was observed on region C, it was assumed that this region was not scanned by the e-beam during the tests. This assumption is reinforced by the fact that region B showed melting, and therefore was overheating as a result of the increased beam loading in the turn-around region of the beam as shown schematically (figure 3.43). Furthermore, it has been observed during the tests that the edge of the adjacent blocks set (the

15 mm thick blocks) was heated, indicating a shift of the loading pattern towards the adjacent block set (the same artefact was observed during the 1000 cyclic thermal loads at 2200°C).

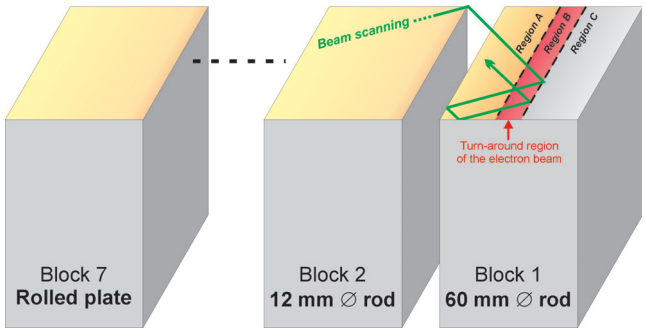

Figure 3.43. Sketch illustrating the sample's overloading in the turn-around region of the electron beam where its dwell time is higher. The overheating in the turn-around region of the electron beam was absorbed by region B, hence the latter showed heavier damages than region A. The electron beam turned before region C, which was not thermally loaded.

Figure 3.44(a) shows the loaded surface after 1000 cycles at 2000°C. Several damage types were observed: (1) surface roughening due to plastic deformation, (2) surface cracking due to tensile forces, (3) particle erosion on the crack path, and (4) material lifting (figure 3.44(a)). Furthermore, cracks opened, reaching an average crack width of

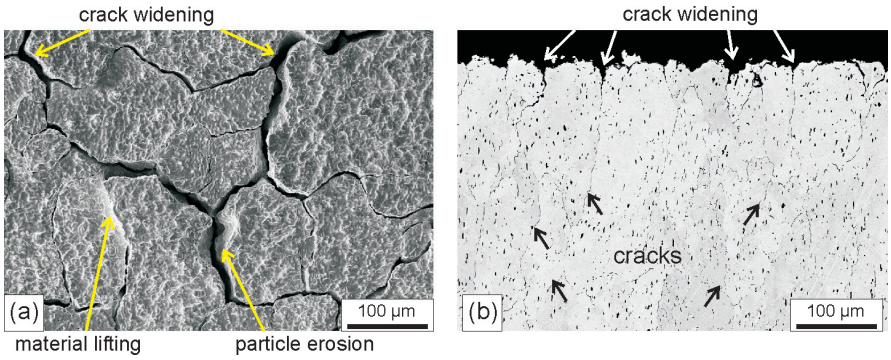

Figure 3.44. (a) SEM micrograph of the loaded surface of the 60 mm diameter rod after 1000 cycles at 2000°C showing particle lifting and erosion, surface roughening and cracking as well as crack opening. (b) BSE micrograph of the cross section of the respective area showing the crack depth, which reached hundreds of micrometers.

about 11 μm and a maximal value of about 23μm. Crack opening took place down to a depth of about 30 μm (average value) as shown in the cross section view (figure 3.44(b)).

The crack depth reached hundreds of micrometers after cracks propagation around the comparably large grains.
At higher temperature (2200°C) the same types of damage were observed; although this was not clear from the top view, the cross section view of the loaded surface showed crack opening (figure 3.45). Due to the increase of temperature the crack opening took

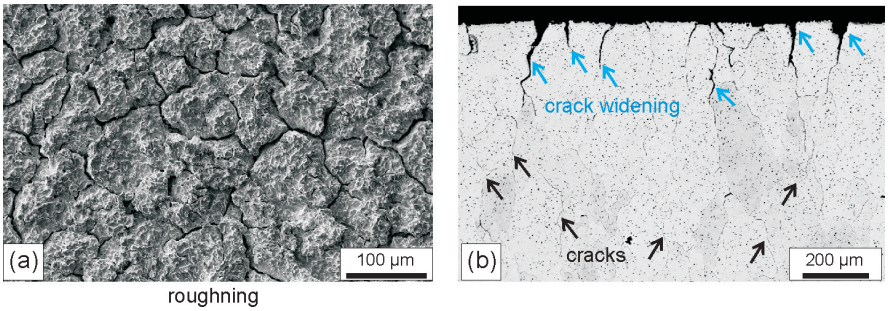

Figure 3.45. (a) SEM and (b) BSE micrographs of the loaded areas (top and cross views respectively) of the 60 mm diameter rod after 1000 cycles at 2200°C showing similar but larger damages than those observed at 2000°C.

place down to a greater depth (∼170 μm, average value). Such crack opening and propagation were not observed after 50 cycles, even at the highest temperature (∼2600°C) as shown before in figure 3.36. Therefore, the increase of the cycle number caused the crack enlargement.

A similar degradation was observed in the pre-cracked sample at the highest surface temperature and cycle number (figures 3.23 and 3.27 in section 3.5.1). This material showed a limited strength under sever loading conditions (1000 cycles, surface temperature ∼2000°C).

Summary

During thermal fatigue loads, cracks occurred in the loaded surfaces due to thermo-mechanical stresses induced by the electron beam. The cracking threshold was below 50 cycles at 1900°C. Cracks due to thermal fatigue loads occurred along grain boundaries. Consequently, cracks followed the grain orientation on the loaded surface (formed curved cracks networks in rods and the forged plate and straight lines in the rolled plate).

The continuous stresses accumulation due to the cycle and temperature increase had no impact on the crack pattern (i.e. crack formation) nor the crack distance (i.e. crack density) in general (below 2200°C). However, the crack depth (i.e. crack propagation) increased with the cycle number. In rod materials, the grain size was large compared to the crack propagation range, and the cracks, which followed the direction of the strong

grain deformation during propagation, were perpendicular to the loaded surface. In the forged plate, the crack propagation range was larger than the grain size and led to crack propagation parallel to the surface and particle erosion.

The W grades showed differences in terms of roughening, cracking, particle erosion and grain growth resistances (damage threshold, damage development rate), which are highlighted in the conclusion of this work.

3.5.3 Comparison of pre-cracked and polished surfaces after thermal loads

Note: this comparative study involved the Plansee materials only.

The table 3.11 summarizes the average crack distances measured in the polished surfaces after 1000 cycles at 2000°C (∼15 MW·m^{-2}) as well as in the pre-cracked surfaces after 1000 cycles at 1600°C (∼16 MW·m^{-2}) and 2000°C (∼11 MW·m^{-2}). At simi-

	Average crack distances (in μm)		
	Polished surfaces	Pre-cracked surfaces	
Materials	2000°C, 15 MW·m^{-2}	1600°C, 16 MW·m^{-2}	2000°C, 11 MW·m^{-2}
Plansee rod Ø 12 mm	78±42	22±12	25±11
Plansee rod Ø 30 mm	72±44	38±30	38±28
Plansee rod Ø 60 mm	188±79	62±32	52±24
Plansee rod Ø 80 mm	246±122	68±28	67±34

Table 3.11. Average crack distances in pre-cracked and polished surfaces after 1000 cyclic thermal loads. The average crack distance was lower in the pre-cracked specimens than in the polished specimens altough the latters were subjected to higher stresses by thermal fatigue.

lar power densities (∼15-16 MW·m^{-2}), the pre-cracked specimens showed lower crack distances (i.e. higher crack densities) than the polished samples although the latter have been tested at a higher surface temperature (∼2000°C versus ∼1600°C). Making another comparison, based this time on the same surface temperature (∼2000°C), pre-cracked specimens showed again higher crack densities than the polished samples although they have been tested at a lower power densities (∼15 MW·m^{-2} versus ∼11 MW·m^{-2}), and therefore exposed to less stresses. Therefore, the EDM process induced more cracks than the cyclic thermal loading (under the present testing configuration and conditions: power density below 15-16 MW·m^{-2}, surface temperature below 2000°C, and 1000 cycles).
In the 12 mm diameter rod material prepared by polishing the surface temperature was higher than 2000°C during the tests because the block was overheating as shown in figure 3.46. However, despite the particularly high temperature on this sample, the crack distance was still higher (i.e. the crack density was lower) than that of the pre-cracked specimen.

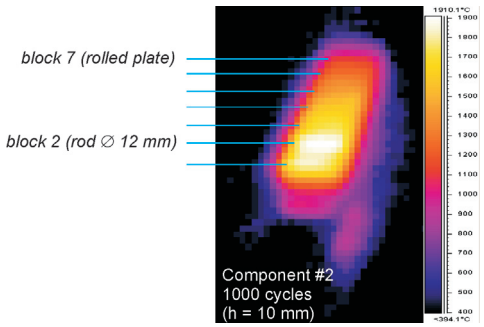

Figure 3.46. Infrared image of the polished specimens (10 mm thick) during cyclic thermal loads (1000 cycles at 2000°C). The 12 mm diameter rod material (block #2) was overheating due to a defective bond to the heat sink.

The crack pattern of the polished surfaces was characterised by continuous curved cracks only after thermal fatigue loads (1000 cycles), whereas that of the pre-cracked surfaces was characterised by continuous curved cracks and discontinuous straight cracks (figure 3.47). Consequently, the crack pattern was less heaped in the polished surfaces (in particular in the 12 mm diameter rod material). Networks formed by discontinuous straight cracks such as those observed on the pre-cracked surface of the 80 mm diameter rod never occurred in the polished specimens.

Inter-granular cracks only were observed in polished samples after thermal fatigue loads, whereas both inter- and intra-granular cracks occurred in the pre-cracked samples (figure 3.48). Typically intra-granular cracks will eventually form in W only if the material "needs" to release more stresses than it died after the formation of inter-granular cracks. No intra-granular cracks were observed in the polished specimens although they have been subjected to higher stresses than the pre-cracked specimens during exposure to thermal loads. Therefore, the intra-granular cracks observed in pre-cracked surfaces were induced by EDM. Thus, the crack density was higher in the pre-cracked specimens because EDM induced cracks (inter- and intra-granular) in W surfaces at regular intervals.

The common feature to the two crack patterns were the continuous curved inter-granular cracks. Intra-granular cracks in the form of discontinuous straight cracks were observed in the pre-cracked samples only.

The average crack depth of the pre-cracked samples was below 40 μm under the most severe loading conditions (16 MW·m^{-2} or 2000°C) as shown in table 3.12. Furthermore, the crack depth did not vary with the temperature nor the cycle number. In contrast to the pre-cracked specimens, the polished specimens had a crack depth that increased with the cycle number. Furthermore, the crack depth was higher in the polished surfaces than in the pre-cracked surfaces.

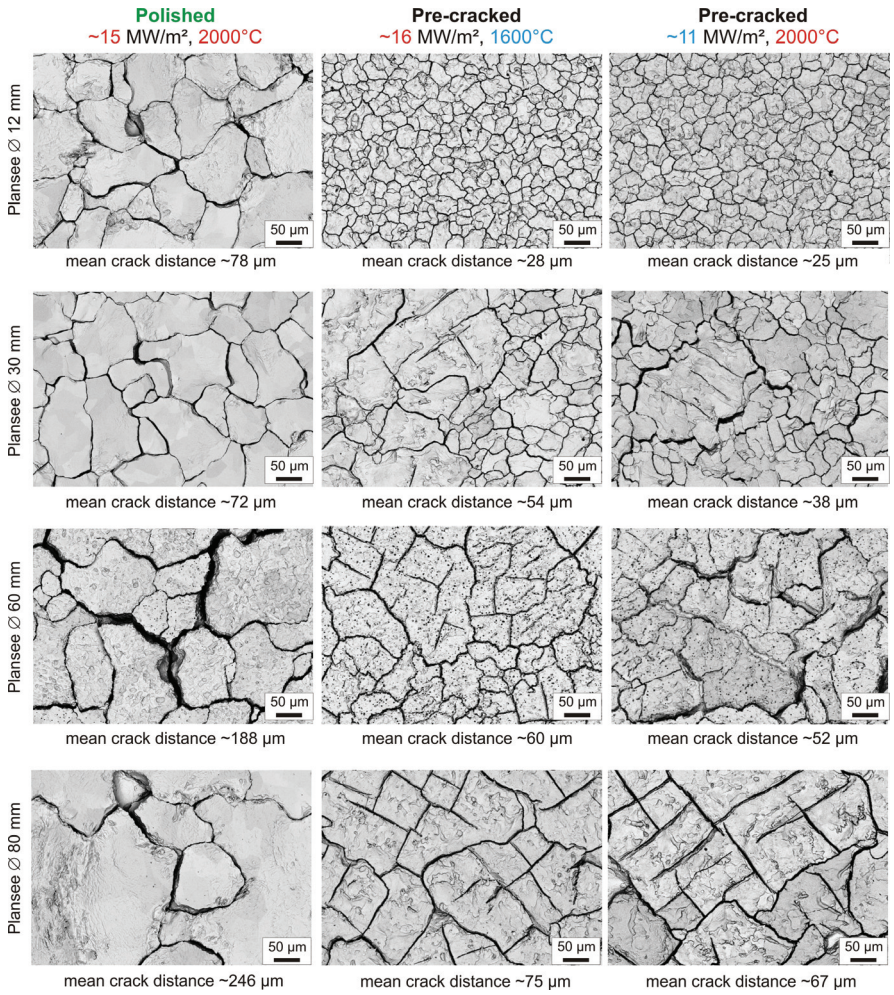

Figure 3.47. BSE micrographs of the loaded areas of both specimen types after 1000 cycles. Discontinuous straight cracks were characteristic of the pre-cracked surfaces as none was observed in the polished surfaces.

	Average crack depths (in μm)		
	Polished surfaces	Pre-cracked surfaces	
Materials	2000°C, 15 MW·m^{-2}	1600°C, 16 MW·m^{-2}	2000°C, 11 MW·m^{-2}
Plansee rod Ø 12 mm	98±27	17±4	19±1
Plansee rod Ø 30 mm	43±18	40±1	24±13
Plansee rod Ø 60 mm	>200 μm	16±8	heavily damaged
Plansee rod Ø 80 mm	73±27	35±4	22±8

Table 3.12. Average crack depths. The crack depth was higher in the polished specimens despite higher stresses in those samples.

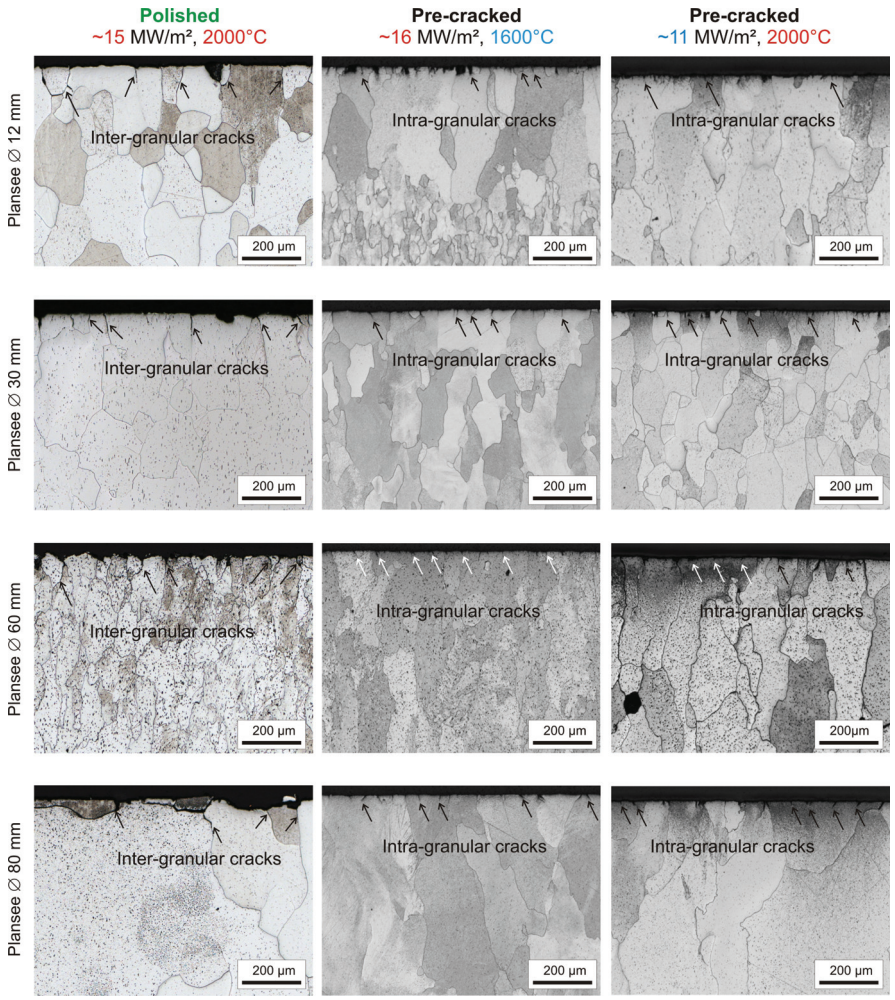

Figure 3.48. Optical micrographs (after etching) of the cross sections of the loaded areas of both specimen types. The cracks in the polished surfaces were mainly inter-granular, whereas both inter- and intra-granular cracks were observed in the pre-cracked surfaces.

The difference in terms of crack depth between the pre-cracked and the polished specimens is well visible on the cross section pictures (figure 3.49). This difference in terms of resistance to crack propagation between the two specimen types could be related to the difference in temperature gradients resulting in higher stresses in the polished blocks (15 $MW{\cdot}m^{-2}$ at 2000°C in the polished samples versus 16 $MW{\cdot}m^{-2}$ at 1600°C or/and 11 $MW{\cdot}m^{-2}$ at 2000°C in the pre-cracked sample). It could also be due to different stress relaxation mechanisms. Typically in W cracks induced by thermal stresses using an e-beam result from compressive and tensile forces. In the pre-cracked specimens,

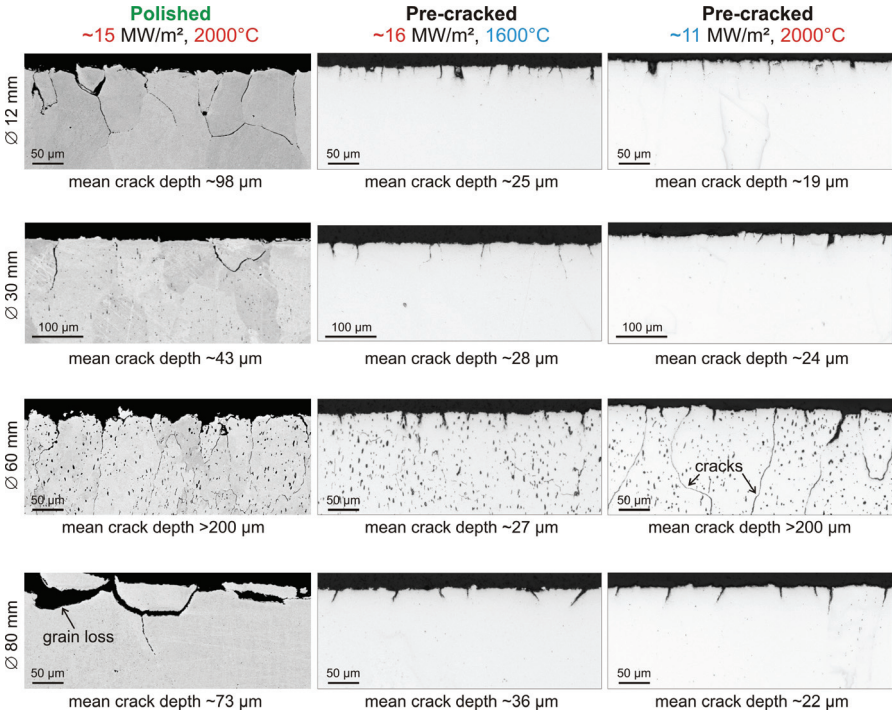

Figure 3.49. (Left) BSE and (middle and right) optical micrographs of the cross sections of the loaded areas of both specimen types showing a higher crack depth in the polished surfaces.

the crack propagation was probably limited by the high crack density as this provided spaces for grains to expand during the heating cycle, this avoiding compressive stresses and plastic deformation, and consequently resulting in less tensile stresses during cooling down. In the polished blocks, the absence of cracks before thermal loading and the preferential formation of cracks at grain boundaries, where the lowest mechanical strength is provided, would lead to more plastic deformation and the necessary stress relief would have manifested itself in crack propagation, explaining the increase of the crack depth with the cycle number (shown in table 3.9 in section 3.5.2).

3.5.4 Performance of the grades under the combined thermal load

After thermal shock loads only

After a single shot with a power density of 0.5 GW·m^{-2} and a pulse duration of 5 ms at room temperature, cracks were observed in all materials as expected (figure 3.50). The failure mechanism was cracking by tensile forces, like for the cracks induced by

thermal fatigue. However, due to the high power density, tensile forces were greater in that case, hence the crack width of the thermal shock cracks was larger (∼5 μm, more than the double).

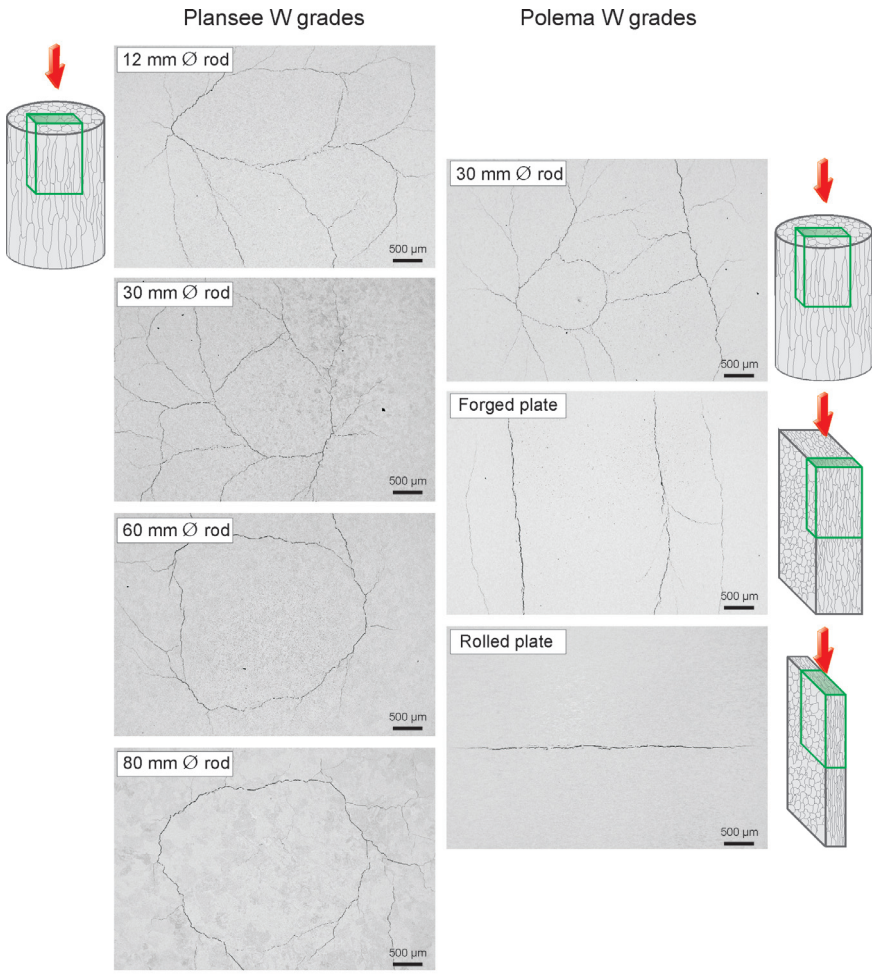

Figure 3.50. BSE micrographs of the top surfaces after one pulse at a power density of 0.5 GW·m^{-2} during 5 ms performed at room temperature showing cracks in all materials.

The cracks were located across the loaded areas. In the rod materials providing no preferential orientation of the grains on the top surface, the cracks tended to describe curves, whereas in the rolled plate characterised by elongated grains, the cracks followed the direction of the grain deformation and were mainly straight.
Beside tensile stresses related fractures leading to cracking, shear forces, either horizontal or vertical, occurred in the material, resulting in the friction of the cracked

surfaces or the lifting of material parts respectively. Furthermore, several places with missing material were found along the crack path indicating the erosion of particles (figure 3.51).

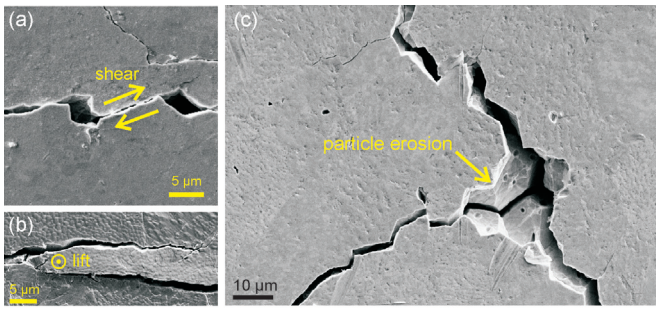

Figure 3.51. SEM micrographs of the top surfaces after one thermal shock pulse (0.5 GW·m^{-2}, 5 ms, RT). In general, cracked surfaces underwent shear forces by (a) horizontal motion (e.g. Plansee 12 mm diameter rod) and (b) vertical motion leading to friction of the cracked surfaces or the lifting of material parts (e.g. Polema rolled plate), respectively. (c) After lifting, material parts were ejected at random positions on the path of the cracks (e.g. Polema 30 mm diameter rod).

After the combined thermal load (synergistic effect)

To evaluate the cracking threshold under the present loading conditions (50-1000 cycles, surface temperatures ∼1000-2200°C, with and without transient load) the components were taken out of the testing facility after 1, 5 and 10 cyclic thermal loads. Cracking by thermal fatigue was observed on the whole loaded surface of the materials after 5 cycles at 1900°C (figure 3.52, the cracking threshold by thermal fatigue found itself between 1 and 5 cycles at 1900°C). Cracks introduced by thermal shock loads had merely no impact on the cracking threshold under thermal fatigue loads.
Table 3.13 shows the average crack distances measured independently on the surfaces subjected to steady-state thermal loads only and on the surfaces subjected to both loading types. As the values were similar on both sides, the surface modifications induced by thermal shock had no impact on the crack formation by thermal fatigue.
Figure 3.53 shows the microstructures of the top surfaces after exposure to thermal fatigue loads, with and without thermal shock loads. The damages (mainly the cracks) induced by thermal shock had no impact on the crack pattern formed by thermal fatigue (network of curved cracks) apart from the characteristic large cracks typically induced by thermal shock loads [95, 128, 133–143]. It also had no impact on the crack orientation (figure 3.54), similar to that observed previously (figure 3.38 in section 3.5.2).
In the areas exposed to the combined thermal load, cracks mainly occurred along the grain boundaries as shown in the cross section views of the loaded areas (figure 3.54) and as observed during thermal fatigue loads only in figure 3.38 in section 3.5.2.

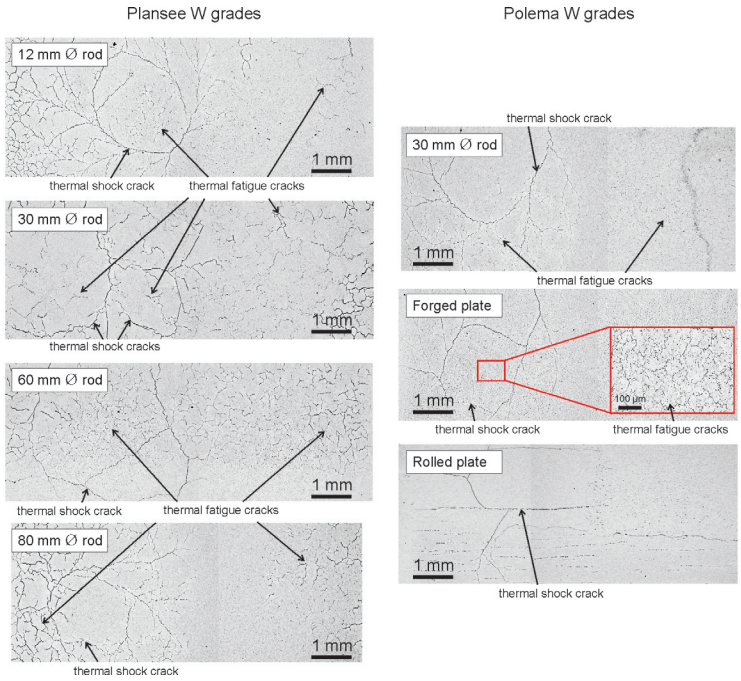

Figure 3.52. BSE micrographs of the top surfaces after a single thermal shock load (0.5 GW·m^{-2}, 1 pulse, 5 ms, RT) followed by thermal fatigue loads (15 MW·m^{-2}, 5 cycles (20 s each), surface temperature of 1900°C). Cracks induced by thermal shock beforehand did not prevent crack formation by thermal fatigue.

	Average crack distances (in μm); TS = thermal shock					
	50 cycles		1000 cycles			
	1900°C		2000°C		2200°C	
Materials	no TS	with TS	no TS	with TS	no TS	with TS
Plansee rod Ø 12 mm	101±48	95±35	78±42	75±34	76±40	93±49
Plansee rod Ø 30 mm	92±36	78±31	72±44	87±26	79±45	103±64
Plansee rod Ø 60 mm	74±37	79±34	189±118	188±101	76±32	81±36
Plansee rod Ø 80 mm	174±101	202±98	246±122	373±245	179±37	199±88
Polema rod Ø 30 mm	74±40	75±33	73±32	101±81	65±29	48±18
Polema plate (forged)	42±19	39±13	63±43	65±25	38±14	38±12
Polema plate (rolled)	21±12	20±411	26±11	28±14	16±6	18±10

Table 3.13. Average crack distances measured on both sides of the loaded surfaces independently. The values were similar on the side exposed to steady-state thermal loads only and on the side exposed to both transient and steady-state thermal loads on the other hand.

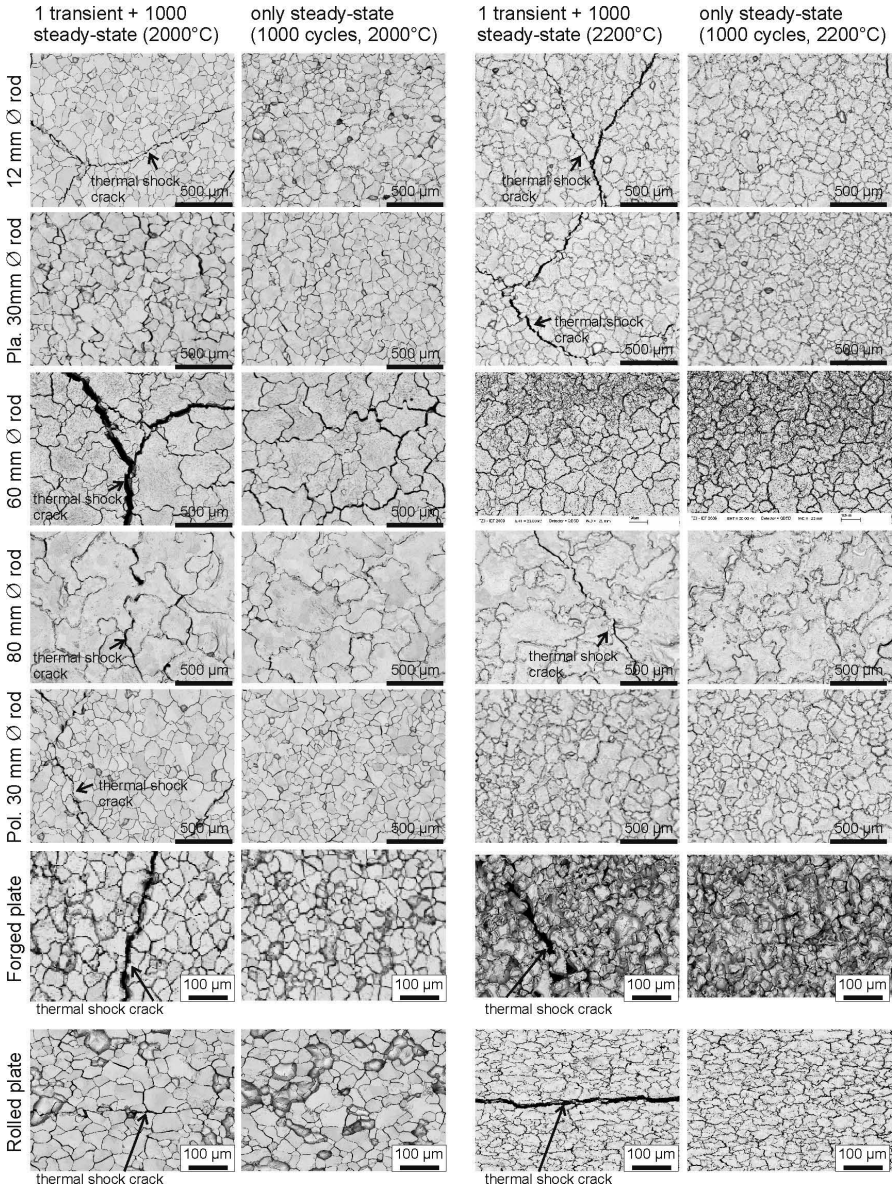

Figure 3.53. BSE micrographs of the top surfaces after 1000 thermal fatigue loads (15 MW·m^{-2}) with and without thermal shock. The damages induced by thermal shock showed no impact on the crack formation by thermal fatigue.

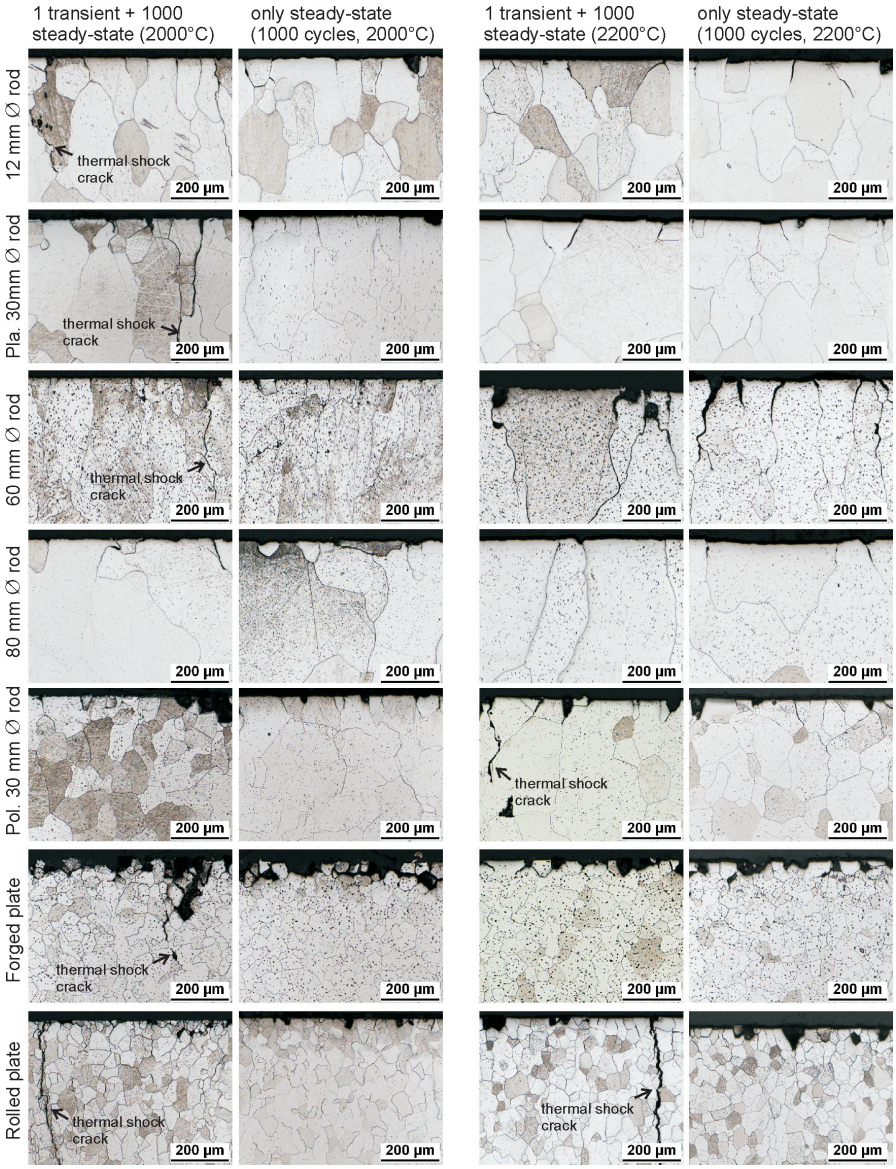

Figure 3.54. Optical micrographs of the cross sections of the top surfaces after 1000 thermal fatigue loads (15 $MW \cdot m^{-2}$) with and without thermal shock. Cracks were inter-granular regardless the loading scheme.

As seen previously in sections 3.5.1 (figures 3.24 and 3.27) and 3.5.2 (figures 3.44 and 3.45) the 60 mm diameter rod was not comparable to the other materials in terms of strength as it heavily cracked after 1000 cycles at high temperature (∼2000°C). This significant cracking was not minimized by the cracks induced beforehand by thermal shock as shown in figure 3.55.

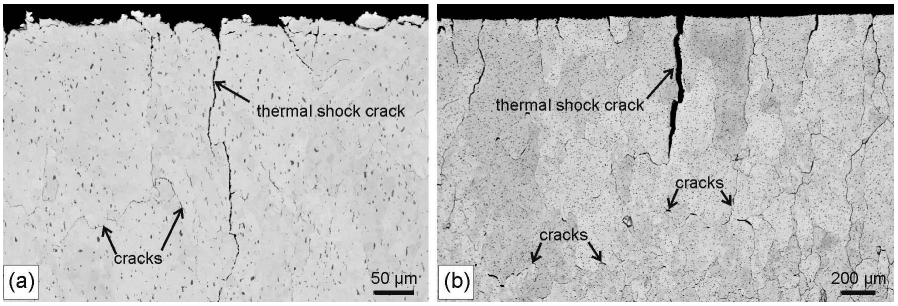

Figure 3.55. BSE micrographs of the cross section of the top surface of the Plansee 60 mm diameter rod after thermal shock and 1000 cyclic thermal loads at (a) 2000°C and (b) 2200°C showing significant damages (crack opening, cavities formation after crack propagation in the bulk, surface roughening) despite the stress relief induced by thermal shock loads' cracks.

Figure 3.56 shows the average crack depths (with standard deviations) of the other materials measured independently on the surfaces subjected to thermal fatigue loads only (1000 cycles) and on the surfaces subjected to the combined thermal loads. The deep cracks typically induced by thermal shock were not taken into account in the measurement of the crack depth to make a fair comparison between the two sides. Despite some small gaps within the values measured at 2000°C, the crack depths measured on both sides of the loaded surface were in general similar. Only the 12 mm diameter rod material exhibited a remarkable crack depth variation at 2000°C (larger crack depth in the area only subjected to steady-state thermal loads) probably caused by the overheating of the block during testing (figure 3.46 in section 3.5.3). It can be concluded that the thermal shock did not show a clear impact on the resistance to crack propagation.

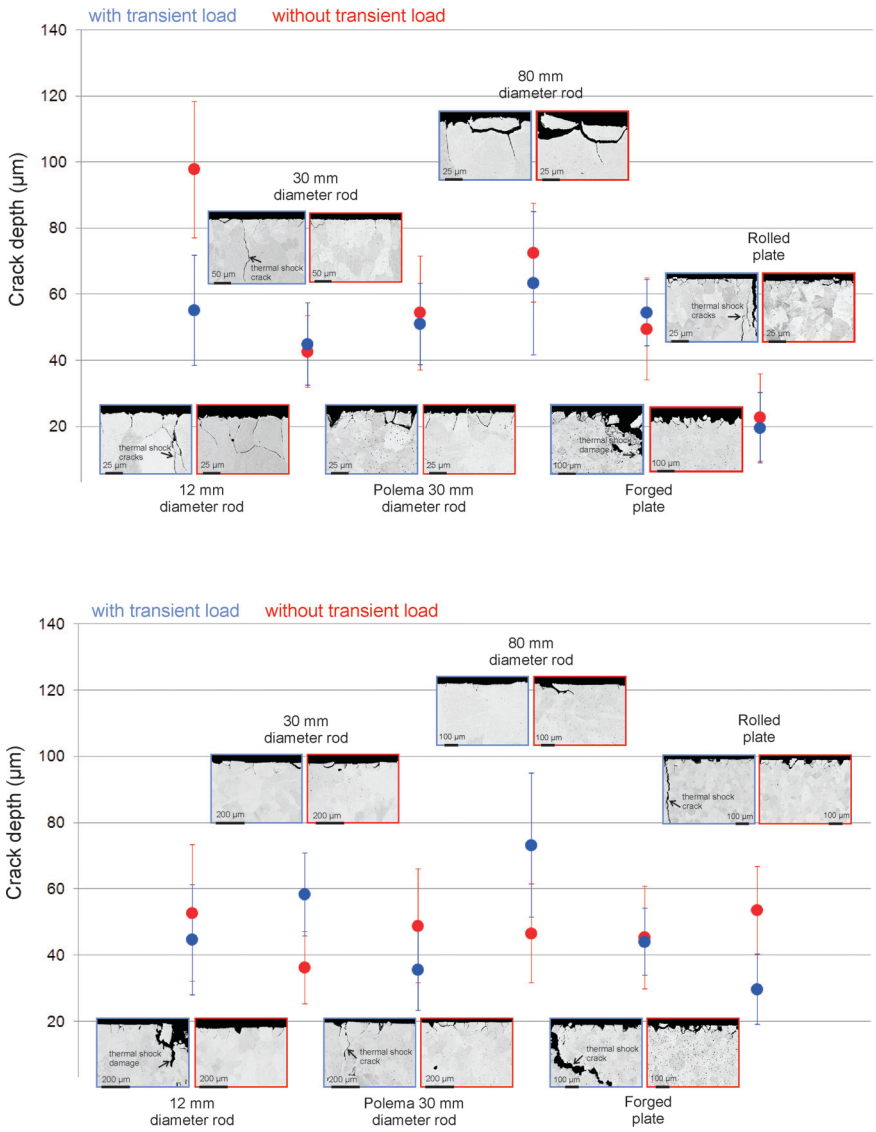

Figure 3.56. Average crack depths (the bars are the standard deviations) measured independently on both sides of the loaded areas after 1000 cyclic thermal loads (top) at 2000°C and (bottom) 2200°C with an without thermal shock. The impact of the damages induced by thermal shock on the crack propagation was not clear3.

4 Summary and conclusions

Failure mode of plasma-facing components for the European DEMO divertor

Based on the examination of the tungsten-armoured plasma-facing components for the helium-cooled DEMO divertor, its viability for a fusion environment and the therein occurring thermo-mechanical loads were strongly related to the choice of the appropriate material as well as joining, design and machining issues.

The helium-cooled components were exposed to cyclic thermal loads with a power density in the range of 9 to 14 $MW \cdot m^{-2}$. With a coolant temperature between 500 and 600°C, the resulting loaded surface temperature was about 1700°C. Thermally induced mechanical stresses led to dense cracks network in the loaded surface as well as crack propagation along grain boundaries. Consequently, cracks followed the direction of the grain deformation. Crack propagation in both the sacrificial plasma-facing part and the structural and heat sink part created a path for helium leakage. It has been observed that the increase of the helium gas' mass flow rate led to a greater cooling efficiency. The resulting lower operation temperature altered the crack development (suppression of the dense cracks network, shallow cracks). Besides, the tungsten grade for the plasma-facing part showed an impact on the resistance to crack propagation as the material from the Polema company (Russian company) showed a lower crack depth than the material from the Plansee company (Austrian company) although it had no castellations (greater thermal stresses) and was subjected to more thermal cycles (i.e. a greater stresses accumulation). Those material issues raised the need of improved tungsten grades with high crack resistance under thermal loads and high thermal stability, namely with a low ductile-to-brittle transition temperature and high recrystallisation temperature.
In the joint between the plasma-facing part (W tile) and the heat sink part (W-1%La_2O_3 thimble) the nickel-based brazing filler metal (STEMET® 1311, brazing temperature = 1050°C) melted during operation and led to further degradation of the component by eroding the tungsten-based materials. In particular the transport of molten brazing metal away from the joint created a thermal barrier preventing any effective cooling of the plasma-facing part. It appeared to be crucial to avoid melting of the nickel-based brazing filler metal. For this purpose one option is to reduce the operation temperature window. Another option is to use a brazing filler metal

with a higher brazing temperature. An attempt was performed with the brazing metal CuNi44 (brazing temperature = 1300°C) but this failed due to an improper filling of the gap between the tile and the thimble during the brazing procedure. Investigations on brazing filler metals are still on-going. An other thermal barrier was created on the inner surface of the heat sink part after the formation of an oxide layer caused by the residual oxygen in the helium-cooling circuit.
In the joint between the heat sink part (W-1%La_2O_3) and the supporting structure (steel) cracks were observed in the as-machined brazing (or casted) layer probably due to manufacturing-induced stress concentrations. During thermal loads, cracks developed and were particularly large in this region due to the large thermal expansion coefficients mismatch between the materials. One should study the possibility, if any, of minimizing crack formation by stress analysis and correlated design modifications.
Before exposure to thermal loads, the machining technique employed for the fabrication of the tungsten parts, namely electric discharge machining (EDM), induced discrete cracks (typically ∼30 μm deep) in tungsten surfaces due to the high brittleness of the material at room temperature. The removal of those cracks by grinding during components manufacturing did not prevent the crack development by thermal fatigue. In combination with pre-existing defects in raw tungsten materials (rods and plates), the EDM-induced cracks could have contributed to further degradation of the plasma-facing part by growing during thermal loads. In order to avoid or minimize cracks after EDM, optimised machining processes providing high quality tungsten surfaces must be found. It has been demonstrated that conventional techniques such as milling and turning are reliable for the machining of accessible tungsten surfaces while diamond wire cutting as well as cutting wheels made of diamond or cubic boron nitride were suitable for the shaping of closed (i.e. non-accessible or poorly accessible) surfaces (see appendix A).

Performance of tungsten grades under steady-state thermal loads

A tungsten grades qualification program has been performed to investigate and compare the performance of various pure tungsten materials under steady-state thermal loads. For this program, tungsten grades from Polema and Plansee were selected. The production route of each material was specific as at least one parameter always differs from a material to another: the provenance, the form of the raw product (rod or plate), the diameter of the rod, and the deformation process (forging or rolling). A total of seven tungsten grades, with and without pre-cracking, were investigated under cyclic thermal fatigue loads with power densities between 11 and 19 $MW \cdot m^{-2}$ and surface temperatures between 1000 and 2600°C.
Three materials distanced themselves from the others. Among them the Russian rolled plate with grains oriented perpendicular to the heat flux showed the highest cracking threshold (the only material that showed no cracks after 5 cycles at 1900°C). It also showed the highest resistance to crack propagation (the only material that showed no cracks network on the loaded surface after 50 cycles indicating that cracks did not

propagate around grains completely, and it had the lowest crack depth of all). Furthermore, this grade showed the highest roughening threshold (no roughening on the loaded surface after 1000 cycles at 2000°C). Finally, it showed the greatest recrystallisation resistance (lowest grain growth depth). On the contrary, the Russian forged plate with no particular grain orientation and the smallest grain size of all showed a significant particle erosion. The reason was that the crack depth range was greater than the grain size and as a result it led to crack propagation parallel to the loaded surface and subsequent ejection of particles. During the first cyclic thermal loads the erosion took place at random positions but the accumulation of thermal stresses led to complete surface erosion at high cycle number. The horizontal cracking created a thermal barrier leading to surface melting. The Plansee rod with a diameter of 60 mm with grains oriented parallel to the heat flux showed a significant degradation at high cycle number (1000 cycles) and temperature (above 2000°C) characterized by large crack opening and crack propagation (hundreds of μm) indicating a low cracking resistance (independently of the surface quality). Cracks propagated along grain boundaries around the comparably large grains, the second largest grain size of all. After propagation the cracks opened in the bulk leading to the cavity formation. Such degradation could be related to the high porosity of the material.

The other materials, namely the 12 mm, 30 mm (Plansee and Polema) and 80 mm diameter rods performed similarly. They all showed similar surface roughening and cracking thresholds (less than 5 cycles at 1900°C). As the orientation of the grain deformation (which defines the cracking pattern and the crack propagation direction) of those materials was the same (perpendicular to the loaded surface), their cracking patterns were also identical (curved cracks' network, orientation of the crack propagation perpendicular to the loaded surface). The crack depth of those materials was shallow ($\sim$30 μm) after 50 cycles and 1000 cycles ($\sim$45-55 μm).

One additional feature was incorporated into this program: the study of the impact of machining-induced surface modifications on the materials' thermal response. Thus, both specimens with defect-free surfaces (obtained by mirror polishing) and specimens with cracked surfaces (obtained by electric discharge machining) were thermally loaded and compared. Pre-cracked surfaces showed two distinct types of crack, namely continuous curved cracks and discontinuous straight cracks already before thermal loads, whereas polished surfaces showed continuous curved cracks only after thermal loads. Cross section observations showed that continuous curved cracks occurred along grain boundaries (inter-granular) and discontinuous straight cracks occurred inside of grains (intra-granular). Furthermore, the crack distance was smaller in pre-cracked specimens, indicating that EDM induced a higher crack density than stresses induced by the electron beam loading (under the present design and testing configuration). The crack depth of the polished specimens increased with the cycle number and became higher than the crack depth of the pre-cracked specimens that remained constant ($\sim$30 μm) despite the accumulation of thermal stresses. Therefore, in pre-cracked surfaces, the

crack propagation was limited by the high crack density as this provided enough space for grains to expand during the heating cycle, thus avoiding the compressive stresses and plastic deformation, resulting in less tensile stresses during cooling down. On the contrary, polished surfaces led to more plastic deformation during thermal loads and the stress relief manifested itself in crack propagation.

The polished specimens were also subjected to thermal shock loads (before thermal fatigue loads). The purpose of the combined load was to introduce cracks in the materials (by thermal shock) and study the further development of the damage under thermal fatigue loads in terms of (i) surface temperatures and (ii) initial surface damage. The cracks pre-induced in all materials by a single pulse thermal shock induced by thermal fatigue afterwards.

A Appendix: machining qualification program for tungsten

Material scientists are continuously looking for materials that can operate at elevated temperatures and under harsh environmental conditions. On the other hand, design engineers who choose the materials are specifying low tolerances and better quality finishes. Indeed, to reach high performance, reliability and functionality of the plasma-facing components, excellent material surfaces are required. Thus, the need for efficient and highly accurate machining processes is as important as the development of the material itself if practical applications are ever to be found. W is a very attractive material for nuclear fusion applications but its drawbacks, namely its high hardness and brittleness at room temperature, make the fabrication of W parts a challenging task that requires special handling and skill.
A machining qualification program was performed to find suitable machining techniques (i.e. providing high quality surfaces) for W and consequently alternatives to electric discharge machining (EDM). In the frame of this program, W parts were manufactured using different machining techniques and the machined surfaces were analysed by metallography and material characterisation.

A.1 Machining techniques

The machining techniques employed in this program were all based on the material-removal process (W was in the form of rod or plate before being cut). The machining methods were turning, milling, wheel and diamond wire cutting. State-of-the-art techniques like powder injection moulding (PIM) are also being investigated [144, 145].

Turning

Turning is a conventional cutting process that requires a turning machine (also called lathe), a workpiece, a fixture, and a cutting tool. The workpiece is secured to the fixture which itself is attached to the turning machine and allowed to rotate at high speeds. The cutter is typically a single-point cutting tool that is also secured in the machine. The cutting tool feeds into the rotating workpiece with a motion parallel to the axis of rotation and cuts away material in the form of small chips to create

the desired shape. The depth of cut is the material thickness that is removed as the workpiece is being machined (figure 1.1).

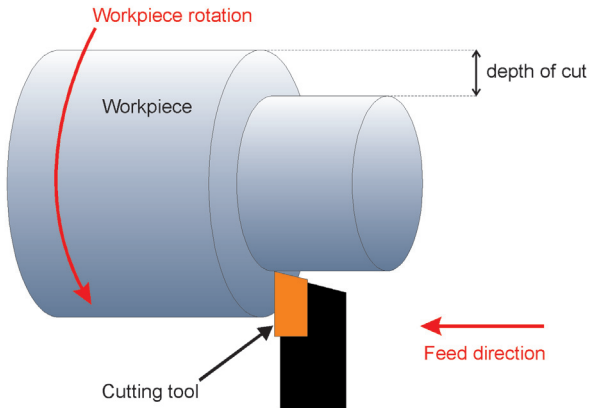

Figure 1.1. Scheme of the turning process.

Turning enables to produce cylindrical external surfaces (i.e. contoured surfaces) as well as flat surfaces when the cutting tool is fed perpendicular to the axis of rotation (i.e. across the face of the workpiece), then speaking about facing, a variant of turning.

Milling

Milling is a common cutting process that employs a milling machine, a workpiece, a fixture, and a cutting tool. The cutter (or miller) is typically a multi-point cutting tool or a cutter with sharp teeth that rotates at high speeds (in opposition to turning). By feeding the workpiece into the rotating cutter the material is cut away from this workpiece in the form of small chips to create the desired shape. One can distinguish two types of milling: *front milling* when the cutter rotates about an axis perpendicular to the surface of the workpiece and *peripheral milling* when the axis of rotation is parallel to the surface (figure 1.2).
Milling may be used with or without coolant. A characteristic of dry milling is the use of compressed air instead of coolant and a higher cutting speed combined with a smaller depth of cut. Due to the lack of coolant heat is induced to the system. The heat removal is realized by the chips that dash away glowing while the bulk material stays cool. The advantage of dry milling is the production speed, four times faster compared to wet milling [147].

Diamond wire cutting

A wire saw is a machine using a metal wire as cutting tool. The two ends of the wire are tightly wrapped round distant pulleys fixed to the machine in such a way that the

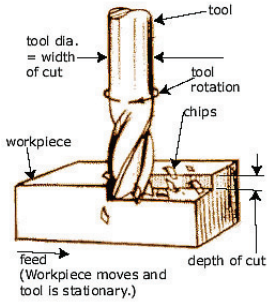

Figure 1.2. Scheme of the peripheral milling process [146].

center part of the wire is kept into tension. The unidimensional motion of the wire is ensured by the rotation of the pulleys around their axis (acting like the spindle in turning and milling). The pulleys rotate continuously in one direction or oscillate. The workpiece is fixed to a support which moves perpendicular to the motion of the wire (figure 1.3).

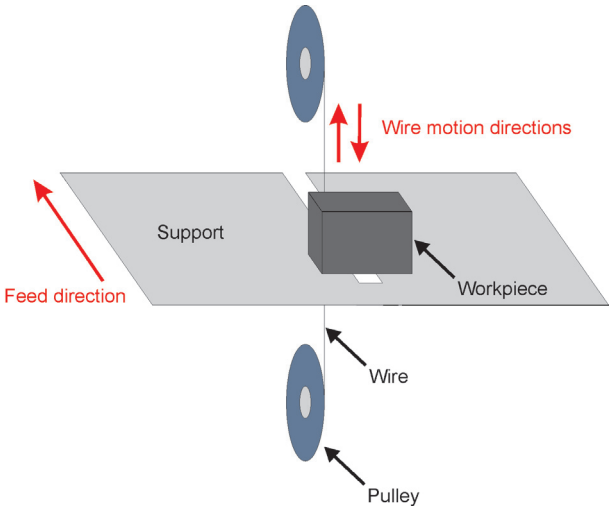

Figure 1.3. Scheme of the wire cutting process.

In diamond wire cutting the wire is impregnated with diamond dust to cut through materials. Because of the hardness of diamonds this cutting technique can cut through almost any material that is softer than the diamond abrasive.

Cutting wheels

Instead of a wire, a cutting wheel (or disc) may also be used as cutting tool. While the workpiece is secured to a fixture, the fast rotating disc feeds into the workpiece to

make a straight cut (figure 1.4). In this work, wheels made of diamond or cubic boron nitride (CBN) were used.

Figure 1.4. View of a working diamond cutting wheel with water coolant to remove chips [120].

A.2 Machining parameters

Several W pieces (or tiles) were fabricated using the **turning** and **milling** processes. Each tile comprised a hexagonal part on top of a bowl-like part with concave surfaces (figures 1.5). The tiles were about 20 mm wide and 12 mm thick. The top surface of the tile was flat whereas the bottom (the bowl-like part) was drilled (hollow) and round inside. This geometry enabled to see on one single tile the impact of both machining

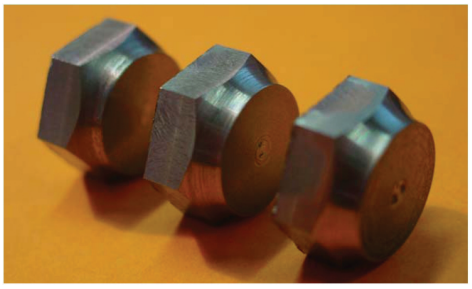

Figure 1.5. Tiles shaped by turning and milling, before the drilling of the bottom part [148].

processes on both flat and curved surfaces. Indeed, the tiles can be divided into five surfaces of interest: three flat surfaces (A, B, and D) and two surfaces with curved outlines (C and E) as shown in figure 1.6). The material used for the tiles's fabrication

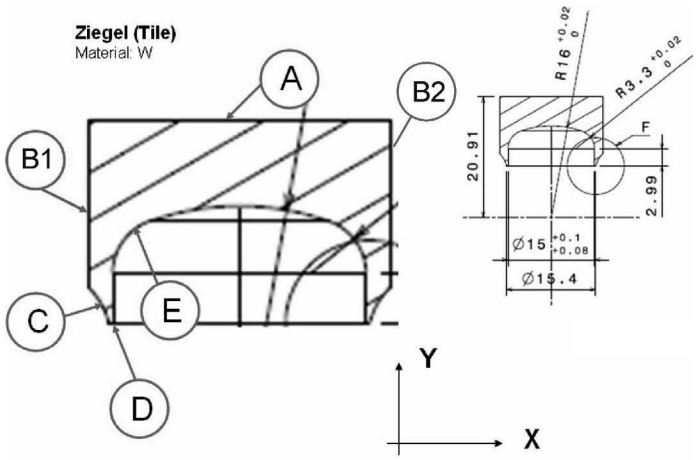

Figure 1.6. Scheme of the cross section of a tile showing the five surfaces of interest: flat surfaces A, B, and D; curved surfaces C and E [148].

was a forged rod. The direction of the grain deformation was perpendicular to the top surface of the tile (surface A) (figure 1.7).

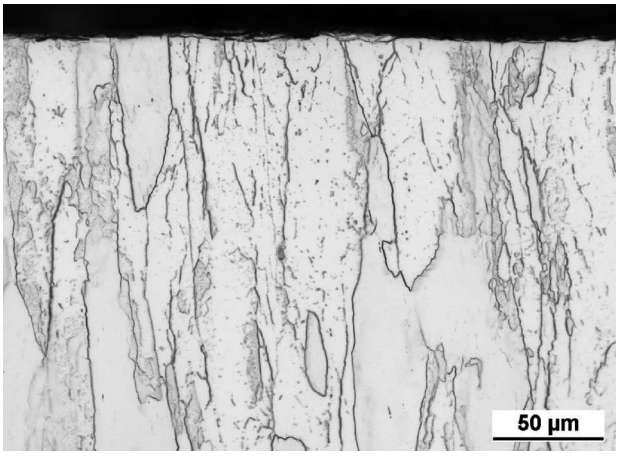

Figure 1.7. The grain orientation was perpendicular to top surface (surface A).

Four series of tiles were fabricated (table A.1). Series 1 and 2 enabled to study turning and milling with respect to the shape (flat or curved) of the surfaces. The difference within those two series lied in the shaping of the surface B by either front (series 1) or peripheral (series 2) milling and the surface E by either turning (series 1) or milling (series 2). Water-cooling was used during machining to remove chips resulting from cutting. Series 3 and 4 were exclusively dedicated to the milling process. In series 3 the axis of rotation of the cutting tool was changed to parallel to the grain orientation

(radial grain orientation) to study the impact of machining with respect to the grain orientation. In series 4 the machining process was performed without cooling.

Surfaces	Series 1	Series 2	Series 3	Series 4
A	Turning	Per. milling (radial)	-	Per. milling (dry)
B	Front milling	Turning	Per. milling (axial)	Front milling (dry)
C	Turning	Turning	-	-
D	Turning	Turning	-	-
E	Turning	Front milling	-	-

Note: within series 1 and 2 several tiles were manufactured per series and the cutting tool was not systematically changed before the machining of new tiles whereas within series 3 and 4 only one tile was examined per series, always manufactured with a new cutting tool.

Table A.1. Series of tiles fabricated for the assessment of turning and milling with respect to the surface morphology (series 1 and 2), the grain orientation (series 3) and the cooling option (series 4).

Thus, turning and milling techniques were investigated with the following features:

- turning of flat surface with radial grain orientation and curved surface
- front milling of flat surface with radial grain orientation and curved surface
- peripheral milling of flat surface with radial grain orientation
- peripheral milling of flat surface with axial grain orientation
- front milling without coolant
- peripheral milling without coolant

Tiles were manufactured using the turning machine center Traub TNA 300 (figure 1.8) and in the milling machine DMU 50 evolution (figure 1.9).

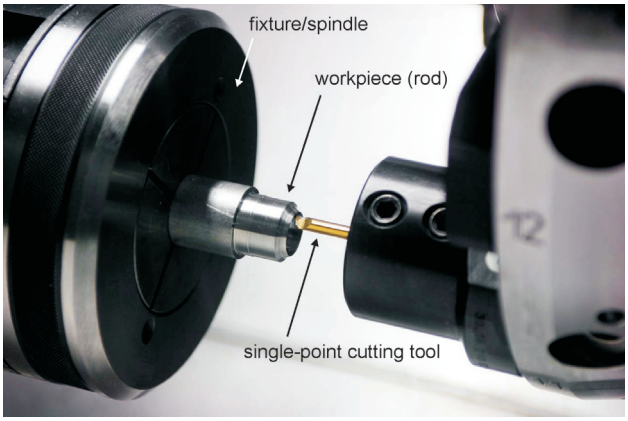

Figure 1.8. View of the inside of the turning machine showing the rotating workpiece fed into a single-point cutting tool [120].

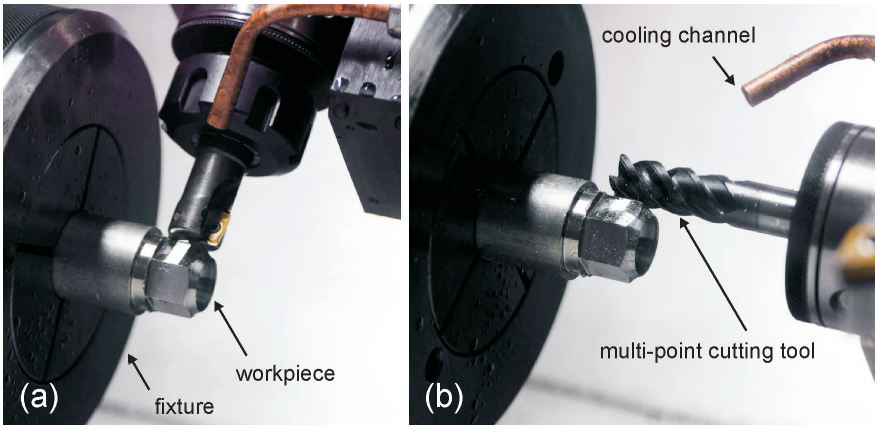

Figure 1.9. View of the inside of the milling machine showing the shaping of workpieces by multi-point cutting tools rotating with an axis (a) perpendicular (front milling) or (b) parallel (peripheral milling) to the machined surface [120].

For the assessment of the surface quality obtained with the other techniques, namely wheel and wire cutting, the approach was simpler. For **cutting wheels** (1 mm thick), slots (or castellations) were machined directly perpendicular to the top surface (surface A) of the tiles. For **cutting with the diamond wire** (1 mm diameter), a groove was machined on a separate W piece.

A.3 Results (examination of machined surfaces)

The surface quality was examined by metallography. A cut was performed perpendicular to the top surface along the full length of the tile for the examination of the cross section.

A.3.1 Turning and milling

Flat surfaces and rotation axis of the cutting tool perpendicular to grain orientation (series 1 and 2)

Flat surfaces machined by *turning* showed two distinct surface aspects depending on the tool quality: smooth surfaces (R_a=0.83 μm) without any defect in tiles machined with a brand new tool (figure 1.10(a)) or rough surfaces (R_a=0.89 μm) with very tiny grooves in tiles machined with a worn tool (figure 1.10(b)). The newer the tool, the smoother the surface, as the cutting tool was deteriorated after several passes.

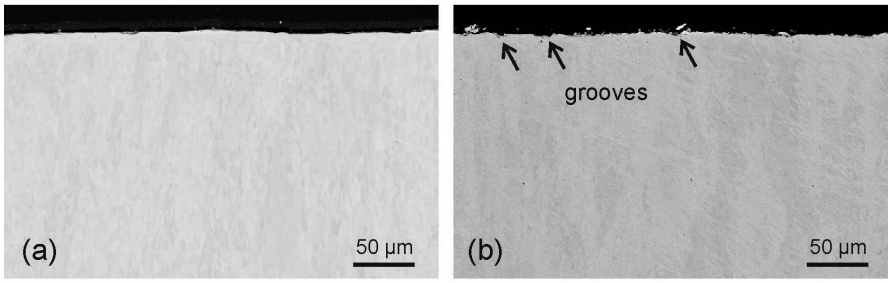

Figure 1.10. BSE micrographs of the cross sections of flat surfaces machined by turning using (a) a new tool (smooth surface) and (b) a worn cutting tool (tiny grooves and rougher surface). The cutting tool was damaged after several passes in W, leading to a decrease of the surface quality.

Each flat surface machined by *front milling* showed an irregular quality, from smooth areas without no particular defects to others with grooves, bumps and cracks parallel to the machined surface (figure 1.11).

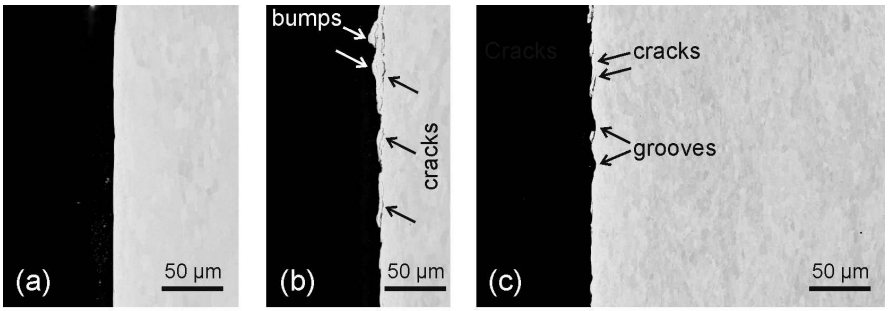

Figure 1.11. BSE micrographs of the cross section of one flat surface machined by front milling. The surface showed on one hand (a) areas with no particular defect, and on the other hand (b) and (c) areas with cracks, bumps and grooves.

Flat surfaces machined by *peripheral milling (radial)* also showed an irregular quality with on the one hand areas without defect (figure 1.12(a)) and on the other hand areas with a few shallow grooves and tiny cracks parallel to the machined surface (figure 1.12(b)).

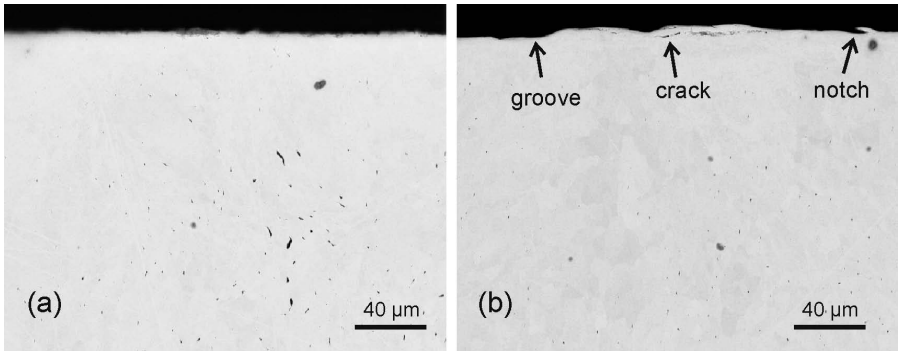

Figure 1.12. BSE micrographs of the cross sections of flat surfaces machined by peripheral milling (radial) showing (a) no defects and (b) shallow grooves as well as tiny cracks parallel to the machined surface.

Flat surfaces and rotation axis of the cutting tool parallel to grain orientation (series 3)

Within one single tile flat surfaces machined by *peripheral milling (axial)* showed two different aspects depending on the side of the hexagonal part (B1 or B2). One side showed no defects whereas the other side showed bumps and cracks. As the sides of the hexagonal part were machined one after the other the miller was probably deteriorated during the machining of the tile. Another tile manufactured with a new miller showed

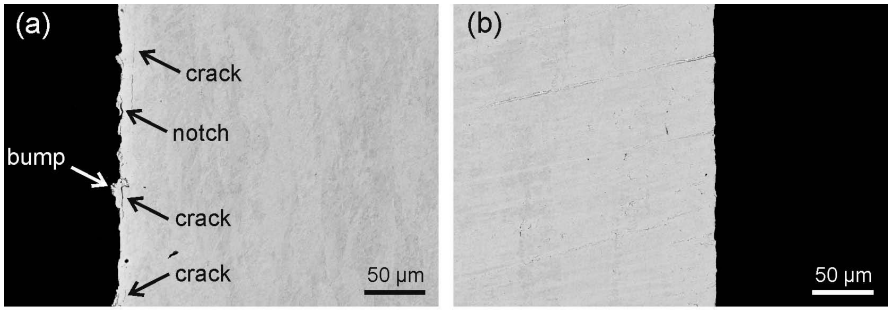

Figure 1.13. BSE micrographs of the cross sections of flat surfaces machined by peripheral milling (axial) showing (a) bumps and cracks and (b) no defect. The surface quality varied from a face of the hexagonal part to an other due to the tool's degradation during machining of the tile.

smooth surfaces without defect (figure 1.14). As in turning, the wear of the cutting tool led to an increase of the surface roughness.

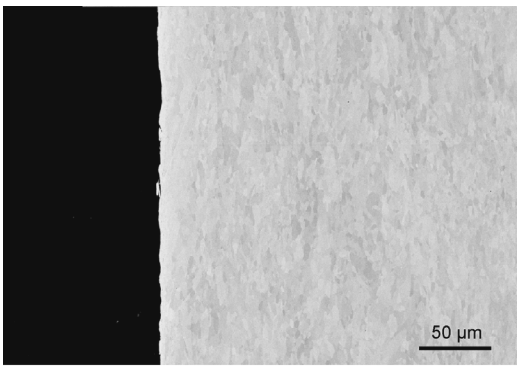

Figure 1.14. BSE micrograph of the cross section of a flat surface machined by peripheral milling (axial) equipped with a new cutting tool. The surface was smooth and did not show any obvious defect such as bumps or cracks characteristic of surfaces machined with a worn tool.

Flat surfaces without coolant (milling only)

As a new cutting tool was employed during *dry milling* so that the quality of the machined surface was comparable to the best surface quality obtained by milling with coolant. In general, the surfaces machined by dry milling showed similar damages as those induced by milling with coolant (cracks parallel to the surface, notches and grooves). Also, the quality was irregular within one single side. There was no visible difference in terms of surface aspect between front and peripheral milling (figure 1.15).

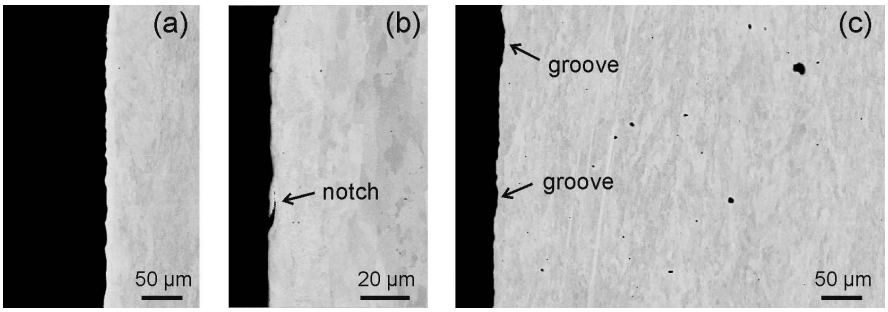

Figure 1.15. BSE micrographs of the cross sections of surfaces machined by (a) front and (b) peripheral milling without coolant. Similar defects than those induced by wet milling were observed.

It took 2 hours to machine a tile by wet willing and 30 minutes by dry milling [147]. Furthermore, in case of dry milling, the machined surface was not contaminated by the coolant.

Curved surfaces

Curved surfaces machined by *turning* revealed a sawtooth structure. To machine curved surfaces by turning it is necessary to define a series of increasing (or decreasing) depths of cut to obtain a round shape eventually; a repositioning of the cutting tool was required after each setting of the depth of cut. The sawtooth structure that appeared at the curvature was the result of this constant tool's adjustment (figure 1.16). Near the "teeth", cracks and tiny cavities were observed, indicating a weakening of the material in this region (figure 1.17). On the contrary, curved surfaces machined by *front milling* were smooth and almost defect-free (figure 1.18).

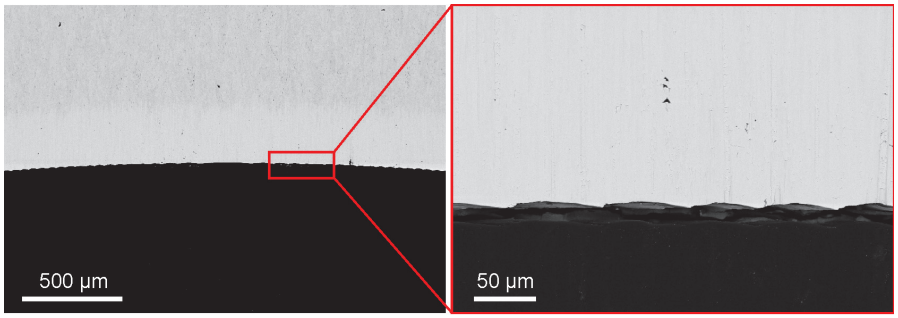

Figure 1.16. BSE micrographs of the cross section of a curved surface machined by the turning process showing a sawtooth aspect.

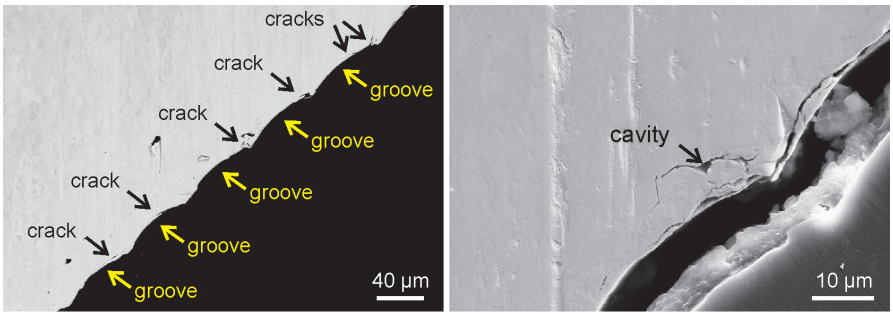

Figure 1.17. BSE micrographs of the cross section of a curved surface machined by turning showing the defects at the vicinity of the "teeth".

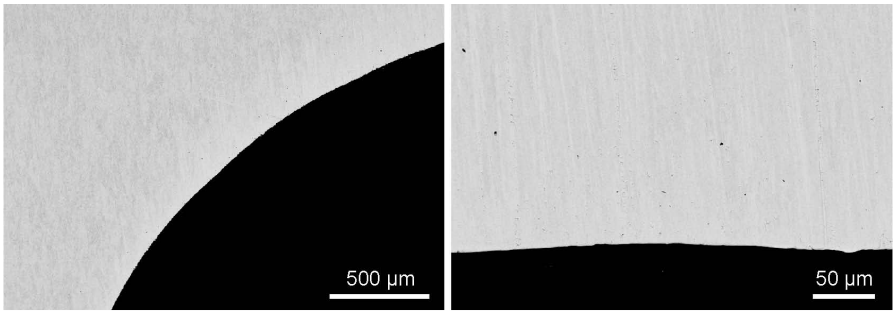

Figure 1.18. BSE micrographs of cross section of a curved surface machined by milling showing no defects.

A.3.2 Cutting wheels

Slots machined with a diamond or CBN cutting wheel displayed good surface qualities as shown in figure 1.19. There was no visible difference in surface aspect as far as flat surfaces were involved. The curved region (at the bottom of the slots) machined by the CBN cutting wheel was not as round as that machined by the diamond cutting wheel. The diamond cutting wheel seemed slightly less abrasive but overall smooth surfaces without defect were obtained with both diamond and CBN materials.

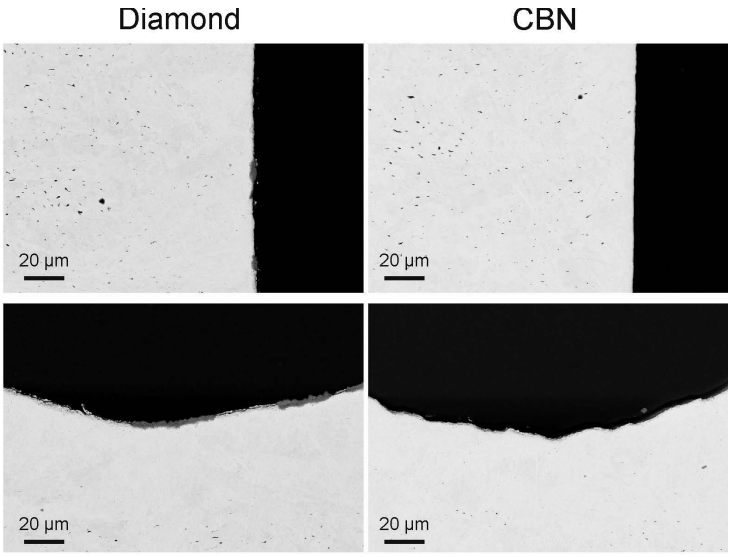

Figure 1.19. BSE micrographs of cross sections of slots machined by cutting wheels showing smooth contours without defect.

A.3.3 Diamond wire cutting

The surface of the groove machined by diamond wire cutting showed a very smooth contour. Only a few tiny defects (notches) were detected at random positions (figure 1.20).

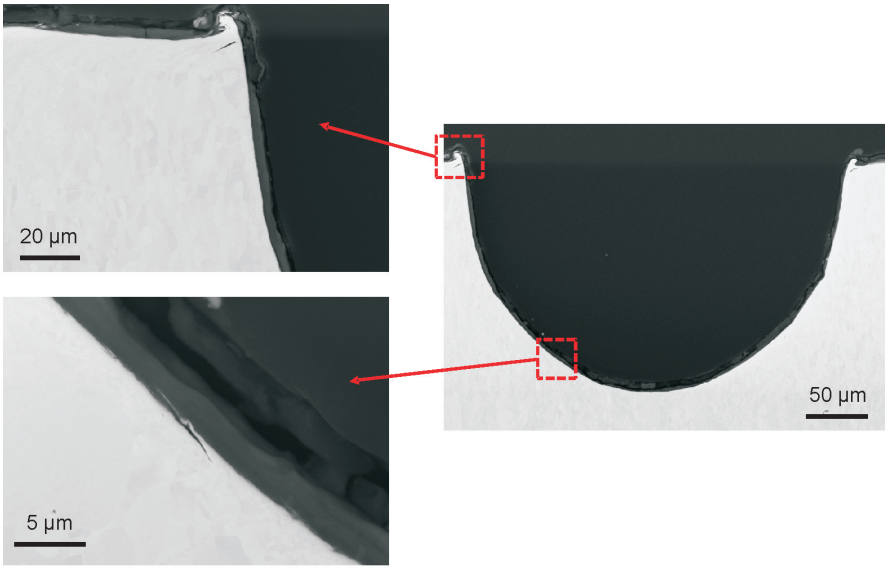

Figure 1.20. BSE micrographs of a cross section of the groove made by diamond cutting wire showing tiny defects only.

Defects in closed (i.e. poorly or non-accessible) surfaces such as castellations may be removed by a non-conventional finishing technique called electro-chemical machining (ECM) [149–152].

A.4 Summary and conclusions

Turning and milling (with coolant) produced flat smooth surfaces without defect as long as a new cutting tool was employed. In both techniques the wear of the tool led to the degradation of the surface quality and increase of the surface roughness. Minor defects such as notches, cracks (parallel to the machined surface), grooves and bumps were observed.

There was no difference of quality between front and peripheral milling. Both milling variants induced the same types of defect. There was no measurable change of the surface quality as a function of the grain orientation. The suppression of the coolant had no impact on the high quality of the surface.

For curved surfaces' machining, turning induced a sawtooth structure and locally damaged the material whereas milling delivered smooth and almost defect-free surfaces. Overall turning and milling were both cleat-cut processes suitable for the fabrication of high quality W parts. Milling distanced itself from turning in the machining of curved surfaces as it does not produce saw-tooth structures in contrast to turning.

Wheel cutting as well as diamond wire cutting were both clean-cut processes as well, leading to smooth surfaces regardless of the grain orientation and the surface shape. A few minor defects were detected in the surfaces machined by these processes but nothing comparable to the characteristic cracks observed in surfaces machined by EDM.

Table A.2 summarizes the surface quality achieved with the different machining techniques.

Machining techniques	Flat surfaces	Curved surfaces	Closed surfaces
Turning	+	-	
Front milling	+	+	
Peripheral milling (radial)	+		
Peripheral milling (axial)	+	+	
Milling (dry)	+		
Diamond wire	+	+	+
Cutting wheels	+	+	+

+: good quality, -: minor defects

Table A.2. Quality of flat, curved and closed surfaces achieved by turning, milling, diamond wire cutting and cutting wheels.

Turning, milling, and EDM may be used to machine open surfaces. One has to take into account that the use of EDM requires an additional surface finishing if one wants to obtain smooth defect-free surfaces, whereas finishing may be optional when using the turning and milling processes.

Turning and milling cannot be used for the shaping of closed surfaces such as castellations ($\sim$1 mm narrow) as their respecting tools are too large. For closed surfaces, EDM, diamond wire saw and cutting wheels can be employed. Diamond wire cutting and cutting wheels appeared as a good alternative to EDM with respect to surface quality.

Bibliography

[1] M. Fewell, "The atomic nuclide with the highest mean binding energy," *American Journal of Physics*, vol. 63, pp. 653–658, 1995.

[2] S. Glasstone and R. Lovberg, "Controlled thermonuclear reactions," 1960.

[3] F. Ajzenberg-Selove, "Energy levels of light nucleai A = 5-10," *Nuclear Physics A*, vol. 490, pp. 1–225, 1988.

[4] "JT-60U Experimental Report No. 36 (August 19, 1996)."

[5] "http://www.ipp.mpg.de." Max-Planck-Institut fuer Plasmaphysik (IPP).

[6] J. Roth, E. Tsitrone, A. Loarte, T. Loarer, G. Counsell, R. Neu, V. Philipps, S. Brezinsek, M. Lehnen, P. Coad, C. Grisolia, K. Schmid, K. Krieger, A. Kallenbach, B. Lipschultz, R. Doerner, R. Causey, V. Alimov, W. Shu, O. Ogorodnikova, A. Kirschner, G. Federici, A. Kukushkin, and EFDA PWI Task Force, ITER PWI Team, Fusion for Energy, ITPA SOL/DIV, "Recent analysis of key plasma wall interactions issues for ITER," *Journal of Nuclear Materials*, vol. 390–391, pp. 1–9, 2009.

[7] P. Lang, A. Degeling, J. Lister, Y. Martin, P. M. Carthy, A. Sips, W. Suttrop, G. Conway, L. Fattorini, O. Gruber, L. Horton, A. Herrmann, M. Manso, M. Maraschek, V. Mertens, A. Mueck, W. Schneider, C. Sihler, W. Treutterer, and H. Zohm ASDEX Upgrade Team, "Frequency control of type-I ELMs by magnetic triggering in ASDEX Upgrade," *Plasma Physics and Controlled Fusion*, vol. 46, pp. L31–L39, 2004.

[8] R. Aymar, "Status of ITER," *Fusion Engineering and Design*, vol. 61–62, pp. 5–12, 2002.

[9] R. Aymar and I. Team, "ITER status, design and material objectives," *Journal of Nuclear Materials*, vol. 307–311, pp. 1–9, 2002.

[10] V. Barabash, "Role and contribution of ITER in research of materials and reactor components," *Journal of Nuclear Materials*, vol. 329-33, pp. 156–160, 2004.

[11] G. Janeschitz and ITER JCT and HTs, "Plasma-wall interaction issues in ITER," *Journal of Nuclear Materials*, vol. 290–293, pp. 1–11, 2001.

[12] Y. Shimomura, "ITER and plasma surface interaction issues in a fusion reactor," *Journal of Nuclear Materials*, vol. 363–365, pp. 467–475, 2007.

[13] "http://www.jet.efda.org." JET.

[14] "http://www.iter.org." ITER organisation.

[15] S. Konishi, S. Nishio, K. Tobita, and the DEMO design team, "DEMO plant design beyond ITER," *Fusion Engineering and Design*, vol. 63-64, pp. 11–17, 2002.

[16] G. Federici, H. Wuerz, G. Janeschitz, and R. Tivey, "Erosion of plasma-facing components in ITER," *Fusion Engineering and Design*, vol. 61-62, pp. 81–94, 2002.

[17] T. Eich, A. Herrmann, G. Pautasso, P. Andrew, N. Asakura, J. Boedo, Y. Corre, M. Fenstermacher, J. Fuchs, W. Fundamenski, G. Federici, E. Gauthier, B. Goncalves, O. Gruber, A. Kirk, A. Leonard, A. Loarte, G. Matthews, J. Neuhauser, R. Pitts, V. Riccardo, and C. Silva, "Power deposition onto plasma facing components in poloidal divertor tokamaks during type-I ELMs and disruptions," *Journal of Nuclear Materials*, vol. 337–339, pp. 669–676, 2005.

[18] Th. Loewenhoff, A. Buerger, J. Linke, G. Pintsuk, and A. Schmidt, "Electron beam simulation of transient heat loads at high cycle numbers," in *Symposium On Fusion Technology 26 (Porto, Portugal)*, 2010.

[19] M. Becoulet, G. Huysmans, P. Thomas, E. Joffrin, F. Rimini, P. Monier-Garbet, A. Grosman, P. Ghendrih, V. Parail, P. Lomas, G. Matthews, H. Wilson, M. Gryaznevich, G. Counsell, A. Loarte, G. Saibene, R. Sartori, A. Leonard, P. Snyder, T. Evans, P. Gohil, R. Moyer, Y. Kamada, N. Oyama, T. Hatae, K. Kamiya, A. Degeling, Y. Martin, J. Lister, J. Rapp, C. Perez, P. Lang, A. Chankin, T. Eich, A. Sips, J. Stober, L. Horton, A. Kallenbach, W. Suttrop, S. Saarelma, S. Cowleyk, J. Loennroth, M. Shimada, A. Polevoi, and G. Federici, "Edge localized modes control: experiment and theory," *Journal of Nuclear Materials*, vol. 337–339, pp. 677–683, 2005.

[20] R. Maingi, S. Sabbagh, C. Bush, E. Fredrickson, J. Menard, D. Stutman, K. Tritz, M. Bell, R. Bell, J. Boedo, D. Gates, D. Johnson, R.Kaita, S. Kaye, H. Kugel, B. LeBlanc, D. Mueller, R. Raman, A. Roquemore, V. Soukhanovskii, and T. Stevenson, "ELMs and the H-mode pedestal in NSTX," *Journal of Nuclear Materials*, vol. 337–339, pp. 727–731, 2005.

[21] D. Hill, "A review of ELMs in divertor tokamaks," *Journal of Nuclear Materials*, vol. 241–243, pp. 182–198, 1997.

[22] A. Loarte, G. Saibene, R. Sartori, M. Becoulet, L. Horton, T. Eich, A. Herrmann, M. Laux, G. Matthews, S. Jachmich, N. Asakura, A. Chankin, A. Leonard, G. Porter, G. Federici, M. Shimada, M. Sugihara, and G. Janeschitz, "ELM energy and particle losses and their extrapolation to burning plasma experiments," *Journal of Nuclear Materials*, vol. 313–316, pp. 388–392, 2003.

[23] A. Leonard, A. Herrmann, K. Itami, J. Lingertat, A. Loarte, T. Osborne, W. Suttrop, and the ITER Divertor Modeling and Database Expert Group and the ITER Divertor Physics Expert Group, "The impact of ELMs on the ITER divertor," *Journal of Materials Processing Technology*, vol. 266-269, pp. 109–117, 1999.

[24] A. Leonard, J. Boedo, M. Fenstermacher, R. Groebner, M. Groth, C. Lasnier, M. Mahdavi, T. Osborne, D. Rudakov, T. Petrie, and J. Watkins, "Transport of ELM energy and particles into the SOL and divertor of DIII-D," *Journal of Materials Processing Technology*, vol. 313-316, pp. 768–776, 2003.

[25] G. Tsotridis, "The melting of tungsten during plasma disruptions," *Journal of Nuclear Materials*, vol. 233–237, pp. 758–762, 1996.

[26] M. Buzio and S. Walker, "Determination of magnetic forces in tokamaks during axisymmetric plasma disruptions," *Fusion Engineering and Design*, vol. 81, pp. 2187–2203, 2006.

[27] P. Knight, G. Castle, A. Morris, A. Caloutsis, and C. Gimblett, "Analysis of Vertical Displacement Events and Halo Currents in COMPASS-D," *Nuclear Fusion*, vol. 40, p. 2000, 1999.

[28] A. Hassanein, "Prediction of material erosion and lifetime during major plasma instabilities in tokamak devices," *Fusion Engineering and Design*, vol. 60, pp. 527–546, 2002.

[29] R. Behrisch, G. Federici, A. Kukushkin, and D. Reiter, "Material erosion at the vessel walls of future fusion devices," *Journal of Nuclear Materials*, vol. 337–339, pp. 677–683, 2003.

[30] R. Matera, G. Federici, and the ITER Joint Central Team, "Design requirements for plasma facing materials in ITER," *Journal of Nuclear Materials*, vol. 233–237, pp. 17–25, 1996.

[31] G. Janeschitz, L. Boccaccini, W. Fietz, W. Goldacker, T. Ihli, R. Meyder, A. Moeslang, and P. Norajitra, "Development of fusion technology for DEMO in Forschungszentrum Karlsruhe," *Fusion Engineering and Design*, vol. 81, pp. 2661–2671, 2006.

[32] G. Federici, P. Andrew, P. Barabaschi, J. Brooks, R. D. A. Geier, A. Herrmann, G. Janeschitz, K. Krieger, A. Kukushkin, A. Loarte, R. Neu, G. Saibene, M. Shimada, G. Strohmayer, and M. Sugihara, "Key ITER plasma edge and plasma-material interaction issues," *Journal of Nuclear Materials*, vol. 313-316, pp. 11–22, 2003.

[33] V. Barabash, G. Federici, J. Linke, and C. Wu, "Material/plasma surface interaction issues following neutron damage," *Journal of Nuclear Materials*, vol. 313-316, pp. 42–51, 2003.

[34] K. Ioki, V. Barabash, J. Cordier, M. Enoeda, G. Federici, B. Kim, I. Mazul, M. Merola, M. Morimoto, M. Nakahira, M. Pick, V. Rozov, M. Shimada, S. Suzuki, M. Ulrickson, Y. Utin, X. Wang, S. Wu, and J. Yu, "ITER vacuum vessel, in-vessel components and plasma facing materials," *Fusion Engineering and Design*, vol. 83, pp. 787–794, 2008.

[35] R. Parker, G. Janeschitz, H. Pacher, D. Post, S. Chiocchio, G. Federici, P. Ladd, Iter Joint Central Team, and Home Teams, "Plasma-wall interactions in ITER," *Journal of Nuclear Materials*, vol. 241–243, pp. 1–26, 1997.

[36] M. Araki, S. Sato, I. Senda, J. Ohmori, and T. Shoji, "Conceptual tokamak design at high neutron fluence," *Fusion Engineering and Design*, vol. 58–55, pp. 887–892, 2001.

[37] M. Akiba, M. Enoeda, D. Tsuru, H. Tanigawa, T. Hirose, K. Mohri, Y. Seki, K. Ezato, S. Suzuki, H. Nishi, and S. Mori, "Development of water-cooled solid breeder test blanket module in JAEA," *Fusion Engineering and Design*, vol. 84, pp. 329–332, 2009.

[38] T. Hirose, M. Enoeda, H. Ogiwara, H. Tanigawa, and M. Akiba, "Structural material properties and dimensional stability of components in first wall components of a breeding blanket module," *Fusion Engineering and Design*, vol. 83, pp. 1176–1180, 2008.

[39] M. Ferrari, L. Giancarli, K. Kleefeldt, C. Nardi, M. Roedig, J. Reimann, and J. Salavy, "Evaluation of divertor conceptual designs for a fusion power plant," *Fusion Engineering and Design*, vol. 56-57, pp. 255–259, 2001.

[40] J. Palmer, M. Siuko, P. Agostini, R. Gottfried, M. Irving, E. Martin, A. Tesini, and M. V. Uffelen, "Recent developments towards ITER 2001 divertor maintenance," *Fusion Engineering and Design*, vol. 75–79, pp. 583–587, 2005.

[41] G. Mazzone, G. Brolatti, E. D'Agata, A. Iorizzo, F. Lucca, A. Marin, M. Merola, L. Petrizzi, A. Pizzuto, M. Roccella, L. Semeraro, and G. Zanotelli, "Design of plasma facing components for the ITER feat divertor," *Fusion Engineering and Design*, vol. 61–62, pp. 153–163, 2002.

[42] R. Tivey, T. Ando, A. Antipenkov, V. Barabash, S. Chiocchio, G. Federici, C. Ibbott, R. Jakeman, G. Janeschitz, R. Raffray, M. Akiba, I. Mazul, H. Pacher, M. Ulrickson, and G. Vieider, "ITER divertor, design issues and research and development," *Fusion Engineering and Design*, vol. 46, pp. 207–220, 1999.

[43] M. Scheerer, H. Bolt, A. Gervash, J. Linke, and I. Smid, "The design of actively cooled plasma-facing components," *Physica Scripta*, vol. 91, pp. 98–103, 2001.

[44] I. Smid, "Material Processing and Testing of Plasma-Interactive Components for Fusion Energy Systems," *Material Science Forum*, vol. 475–479, pp. 1355–1360, 2005.

[45] U. Luconi, M. D. Marco, A. Federici, M. Grattarola, G. Gualco, J. Larrea, M. Merola, C. Ozzano, and G. Pasquale, "Development of the plasma facing components for the dome-liner component of the ITER divertor," *Fusion Engineering and Design*, vol. 75–79, pp. 271–276, 2005.

[46] M. Bisio, V. Branca, M. D. Marco, A. Federici, M. Grattarola, G. Gualco, P. Guarnone, U. Luconi, M. Merola, C. Ozzano, G. Pasquale, P. Poggi, S. Rizzo, and F. Varone, "Manufacturing and testing in reactor relevant conditions of brazed plasma facing components of the ITER divertor," *Fusion Engineering and Design*, vol. 75–79, pp. 277–283, 2005.

[47] B. Schedler, T. Huber, E. Eidenberger, C. Scheu, R. Pippan, and H. Clemens, "Methods to determine the joint strength of C/C to copper joints," *Fusion Engineering and Design*, vol. 82, pp. 1786–1792, 2007.

[48] P. Appendino, M. Ferraris, V. Casalegno, M. Salvo, M. Merola, and M. Grattarola, "Direct joining of CFC to copper," *Journal of Nuclear Materials*, vol. 329–333, pp. 1563–1566, 2004.

[49] M. Merola, M. Akiba, V. Barabash, and I. Mazul, "Overview on fabrication and joining of plasma facing and high heat flux materials for ITER," *Journal of Nuclear Materials*, vol. 56–57, pp. 173–178, 2002.

[50] M. Merola, G. Vieider, M. Bet, I. B. Vastra, L. Briottet, P. Chappuis, K. Cheyne, G. Dell'Orco, D. Duglué, R. Duwe, S. Erskine, F. Escourbiac, M. Fèbvre, M. Grattarola, F. Moreschi, A. Orsini, R. Pamato, L. Petrizzi, L. Ploechl, B. Riccardi, E. Rigal, M. Roedig, J. Salavy, B. Schedler, J. Schlosser, S. Taehtinen, R. Vesprini, E. Visca, and C. H. Wu, "European achievements for ITER high heat flux components," *Fusion Engineering and Design*, vol. 307–311, pp. 1524–1532, 2001.

[51] M. Merola and G. Vieider, "On the use of flat tile armour in high heat flux components," *Journal of Nuclear Materials*, vol. 258–263, pp. 672–676, 1998.

[52] V. Barabash, M. Akiba, A. Cardella, I. Mazul, B. Odegard, L. Ploechl, R. Tivey, and G. Vieider, "Armor and heat sink materials joining technologies development for ITER plasma facing components," *Journal of Nuclear Materials*, vol. 283-287, pp. 1248–1252, 2000.

[53] G. Vieider, M. Merola, F. Anselmi, J. Bonal, P. Chappuis, G. Dell'Orco, D. Duglué, R. Duwe, S. Erskine, F. Escourbiac, M. Fèbvre, L. Giancarli, M. Grattarola, G. LeMarois, H. Pacher, A. Pizzuto, L. Plöchl, B. Riccardi, M. Roedig, J. Schlosser, A. Salito, B. Schedler, and C. Wu, "European development of prototypes for ITER high heat flux components," *Fusion Engineering and Design*, vol. 49–50, pp. 135–143, 2009.

[54] G. Kalinin, V. Barabash, A. Cardella, J. Dietz, K. Ioki, R. Matera, R. Santoro, R. Tivey, and the ITER Home Teams, "Assessment and selection of materials for ITER in-vessel components," *Journal of Nuclear Materials*, vol. 283-287, pp. 10–19, 2000.

[55] M. Merola, W. Daenner, M. Pick, and the EU ITER Participating Team, "EU R&D on divertor components," *Fusion Engineering and Design*, vol. 75–79, pp. 325–331, 2005.

[56] M. Roedig, R. Duwe, W. Kuehnlein, J. Linke, M. Scheerer, I. Smid, and B. Wiechers, "Testing of actively cooled high heat flux mock-ups," *Journal of Nuclear Materials*, vol. 258–263, pp. 967–971, 1998.

[57] M. Roedig, M. Akiba, P. Chappuis, R. Duwe, M. Febvre, A. Gervash, J. Linke, N. Litounovsky, S. Suzuki, B. Wiechers, and D. L. Youchison, "Comparison of electron beam test facilities for testing of high heat flux components," *Fusion Engineering and Design*, vol. 51–52, pp. 715–722, 2000.

[58] J. Linke, "High Heat Flux Performance Of Plasma Facing Materials And Components Under Service Conditions In Future Fusion Reactors," *Transactions Of Fusion Science And Technology*, vol. 49, pp. 455–464, 2006.

[59] H. Bolt, V. Barabash, W. Krauss, J. Linke, R. Neu, S. Suzuki, N. Yoshida, and ASDEX Upgrade Team, "Materials for the plasma-facing components of fusion reactors," *Journal of Nuclear Materials*, vol. 329–333, pp. 66–73, 2004.

[60] A. Raffray, R. Nygren, D. Whyte, S. Abdel-Khalik, R. Doerner, F. Escourbiac, T. Evans, R. Goldston, D. Hoelzer, S. Konishi, P. Lorenzetto, M. Merola, R. Neu, P. Norajitra, R. Pitts, M. Rieth, M. Roedig, T. Rognlien, S. Suzuki, M. Tillack, and C. Wong, "High heat flux components - Readiness to proceed from near term fusion systems to power plants," *Fusion Engineering and Design*, vol. 85, pp. 93–108, 2010.

[61] J. Linke, T. Hirai, M. Roedig, and L. Singheiser, "Performance of plasma-facing materials under intense thermal loads in tokamaks and stellarators," *Fusion Science and Technology*, vol. 46, pp. 142–151, 2004.

[62] V. Barabash, M. Akiba, I. Mazul, M. Ulrickson, and G. Vieider, "Selection, development and characterisation of plasma facing materials for ITER," *Journal of Nuclear Materials*, vol. 233–237, pp. 718–723, 1996.

[63] J. Linke, P. Lorenzetto, P. Majerus, M. Merola, D. Pitzer, and M. Roedig, "EU Development of High Heat Flux Components," vol. 47, pp. 678–685, 2005.

[64] A. Raffray, G. Federici, V. Barabash, H. Pacher, H. Bartels, A. Cardella, R. Jakeman, K. Ioki, G. Janeschitz, R. Parker, R. Tivey, and C. Wu, "Beryllium application in ITER plasma facing components," *Fusion Engineering and Design*, vol. 37, pp. 261–286, 1997.

[65] M. Shimada, A. Costley, G. Federici, K. Ioki, A. Kukushkin, V. Mukhovatov, A. Polevoi, and M. Sugihara, "Overview of goals and performance of ITER and strategy for plasma-wall interaction investigation," *Journal of Nuclear Materials*, vol. 337–339, pp. 808–815, 2005.

[66] V. Philipps, J. Roth, and A. Loarte, "Key issues in plasma-wall interaction for ITER: a European approach," *Plasma Physics and Controlled Fusion*, vol. 45, pp. A17–A30, 2003.

[67] G. Federici, D. Holland, G. Janeschitz, and C. Wu, "The influence of key operation parameters and material properties on the quantification of tritium inventory and permeation in the plasma facing components of ITER," *Journal of Nuclear Materials*, vol. 241-243, pp. 260–267, 1997.

[68] J. Compan, T. Hirai, G. Pintsuk, and J. Linke, "Microstructural and thermomechanical characterization of carbon/carbon composites," *Journal of Nuclear Materials*, vol. 386–388, pp. 797–800, 2009.

[69] T. Hirai, J. Compan, K. Niwase, and J. Linke, "Laser raman microprobe analysis of graphite exposed to edge plasma in the TEXTOR tokamak," *Journal of Nuclear Materials*, vol. 373, pp. 119–122, 2008.

[70] G. Pintsuk, J. Compan, T. Koppitz, J. Linke, A. Peacock, D. Pitzer, M. Roedig, and S. Wikman, "Mechanical and thermo-physical characterization of three-directional carbon fiber composites for W-7X and ITER," *Fusion Engineering and Design*, vol. 84, pp. 1525–1530, 2009.

[71] K. Sato, E. Ishitsuka, M. Uda, H. Kawamura, S. Suzuki, M. Taniguchi, K. Ezato, and M. Akiba, "Erosion characteristics of neutron-irradiated carbon-based materials under simulated disruption heat loads," *Journal of Nuclear Materials*, vol. 283–287, pp. 1157–1160, 2000.

[72] H. Wuerz, B. Bazylev, I. Landman, S. Pestchanyi, and V. Safronov, "Macroscopic erosion of divertor and first wall armour in future tokamaks," *Journal of Nuclear Materials*, vol. 307–311, pp. 60–68, 2002.

[73] J. Davis and A. Haasz, "Impurity release from low-Z materials under light particle bombardment," *Journal of Nuclear Materials*, vol. 241–243, pp. 37–51, 1997.

[74] M. Roedig, E. Ishitsuka, A. Gervash, H. Kawamura, J. Linke, N. Litunovski, and M. Merola, "High heat flux performance of neutron irradiated plasma facing components," *Journal of Nuclear Materials*, vol. 307–311, pp. 53–59, 2002.

[75] C. Wu, C. Alessandrini, P. Bonal, H. Grote, R. Moormann, M. Roedig, J. Roth, H. Werle, and G. Vieider, "Overview of EU CFCs development for plasma facing materials," *Journal of Nuclear Materials*, vol. 258–263, pp. 833–838, 1998.

[76] C. Wu, C. Alessandrini, J. Bonal, J. Davis, A. Haasz, W. Jacob, A. Kallenbach, J. Keinonen, P. Kornejew, R. Moormann, V. Philipps, J. Roth, F. Scaffidi-Argentina, and H. Wuerz, "Progress of the European R&D on plasma-wall interactions, neutron effects and tritium removal in ITER plasma facing materials," *Fusion Engineering and Design*, vol. 56–57, pp. 179–187, 2001.

[77] T. Hirai, H. Maier, M. Rubel, P. Mertens, R. Neu, E. Gauthier, J. Likonen, C. Lungu, G. Maddaluno, G. Matthews, R. Mitteau, O. Neubauer, G. Piazza, V. Philipps, B. Riccardi, C. Ruset, I. Uytdenhouwen, and JET EFDA Contributors, "R&D on full tungsten divertor and beryllium wall for JET ITER-like wall project," *Fusion Engineering and Design*, vol. 82, pp. 1839–1845, 2007.

[78] T. Tanabe, N. Noda, and H. Nakamura, "Review of High Z Materials for PSI Applications," *Journal of Nuclear Materials*, vol. 196–198, pp. 11–27, 1992.

[79] I. Smid, M. Akiba, G. Vieider, and L. Ploech, "Development of tungsten armor and bonding to copper for plasma-interactive components," *Journal of Nuclear Materials*, vol. 258–263, pp. 160–172, 1998.

[80] G. Federici, A. Zhitlukhin, N. Arkhipov, R. Giniyatulin, N. Klimov, I. Landman, V. Podkovyrov, V. Safronov, N. N. A. LoarteK. Tokunagab, N. Yoshidab, Z. Xu, and M. Merola, "Effects of ELMs and disruptions on ITER divertor armour materials," *Journal of Nuclear Materials*, vol. 337-339, pp. 684–690, 2005.

[81] "Materials Assessment Report, ITER Doc. G 74 MA 10 01-07-11 W 0.2."

[82] K. Krieger, H. Maier, R. Neu, and ASDEX Upgrade Team, "Conclusions about the use of tungsten in the divertor of ASDEX upgrade," *Journal of Nuclear Materials*, vol. 266-269, pp. 207–216, 1999.

[83] R. Neu, V. Rohde, A. Geier, K. Krieger, H. Maier, D. Bolshukhin, A. Kallenbach, R. Pugno, K. Schmidtmann, M. Zarrabian, and ASDEX Upgrade Team, "Plasma operation with tungsten tiles at the central column of ASDEX Upgrade," *Journal of Nuclear Materials*, vol. 290–293, pp. 206–210, 2001.

[84] R. Neu, R. Dux, A. Geier, O. Gruber, A. Kallenbach, K. Krieger, H. Maier, R. Pugno, V. Rohde, S. Schweizer, and ASDEX Upgrade Team, "Tungsten as plasma-facing material in ASDEX Upgrade," *Fusion Engineering and Design*, vol. 65, pp. 367–374, 2003.

[85] R. Neu, R. Dux, A. Geier, H. Greuner, K. Krieger, H. Maier, R. Pugno, V. Rohde, S. Yoon, and ASDEX Upgrade Team

[86] H. Maier, J. Luthin, M. Balden, J. Linke, F. Koch, and H. Bolt, "Properties of tungsten coatings deposited onto fine grain graphite by different methods," *Surface and Coatings Technology*, vol. 142–144, pp. 733–737, 2001.

[87] K. Tokunaga, N. Yoshida, Y. Kubota, N. Noda, Y. Imamura, T. Oku, A. Kurumada, T. Sogabe, T. Kato, and L. Ploechl, "High heat flux test of actively cooled tungsten-coated carbon divertor mock-ups," *Fusion Engineering and Design*, vol. 49–50, pp. 371–376, 2000.

[88] S. Deschka, C. Garcia-Rosales, W. Hohenauer, R. Duwe, E. Gauthier, J. Linke, M. Lochter, W. Malléner, L. Ploechl, P. Roedhammer, and A. Salito, "Manufacturing and high heat flux loading of tungsten coatings on fine grain graphite for the ASDEX-upgrade divertor," *Journal of Nuclear Materials*, vol. 233–237, pp. 645–649, 1996.

[89] J. Boscary, S. Suzuki, K. Nakamura, T. Suzuki, and M. Akiba, "Thermal fatigue tests on CVD-W/Cu divertor mock-ups," *Fusion Engineering and Design*, vol. 537–542, pp. 39–40, 1998.

[90] K. Nakamura, S. Suzuki, T. Tanabe, M. Dairaku, K. Yokoyama, and M. Akiba, "Disruption erosions of various kinds of tungsten," *Fusion Engineering and Design*, vol. 39–40, pp. 295–301, 1998.

[91] Y. Yahiro, M. Mitsuhara, K. Tokunakga, N. Yoshida, T. Hirai, K. Ezato, S. Suzuki, M. Akiba, and H. Nakashima, "Characterization of thick plasma spray tungsten coating on ferritic/martensitic steel F82H for high heat flux armor," *Journal of Nuclear Materials*, vol. 386–388, pp. 784–788, 2009.

[92] T. Hino and M. Akiba, "Japanese developments of fusion reactor plasma facing components," *Fusion Engineering and Design*, vol. 49–50, pp. 97–105, 2000.

[93] H. Maier, S. Koetterl, K. Krieger, R. Neu, M. Balden, and ASDEX Upgrade-Team, "Performance of tungsten coatings as plasma facing components used

in ASDEX Upgrade," *Journal of Nuclear Materials*, vol. 258–263, pp. 921–926, 1998.

[94] R. Mitteau, J. Missiaen, P. Brustolin, O. Ozer, A. Durocher, C. Ruset, C. Lungu, X. Courtois, C. Dominicy, H. Maier, C. Grisolia, G. Piazza, and P. Chappuis, "Recent developments toward the use of tungsten as armour material in plasma facing components," *Fusion Engineering and Design*, vol. 82, pp. 1700–1705, 2007.

[95] J. Linke, M. Akiba, H. Bolt, J. van der Laan, H. Nickel, E. van Osche, S. Suzuki, and E. Wallura, "Simulation of disruptions on coatings and bulk materials," *Journal of Nuclear Materials*, vol. 196–198, pp. 607–611, 1992.

[96] X. Liu, L. Yang, S. Tamura, K. Tokunaga, N. Yoshida, N. Noda, and Z. Xu, "Thermal response of plasma sprayed tungsten coating to high heat flux," *Fusion Engineering and Design*, vol. 70, pp. 341–349, 2004.

[97] T. Hirai, A. Kreter, J. Linke, J. Malzbender, T. Ohgo, V. Philipps, G. Pintsuk, A. Pospieszczyk, Y. Sakawa, G. Sergienko, T. Tanabe, Y. Ueda, and M. Wada, "Critical heat flux loading experiments on CVD-W coating in the TEXTOR tokamak," *Fusion Engineering and Design*, vol. 81, pp. 175–180, 2006.

[98] T. Tanabe, M. Wada, T. Ohgo, V. Philipps, M. Rubel, A. Huber, J. v. Seggern, K. Ohya, A. Pospieszczyk, B. Schweer, and T. team, "Application of tungsten for plasma limiters in TEXTOR," *Journal of Nuclear Materials*, vol. 283–287, pp. 1128–1133, 2000.

[99] X. Liu, S. Tamura, K. Tokunaga, N. Yoshida, N. Noda, L. Yanga, and Z. Xu, "High heat flux properties of pure tungsten and plasma sprayed tungsten coatings," *Journal of Nuclear Materials*, vol. 329–333, pp. 687–691, 2004.

[100] F. Elio, K. Ioki, P. Barabaschi, L. Bruno, A. Cardella, M. Hechler, T. Kodama, A. Lodato, D. Loesser, D. Lousteau, N. Miki, K. Mohri, R. Parker, R. Raffray, D. Williamson, M. Yamada, W. Daenner, R. Mattas, Y. Strebkov, and H. Takatsu, "Engineering design of the ITER blanket and relevant research and development results," *Fusion Engineering and Design*, vol. 46, pp. 159–175, 1999.

[101] G. Federici, C. Skinner, J. Brooks, J. Coad, C. Grisolia, A. Haasz, A. Hassanein, V. Philipps, C. Pitcher, J. Roth, W. Wampler, and D. Whyte, "Plasma-material interactions in current tokamaks and their implications for next step fusion reactors," *Nuclear Fusion*, vol. 41, pp. 1967–2137, 2001.

[102] C. Baxi and C. Wong, "Review of helium cooling for fusion reactor applications," *Fusion Engineering and Design*, vol. 51-52, pp. 319–324, 2000.

[103] P. Sardain, D. Maisonnier, L. D. Pace, L. Giancarli, A. L. Puma, P. Norajitra, A. Orden, E. Arenaza, D. Ward, and the PPCS team, "The European power plant conceptual study: Helium-cooled lithium-lead reactor concept," *Fusion Engineering and Design*, vol. 81, pp. 2673–2678, 2006.

[104] L. Boccaccini, L. Giancarli, G. Janeschitz, S. Hermsmeyer, Y. Poitevin, A. Cardella, and E. Diegele, "Materials and design of the European DEMO blankets," *Journal of Nuclear Materials*, vol. 329–333, pp. 148–155, 2004.

[105] L. Giancarli, M. Ferrari, M. Fuetterer, and S. Malang, "Candidate blanket concepts for a European fusion power plant study," *Fusion Engineering and Design*, vol. 49–50, pp. 445–456, 2000.

[106] O. Ogorodnikova, X. Raepsaet, and M. Fuetterer, "Tritium permeation through the first wall of the EU-HCPB blanket," *Fusion Engineering and Design*, vol. 49–50, pp. 921–926, 2000.

[107] P. Norajitra, R. Giniyatulin, T. Ihli, G. Janeschitz, W. Krauss, R. Kruessmann, V. Kuznetsov, I. Mazul, V. Widak, I. Ovchinnikov, R. Ruprecht, and B. Zeep, "He-cooled divertor development for DEMO," *Fusion Engineering and Design*, vol. 82, pp. 2740–2744, 2007.

[108] G. Ritz, T. Hirai, J. Linke, P. Norajitra, R. Giniyatulin, and L. Singheiser, "Post-examination of helium-cooled tungsten components exposed to DEMO specific cyclic thermal loads," *Fusion Engineering and Design*, vol. 84, pp. 1623–1627, 2009.

[109] P. Norajitra, R. Giniyatulin, T. Hirai, W. Krauss, V. Kuznetsov, I. Mazul, I. Ovchinnikov, J. Reiser, G. Ritz, H.-J. Ritzhaupt-Kleissl, and V. Widak, "Current status of He-cooled divertor development for DEMO," *Fusion Engineering and Design*, vol. 84, pp. 1429–1433, 2009.

[110] T. Ihli, S. Hermsmeyer, C. Koehly, and P. Norajitra, "Integration of an advanced He-cooled divertor in a DEMO-relevant tokamak geometry," *Fusion Engineering and Design*, vol. 81, pp. 121–126, 2006.

[111] I. Ovchinnikov, R. Giniyatulin, T. Ihli, G. Janeschitz, A. Komarov, R. Kruessmann, V. Kuznetsov, S. Mikhailov, P. Norajitra, and V. Smirnov, "Experimental study of DEMO helium cooled divertor target mock-ups to estimate their thermal and pumping efficiencies," *Fusion Engineering and Design*, vol. 73, pp. 181–186, 2005.

[112] P. Norajitra, A. Gervash, R. Giniyatulin, T. Hirai, G. Janeschitz, W. Krauss, V. Kuznetsov, A. Makhankov, I. Mazul, I. Ovchinnikov, J. Reiser, and V. Widak, "Helium-cooled divertor for DEMO: Manufacture and high heat flux tests of

tungsten-based mock-ups," *Journal of Nuclear Materials*, vol. 386–388, pp. 813–816, 2009.

[113] P. Norajitra, R. Giniyatulin, N. Holstein, T. Ihli, W. Krauss, R. Kruessmann, V. Kuznetsov, I. Mazul, I. Ovchinnikov, and B. Zeep, "Status of He-cooled divertor development for DEMO," *Fusion Engineering and Design*, vol. 75–79, pp. 307–311, 2005.

[114] V. Widak and P. Norajitra, "Optimization of He-cooled divertor cooling fingers using a CAD-FEM method," *Fusion Engineering and Design*, vol. 84, pp. 1973–1978, 2009.

[115] V. Widak, P. Norajitra, L. Boccaccini, and G. Janeschitz, "Assessment of the He-cooled Test Divertor Module for ITER," *Fusion Engineering and Design*, vol. 83, pp. 1131–1136, 2008.

[116] P. Norajitra, S. Antusch, H.-J. Ritzhaupt-Kleissl, L. Spatafora, V. Widak, R. Giniyatulin, V. Kuznetsov, I. Mazul, and I. Ovchinnikov, "He-Cooled Divertor for DEMO: Technological Studies and Experimental Verification of the Design," 2009.

[117] P. Norajitra, A. Gervash, R. Giniyatulin, T. Ihli, W. Krauss, R. Kruessmann, V. Kuznetsov, A. Makhankov, I. Mazul, and I. Ovchinnikov, "He-cooled divertor for DEMO: Experimental verification of the conceptual modular design," *Fusion Engineering and Design*, vol. 81, pp. 341–346, 2006.

[118] J. Reiser, P. Norajitra, and R. Ruprecht, "Numerical investigation of a brazed joint between W-1%La_2O_3 and ODS EUROFER components," *Fusion Engineering and Design*, vol. 83, pp. 1126–1130, 2008.

[119] P. Norajitra, L. Boccaccini, A. Gervash, R. Giniyatulin, N. Holstein, T. Ihli, G. Janeschitz, W. Krauss, R. Kruessmann, V. Kuznetsov, A. Makhankov, I. Mazul, A. Moeslang, I. Ovchinnikov, M. Rieth, and B. Zeep, "Development of a helium-cooled divertor: Material choice and technological studies," *Journal of Nuclear Materials*, vol. 367–370, pp. 1416–1421, 2007.

[120] P. Norajitra, S. Antusch, R. Giniyatulin, I. Mazul, G. Ritz, H.-J. Ritzhaupt-Kleissl, and L. Spatafora, "Current State-Of-The-Art Manufacturing Technology for He-Cooled Divertor Finger," *Fourteenth International Conference on Fusion Reactor Materials*, 2009.

[121] M. Rieth, J. Boutard, S. Dudarev, T. Ahlgren, S. Antusch, N. Baluc, M.-F. Barthe, C. Becquart, L. Ciupinski, J. Correia, C. Domain, J. Fikar, E. Fortuna, C.-C. Fu, E. Gaganidze, T. Galán, C. García-Rosales, B. Gludovatz, H. Greuner, K. Heinola, N. Holstein, N. Juslin, F. Koch, W. Krauss, K. Kurzydlowski, J. Linke, C. Linsmeier, N. Luzginova, H. Maier, M. Martínez, J. Missiaen, M. Muhammed, A. Muñoz, M. Muzyk, K. Nordlund, D. Nguyen-Manh,

P. Norajitra, J. Opschoor, G. Pintsuk, R. Pippan, G. Ritz, L. Romane, D. Rupp, R. Schaeublin, J. Schlosser, I. Uytdenhouwen, J. van der Laan, L. Veleva, L. Ventelon, S. Wahlberg, F. Willaime, S. Wurster, and M. Yar, "Review on the EFDA Programme on Tungsten Materials Technology and Science," in *International Conference on Fusion Reactor Materials 14 (Sapporo, Japan)*, 2009.

[122] J. Wang and B. Ravani, "Computer aided contouring operation for traveling wire electric discharge machining (EDM)," *Computer-Aided Design*, vol. 35, pp. 925–934, 2003.

[123] R. Giniyatulin, A. Alekseev, A. Gervash, A. Kokoulin, A.Komarov, V. Kuznetsov, A. Labusov, A. Makhankov, I. Mazul, I. Ovchinnikov, V. Smirnov, and N. Yablokov, "Development of He-cooled target module mock-ups for DEMO fusion reactor divertor," tech. rep., D.V. Efremov Scientific Research Institute of Electrophysical Apparatus (NIIEFA), 2007.

[124] A. Gervash, R. Giniyatulin, T. Ihli, W. Krauss, A. Makhankov, I. Mazul, P. Norajitra, and N. Yablokov, "Fabrication of a He-cooled divertor module for DEMO reactor," *Journal of Nuclear Materials*, vol. 367–370, pp. 1472–1475, 2007.

[125] A. Gervash, R. Giniyatulin, V. Komarov, I. Mazul, N. Litunovsky, A. Ganenko, A. Vainerman, V. Fedotov, D. Davydov, and R. Zalavutdinov, "Comparative thermal cyclic testing and strength investigation of different Be/Cu joints," *Fusion Engineering and Design*, vol. 39–40, pp. 543–549, 1998.

[126] M. Roedig, I. Bobin-Vastra, S. Cox, F. Escourbiac, A. Gervash, A. Kapoustina, W. Kuehnlein, V. Kuznetsov, M. Merola, R. Nygren, and D. Youchison, "Testing of actively cooled mock-ups in several high heat flux facilities-An International Round Robin Test," *Fusion Engineering and Design*, vol. 75–79, pp. 303–306, 2005.

[127] H. Lee and T. Tai, "Relationship between EDM parameters and surface crack formation," *Journal of Materials Processing Technology*, vol. 142, pp. 676–683, 2003.

[128] I. Uytdenhouwen, M. Decreton, T. Hirai, J. Linke, G. Pintsuk, and G. V. Oost, "Influence of recrystallization on thermal shock resistance of various tungten grades," *Journal of Nuclear Materials*, vol. 363–365, pp. 1099–1103, 2007.

[129] J. Davis and G. Kalinin, "Material properties and design requirements for copper alloys used in ITER," *Journal of Nuclear Materials*, vol. 258–263, pp. 323–328, 1998.

[130] "http://www.plansee.com." Plansee.

[131] Th. Loewenhoff, T. Hirai, S. Keusemann, J. Linke, G. Pintsuk, and A. Schmidt, "Experimental simulation of Edge Localised Modes using focused electron beams - features of a circular load pattern," 2010.

[132] T. Hirai and G. Pintsuk, "Thermo-mechanical calculations on operation temperature limits of tungsten as plasma facing material," *Fusion Engineering and Design*, vol. 82, pp. 389–393, 2007.

[133] T. Hirai, G. Pintsuk, J. Linke, and M. Batilliot, "Cracking failure study of ITER-reference tungsten grade under single pulse thermal shock loads at elevated temperatures," *Journal of Nuclear Materials*, vol. 390–391, pp. 751–754, 2009.

[134] J. Linke, S. Amouroux, E. Berthe, Y. Koza, W. Kuehnlein, and M. Roedig, "Brittle destruction of carbon-based materials in transient heat load tests," *Fusion Engineering and Design*, vol. 66–68, pp. 395–399, 2003.

[135] M. Roedig, W. Kuehnlein, J. Linke, D. Pitzer, M. Merola, E. Rigal, B. Schedler, and E. Visca, "Post irradiation testing of samples from the irradiation experiments PARIDE 3 and PARIDE 4," *Journal of Nuclear Materials*, vol. 329–333, pp. 766–700, 2004.

[136] T. Hirai, J. Linke, W. Kuehnlein, G. Sergienko, and S. Brezinsek, "Light emission from carbon-based materials under ITER relevant thermal shock loads," *Journal of Nuclear Materials*, vol. 321, pp. 110–114, 2003.

[137] G. Pintsuk, W. Kuehnlein, J. Linke, and M. Roedig, "Investigation of tungsten and beryllium behaviour under short transient events," *Fusion Engineering and Design*, vol. 82, pp. 1720–1729, 2007.

[138] Y. Koza, E. Berthe, E. Lehmann, J. Linke, M. Roedig, E. Wessel, and L. Singheiser, "Formation of dust particles under the influence of intense thermal loads," *Journal of Nuclear Materials*, vol. 329-333, pp. 706–710, 2004.

[139] T. Hirai, J. Linke, M. Rubel, J. Coad, J. Likonen, C. Lungu, G. Matthews, V. Philipps, E. Wessel, and J. contributors, "Thermal load testing of erosion-monitoring beryllium marker tile for the ITER-Like Wall Project at JET," *Fusion Engineering and Design*, vol. 83, pp. 1072–1076, 2008.

[140] J. Linke, F. Escourbiac, I. Mazul, R. Nygren, M. Roedig, J. Schlosser, and S. Suzuki, "High heat flux testing of plasma facing materials and components - Status and perspectives for ITER related activities," *Journal of Nuclear Materials*, vol. 367–370, pp. 1422–1431, 2007.

[141] G. Pintsuk, Z. Oksiuta, J. Linke, and N. Baluc, "High heat flux testing of 12-14Cr ODS ferritic steels," *Journal of Nuclear Materials*, vol. 396, pp. 20–25, 2010.

[142] T. Hirai, N. Bekris, J. Coad, C. Grisolia, J. Linke, H. Maier, G. Matthews, V. Philipps, and E. Wessel, "Failure modes of vacuum plasma spray tungsten coating created on carbon fibre composites under thermal loads," *Journal of Nuclear Materials*, vol. 392, pp. 40–44, 2009.

[143] M. Wirtz, J. Linke, and G. Pintsuk, "Thermal resistivity of tungsten grades under fusion relevant conditions," in *Jahrestagung Kerntechnik 2010 (Berlin, Germany)*, 2010.

[144] B. Zeep, P. Norajitra, V. Piotter, J. Boehm, R. Ruprecht, and J. Hausselt, "Net shaping of tungsten components by micro powder injection moulding," *Fusion Engineering and Design*, vol. 82, pp. 2660–2665, 2007.

[145] V. Piotter, B. Zeep, P. Norajitra, R. Ruprecht, A. v. Weth, and J. Hausselt, "Development of a powder metallurgy process for tungsten components," *Fusion Engineering and Design*, vol. 83, pp. 1517–1520, 2008.

[146] "http://www.sinotech.com." Sinotech.

[147] P. Norajitra, J. Reiser, H.-J. Ritzhaupt-Kleissl, S. Dichiser, J. Konrad, and G. Ritz, "Development of a He-cooled divertor: Status of the fabrication technology," 2008.

[148] J. Reiser, P. Norajitra, V. Widak, and W. Krauss, "He-Cooled Divertor For DEMO: Fabrication Technology For Tungsten Cooling Fingers," pp. 680–684, 2008.

[149] W. Krauss, N. Holstein, J. Konys, and I. Mazul, "Investigation of the impact of fabrication methods on the microstructure features of W-components of a He-cooled divertor," *Fusion Engineering and Design*, vol. 81, pp. 256–264, 2006.

[150] W. Krauss, N. Holstein, and J. Konys, "Strategies in electro-chemical machining of tungsten for divertor application," *Fusion Engineering and Design*, vol. 82, pp. 1799–1805, 2007.

[151] W. Krauss, N. Holstein, and J. Konys, "Development and fabrication aspects regarding tungsten components for a He-cooled divertor," *Fusion Engineering and Design*, vol. 75–79, pp. 775–778, 2005.

[152] N. Holstein, W. Krauss, and J. Konys, "Structuring of tungsten by pulsed ECM processes for He-cooled divertor application," *Fusion Engineering and Design*, vol. 83, pp. 1512–1516, 2008.

Acknowledgements

I would like to thank Univ.-Prof. Dr.-Ing. L. Singheiser for giving me the opportunity to work in the Institut für Energieforschung (IEF-2) of Forschungszentrum Jülich.

To Dr. J. Linke for welcoming me in his group. For his optimism, sound suggestions and contributions, which made the work stimulating and productive.
To Dr. T. Hirai for his positive impact on my scientific work, practical advices and clever ideas, in general his ability to constantly improve all aspects of the work to produce masterpieces. To Dr. G. Pintsuk for his logical approach of the scientific work, accurate and constructive criticisms to reach high effectiveness during the interpretation of experimental results.
To Mrs. G. Knauf and Mr. G. Böling for their support in the preparation of the experimental setup and the processing of post-experimental data. To Mr. Th. Loewenhoff and Mr. M. Wirtz for their help in solving technical problems and for providing a stimulating and enjoyable environment in which to learn.
To Dr. E. Wessel, Mr. V. Gutzeit, Mr. J. Bartsch for their help, time and knowledge on sample preparation and surface inspection, which contributed to optimise the metallography and the material characterisation aspects.
To Mr. T. Koppitz for fruitful discussions on material joining techniques and his technical advices.

To Dr. R. Chaouadi for his encouragements.

To Dr. P. Norajitra and J. Reiser for their trust and support in the collaboration for the helium-cooled divertor project and the machining qualification program.

To Dr. R. Giniyatulin and Dr. A. Makhankov for providing with the tungsten materials and sharing useful information on high heat flux testing.

To Dr. M. Missirlian for the coordination of the European Training Network for Plasma-Facing Materials.

Finally, to my family who gave me precious and constant support as well as motivation.

1. **Einsatz von multispektralen Satellitenbilddaten in der Wasserhaushalts- und Stoffstrommodellierung – dargestellt am Beispiel des Rureinzugsgebietes**
   von C. Montzka (2008), XX, 238 Seiten
   ISBN: 978-3-89336-508-1

2. **Ozone Production in the Atmosphere Simulation Chamber SAPHIR**
   by C. A. Richter (2008), XIV, 147 pages
   ISBN: 978-3-89336-513-5

3. **Entwicklung neuer Schutz- und Kontaktierungsschichten für Hochtemperatur-Brennstoffzellen**
   von T. Kiefer (2008), 138 Seiten
   ISBN: 978-3-89336-514-2

4. **Optimierung der Reflektivität keramischer Wärmedämmschichten aus Yttrium-teilstabilisiertem Zirkoniumdioxid für den Einsatz auf metallischen Komponenten in Gasturbinen**
   von A. Stuke (2008), X, 201 Seiten
   ISBN: 978-3-89336-515-9

5. **Lichtstreuende Oberflächen, Schichten und Schichtsysteme zur Verbesserung der Lichteinkopplung in Silizium-Dünnschichtsolarzellen**
   von M. Berginski (2008), XV, 171 Seiten
   ISBN: 978-3-89336-516-6

6. **Politikszenarien für den Klimaschutz IV – Szenarien bis 2030**
   hrsg.von P. Markewitz, F. Chr. Matthes (2008), 376 Seiten
   ISBN 978-3-89336-518-0

7. **Untersuchungen zum Verschmutzungsverhalten rheinischer Braunkohlen in Kohledampferzeugern**
   von A. Schlüter (2008), 164 Seiten
   ISBN 978-3-89336-524-1

8. **Inorganic Microporous Membranes for Gas Separation in Fossil Fuel Power Plants**
   by G. van der Donk (2008), VI, 120 pages
   ISBN: 978-3-89336-525-8

9. **Sinterung von Zirkoniumdioxid-Elektrolyten im Mehrlagenverbund der oxidkeramischen Brennstoffzelle (SOFC)**
   von R. Mücke (2008), VI, 165 Seiten
   ISBN: 978-3-89336-529-6

10. **Safety Considerations on Liquid Hydrogen**
    by K. Verfondern (2008), VIII, 167 pages
    ISBN: 978-3-89336-530-2

11. **Kerosinreformierung für Luftfahrtanwendungen**
von R. C. Samsun (2008), VII, 218 Seiten
ISBN: 978-3-89336-531-9

12. **Der 4. Deutsche Wasserstoff Congress 2008 – Tagungsband**
hrsg. von D. Stolten, B. Emonts, Th. Grube (2008), 269 Seiten
ISBN: 978-3-89336-533-3

13. **Organic matter in Late Devonian sediments as an indicator for environmental changes**
by M. Kloppisch (2008), XII, 188 pages
ISBN: 978-3-89336-534-0

14. **Entschwefelung von Mitteldestillaten für die Anwendung in mobilen Brennstoffzellen-Systemen**
von J. Latz (2008), XII, 215 Seiten
ISBN: 978-3-89336-535-7

15. **RED-IMPACT**
Impact of Partitioning, Transmutation and Waste Reduction Technologies on the Final Nuclear Waste Disposal
SYNTHESIS REPORT
ed. by W. von Lensa, R. Nabbi, M. Rossbach (2008), 178 pages
ISBN 978-3-89336-538-8

16. **Ferritic Steel Interconnectors and their Interactions with Ni Base Anodes in Solid Oxide Fuel Cells (SOFC)**
by J. H. Froitzheim (2008), 169 pages
ISBN: 978-3-89336-540-1

17. **Integrated Modelling of Nutrients in Selected River Basins of Turkey**
Results of a bilateral German-Turkish Research Project
project coord. M. Karpuzcu, F. Wendland (2008), XVI, 183 pages
ISBN: 978-3-89336-541-8

18. **Isotopengeochemische Studien zur klimatischen Ausprägung der Jüngeren Dryas in terrestrischen Archiven Eurasiens**
von J. Parplies (2008), XI, 155 Seiten, Anh.
ISBN: 978-3-89336-542-5

19. **Untersuchungen zur Klimavariabilität auf dem Tibetischen Plateau - Ein Beitrag auf der Basis stabiler Kohlenstoff- und Sauerstoffisotope in Jahrringen von Bäumen waldgrenznaher Standorte**
von J. Griessinger (2008), XIII, 172 Seiten
ISBN: 978-3-89336-544-9

20. **Neutron-Irradiation + Helium Hardening & Embrittlement Modeling of 9%Cr-Steels in an Engineering Perspective (HELENA)**
by R. Chaouadi (2008), VIII, 139 pages
ISBN: 978-3-89336-545-6

21. **in Bearbeitung**

22. **Verbundvorhaben APAWAGS (AOEV und Wassergenerierung) – Teilprojekt: Brennstoffreformierung – Schlussbericht**
von R. Peters, R. C. Samsun, J. Pasel, Z. Porš, D. Stolten (2008), VI, 106 Seiten
ISBN: 978-3-89336-547-0

23. **FREEVAL**
Evaluation of a Fire Radiative Power Product derived from Meteosat 8/9 and Identification of Operational User Needs
Final Report
project coord. M. Schultz, M. Wooster (2008), 139 pages
ISBN: 978-3-89336-549-4

24. **Untersuchungen zum Alkaliverhalten unter Oxycoal-Bedingungen**
von C. Weber (2008), VII, 143, XII Seiten
ISBN: 978-3-89336-551-7

25. **Grundlegende Untersuchungen zur Freisetzung von Spurstoffen, Heißgaschemie, Korrosionsbeständigkeit keramischer Werkstoffe und Alkalirückhaltung in der Druckkohlenstaubfeuerung**
von M. Müller (2008), 207 Seiten
ISBN: 978-3-89336-552-4

26. **Analytik von ozoninduzierten phenolischen Sekundärmetaboliten in *Nicotiana tabacum* L. cv Bel W3 mittels LC-MS**
von I. Koch (2008), III, V, 153 Seiten
ISBN 978-3-89336-553-1

27. **IEF-3 Report 2009. Grundlagenforschung für die Anwendung**
(2009), ca. 230 Seiten
ISBN: 978-3-89336-554-8

28. **Influence of Composition and Processing in the Oxidation Behavior of MCrAlY-Coatings for TBC Applications**
by J. Toscano (2009), 168 pages
ISBN: 978-3-89336-556-2

29. **Modellgestützte Analyse signifikanter Phosphorbelastungen in hessischen Oberflächengewässern aus diffusen und punktuellen Quellen**
von B. Tetzlaff (2009), 149 Seiten
ISBN: 978-3-89336-557-9

30. **Nickelreaktivlot / Oxidkeramik – Fügungen als elektrisch isolierende Dichtungskonzepte für Hochtemperatur-Brennstoffzellen-Stacks**
von S. Zügner (2009), 136 Seiten
ISBN: 978-3-89336-558-6

31. **Langzeitbeobachtung der Dosisbelastung der Bevölkerung in radioaktiv kontaminierten Gebieten Weißrusslands – Korma-Studie**
von H. Dederichs, J. Pillath, B. Heuel-Fabianek, P. Hill, R. Lennartz (2009), Getr. Pag.
ISBN: 978-3-89336-532-3

32. **Herstellung von Hochtemperatur-Brennstoffzellen über physikalische Gasphasenabscheidung**
von N. Jordán Escalona (2009), 148 Seiten
ISBN: 978-3-89336-532-3

33. **Real-time Digital Control of Plasma Position and Shape on the TEXTOR Tokamak**
by M. Mitri (2009), IV, 128 pages
ISBN: 978-3-89336-567-8

34. **Freisetzung und Einbindung von Alkalimetallverbindungen in kohlebefeuerten Kombikraftwerken**
von M. Müller (2009), 155 Seiten
ISBN: 978-3-89336-568-5

35. **Kosten von Brennstoffzellensystemen auf Massenbasis in Abhängigkeit von der Absatzmenge**
von J. Werhahn (2009), 242 Seiten
ISBN: 978-3-89336-569-2

36. **Einfluss von Reoxidationszyklen auf die Betriebsfestigkeit von anodengestützten Festoxid-Brennstoffzellen**
von M. Ettler (2009), 138 Seiten
ISBN: 978-3-89336-570-8

37. **Großflächige Plasmaabscheidung von mikrokristallinem Silizium für mikromorphe Dünnschichtsolarmodule**
von T. Kilper (2009), XVII, 154 Seiten
ISBN: 978-3-89336-572-2

38. **Generalized detailed balance theory of solar cells**
by T. Kirchartz (2009), IV, 198 pages
ISBN: 978-3-89336-573-9

39. **The Influence of the Dynamic Ergodic Divertor on the Radial Electric Field at the Tokamak TEXTOR**
von J. W. Coenen (2009), xii, 122, XXVI pages
ISBN: 978-3-89336-574-6

40. **Sicherheitstechnik im Wandel Nuklearer Systeme**
von K. Nünighoff (2009), viii, 215 Seiten
ISBN: 978-3-89336-578-4

41. **Pulvermetallurgie hochporöser NiTi-Legierungen für Implanat- und Dämpfungsanwendungen**
von M. Köhl (2009), XVII, 199 Seiten
ISBN: 978-3-89336-580-7

42. **Einfluss der Bondcoatzusammensetzung und Herstellungsparameter auf die Lebensdauer von Wärmedämmschichten bei zyklischer Temperaturbelastung**
von M. Subanovic (2009), 188, VI Seiten
ISBN: 978-3-89336-582-1

43. **Oxygen Permeation and Thermo-Chemical Stability of Oxygen Permeation Membrane Materials for the Oxyfuel Process**
by A. J. Ellett (2009), 176 pages
ISBN: 978-3-89336-581-4

44. **Korrosion von polykristallinem Aluminiumoxid (PCA) durch Metalljodidschmelzen sowie deren Benetzungseigenschaften**
von S. C. Fischer (2009), 148 Seiten
ISBN: 978-3-89336-584-5

45. **IEF-3 Report 2009. Basic Research for Applications**
(2009), 217 Seiten
ISBN: 978-3-89336-585-2

46. **Verbundvorhaben ELBASYS (Elektrische Basissysteme in einem CFK-Rumpf) - Teilprojekt: Brennstoffzellenabgase zur Tankinertisierung - Schlussbericht**
von R. Peters, J. Latz, J. Pasel, R. C. Samsun, D. Stolten
(2009), xi, 202 Seiten
ISBN: 978-3-89336-587-6

47. **Aging of ^{14}C-labeled Atrazine Residues in Soil: Location, Characterization and Biological Accessibility**
by N. D. Jablonowski (2009), IX, 104 pages
ISBN: 978-3-89336-588-3

48. **Entwicklung eines energetischen Sanierungsmodells für den europäischen Wohngebäudesektor unter dem Aspekt der Erstellung von Szenarien für Energie- und CO_2 - Einsparpotenziale bis 2030**
von P. Hansen (2009), XXII, 281 Seiten
ISBN: 978-3-89336-590-6

49. **Reduktion der Chromfreisetzung aus metallischen Interkonnektoren für Hochtemperaturbrennstofzellen durch Schutzschichtsysteme**
von R. Trebbels (2009), iii, 135 Seiten
ISBN: 978-3-89336-591-3

50. **Bruchmechanische Untersuchung von Metall / Keramik-Verbundsystemen für die Anwendung in der Hochtemperaturbrennstoffzelle**
von B. Kuhn (2009), 118 Seiten
ISBN: 978-3-89336-592-0

51. **Wasserstoff-Emissionen und ihre Auswirkungen auf den arktischen Ozonverlust**
Risikoanalyse einer globalen Wasserstoffwirtschaft
von T. Feck (2009), 180 Seiten
ISBN: 978-3-89336-593-7

52. **Development of a new Online Method for Compound Specific Measurements of Organic Aerosols**
by T. Hohaus (2009), 156 pages
ISBN: 978-3-89336-596-8

53. **Entwicklung einer FPGA basierten Ansteuerungselektronik für Justageeinheiten im Michelson Interferometer**
von H. Nöldgen (2009), 121 Seiten
ISBN: 978-3-89336-599-9

54. **Observation – and model – based study of the extratropical UT/LS**
by A. Kunz (2010), xii, 120, xii pages
ISBN: 978-3-89336-603-3

55. **Herstellung polykristalliner Szintillatoren für die Positronen-Emissions-Tomographie (PET)**
von S. K. Karim (2010), VIII, 154 Seiten
ISBN: 978-3-89336-610-1

56. **Kombination eines Gebäudekondensators mit H2-Rekombinatorelementen in Leichwasserreaktoren**
von S. Kelm (2010), vii, 119 Seiten
ISBN: 978-3-89336-611-8

57. **Plant Leaf Motion Estimation Using A 5D Affine Optical Flow Model**
by T. Schuchert (2010), X, 143 pages
ISBN: 978-3-89336-613-2

58. **Tracer-tracer relations as a tool for research on polar ozone loss**
by R. Müller (2010), 116 pages
ISBN: 978-3-89336-614-9

59. **Sorption of polycyclic aromatic hydrocarbon (PAH) to Yangtze River sediments and their components**
by J. Zhang (2010), X, 109 pages
ISBN: 978-3-89336-616-3

60. **Weltweite Innovationen bei der Entwicklung von CCS-Technologien und Möglichkeiten der Nutzung und des Recyclings von CO_2**
Studie im Auftrag des BMWi
von W. Kuckshinrichs et al. (2010), X, 139 Seiten
ISBN: 978-3-89336-617-0

61. **Herstellung und Charakterisierung von sauerstoffionenleitenden Dünnschichtmembranstrukturen**
von M. Betz (2010), XII, 112 Seiten
ISBN: 978-3-89336-618-7

62. **Politikszenarien für den Klimaschutz V – auf dem Weg zum Strukturwandel, Treibhausgas-Emissionsszenarien bis zum Jahr 2030**
hrsg. von P. Hansen, F. Chr. Matthes (2010), 276 Seiten
ISBN: 978-3-89336-619-4

63. **Charakterisierung Biogener Sekundärer Organischer Aerosole mit Statistischen Methoden**
von C. Spindler (2010), iv, 163 Seiten
ISBN: 978-3-89336-622-4

64. **Stabile Algorithmen für die Magnetotomographie an Brennstoffzellen**
von M. Wannert (2010), ix, 119 Seiten
ISBN: 978-3-89336-623-1

65. **Sauerstofftransport und Degradationsverhalten von Hochtemperaturmembranen für CO2-freie Kraftwerke**
von D. Schlehuber (2010), VII, 139 Seiten
ISBN: 978-3-89336-630-9

66. **Entwicklung und Herstellung von foliengegossenen, anodengestützten Festoxidbrennstoffzellen**
von W. Schafbauer (2010), VI, 164 Seiten
ISBN: 978-3-89336-631-6

67. **Disposal strategy of proton irradiated mercury from high power spallation sources**
by S. Chiriki (2010), xiv, 124 pages
ISBN: 978-3-89336-632-3

68. **Oxides with polyatomic anions considered as new electrolyte materials for solid oxide fuel cells (SOFCs)**
by O. H. Bin Hassan (2010), vii, 121 pages
ISBN: 978-3-89336-633-0

69. **Von der Komponente zum Stack: Entwicklung und Auslegung von HT-PEFC-Stacks der 5 kW-Klasse**
von A. Bendzulla (2010), IX, 203 Seiten
ISBN: 978-3-89336-634-7

70. **Satellitengestützte Schwerewellenmessungen in der Atmosphäre und Perspektiven einer zukünftigen ESA Mission (PREMIER)**
von S. Höfer (2010), 81 Seiten
ISBN: 978-3-89336-637-8

71. **Untersuchungen der Verhältnisse stabiler Kohlenstoffisotope in atmosphärisch relevanten VOC in Simulations- und Feldexperimenten**
von H. Spahn (2010), IV, 210 Seiten
ISBN: 978-3-89336-638-5

72. **Entwicklung und Charakterisierung eines metallischen Substrats für nanostrukturierte keramische Gastrennmembranen**
von K. Brands (2010), vii, 137 Seiten
ISBN: 978-3-89336-640-8

73. **Hybridisierung und Regelung eines mobilen Direktmethanol-Brennstoffzellen-Systems**
von J. Chr. Wilhelm (2010), 220 Seiten
ISBN: 978-3-89336-642-2

74. **Charakterisierung perowskitischer Hochtemperaturmembranen zur Sauerstoffbereitstellung für fossil gefeuerte Kraftwerksprozesse**
von S.A. Möbius (2010) III, 208 Seiten
ISBN: 978-3-89336-643-9

75. **Characterization of natural porous media by NMR and MRI techniques: High and low magnetic field studies for estimation of hydraulic properties**
by L.-R. Stingaciu (2010), 96 pages
ISBN: 978-3-89336-645-3

76. **Hydrological Characterization of a Forest Soil Using Electrical Resistivity Tomography**
by Chr. Oberdörster (2010), XXI, 151 pages
ISBN: 978-3-89336-647-7

77. **Ableitung von atomarem Sauerstoff und Wasserstoff aus Satellitendaten und deren Abhängigkeit vom solaren Zyklus**
von C. Lehmann (2010), 127 Seiten
ISBN: 978-3-89336-649-1

78. **18th World Hydrogen Energy Conference 2010 – WHEC2010**
Proceedings
Speeches and Plenary Talks
ed. by D. Stolten, B. Emonts (2010)
ISBN: 978-3-89336-658-3

78-1. **18th World Hydrogen Energy Conference 2010 – WHEC2010**
Proceedings
Parallel Sessions Book 1:
Fuel Cell Basics / Fuel Infrastructures
ed. by D. Stolten, T. Grube (2010), ca. 460 pages
ISBN: 978-3-89336-651-4

78-2. **18th World Hydrogen Energy Conference 2010 – WHEC2010**
Proceedings
Parallel Sessions Book 2:
Hydrogen Production Technologies – Part 1
ed. by D. Stolten, T. Grube (2010), ca. 400 pages
ISBN: 978-3-89336-652-1

78-3. **18th World Hydrogen Energy Conference 2010 – WHEC2010**
Proceedings
Parallel Sessions Book 3:
Hydrogen Production Technologies – Part 2
ed. by D. Stolten, T. Grube (2010), ca. 640 pages
ISBN: 978-3-89336-653-8

78-4. **18th World Hydrogen Energy Conference 2010 – WHEC2010**
Proceedings
Parallel Sessions Book 4:
Storage Systems / Policy Perspectives, Initiatives and Cooperations
ed. by D. Stolten, T. Grube (2010), ca. 500 pages
ISBN: 978-3-89336-654-5

78-5. **18th World Hydrogen Energy Conference 2010 – WHEC2010**
Proceedings
Parallel Sessions Book 5:
Stategic Analysis / Safety Issues / Existing and Emerging Markets
ed. by D. Stolten, T. Grube (2010), ca. 530 pages
ISBN: 978-3-89336-655-2

78-6. **18th World Hydrogen Energy Conference 2010 – WHEC2010**
Proceedings
Parallel Sessions Book 6:
Stationary Applications / Transportation Applications
ed. by D. Stolten, T. Grube (2010), ca. 330 pages
ISBN: 978-3-89336-656-9

78 Set (complete book series)

18th World Hydrogen Energy Conference 2010 – WHEC2010 Proceedings
ed. by D. Stolten, T. Grube, B. Emonts (2010)
ISBN: 978-3-89336-657-6

79. **Ultrafast voltex core dynamics investigated by finite-element micromagnetic simulations**
by S. Gliga (2010), vi, 144 pages
ISBN: 978-3-89336-660-6

80. **Herstellung und Charakterisierung von keramik- und metallgestützten Membranschichten für die CO_2-Abtrennung in fossilen Kraftwerken**
von F. Hauler (2010), XVIII, 178 Seiten
ISBN: 978-3-89336-662-0

81. **Experiments and numerical studies on transport of sulfadiazine in soil columns**
by M. Unold (2010), xvi, 115 pages
ISBN: 978-3-89336-663-7

82. **Prompt-Gamma-Neutronen-Aktivierungs-Analyse zur zerstörungsfreien Charakterisierung radioaktiver Abfälle**
von J.P.H. Kettler (2010), iv, 205 Seiten
ISBN: 978-3-89336-665-1

83. **Transportparameter dünner geträgerter Kathodenschichten der oxidkeramischen Brennstoffzelle**
von C. Wedershoven (2010), vi, 137 Seiten
ISBN: 978-3-89336-666-8

84. **Charakterisierung der Quellverteilung von Feinstaub und Stickoxiden in ländlichem und städtischem Gebiet**
von S. Urban (2010), vi, 211 Seiten
ISBN: 978-3-89336-669-9

85. **Optics of Nanostructured Thin-Film Silicon Solar Cells**
by C. Haase (2010), 150 pages
ISBN: 978-3-89336-671-2

86. **Entwicklung einer Isolationsschicht für einen Leichtbau-SOFC-Stack**
von R. Berhane (2010), X, 162 Seiten
ISBN: 978-3-89336-672-9

87. **Hydrogen recycling and transport in the helical divertor of TEXTOR**
by M. Clever (2010), x, 172 pages
ISBN: 978-3-89336-673-6

88. **Räumlich differenzierte Quantifizierung der N- und P-Einträge in Grundwasser und Oberflächengewässer in Nordrhein-Westfalen unter besonderer Berücksichtigung diffuser landwirtschaftlicher Quellen**
von F. Wendland et. al. (2010), xii, 216 Seiten
ISBN: 978-3-89336-674-3

89. **Oxidationskinetik innovativer Kohlenstoffmaterialien hinsichtlich schwerer Lufteinbruchstörfälle in HTR´s und Graphitentsorgung oder Aufarbeitung**
von B. Schlögl (2010), ix, 117 Seiten
ISBN: 978-3-89336-676-7

90. **Chemische Heißgasreinigung bei Biomassenvergasungsprozessen**
von M. Stemmler (2010), xv, 196 Seiten
ISBN: 978-3-89336-678-1

91. **Untersuchung und Optimierung der Serienverschaltung von Silizium-Dünnschicht-Solarmodulen**
von S. Haas (2010), ii, 202 Seiten
ISBN: 978-3-89336-680-4

92. **Non-invasive monitoring of water and solute fluxes in a cropped soil**
by S. Garré (2010), xxiv, 133 pages
ISBN: 978-3-89336-681-1

93. **Improved hydrogen sorption kinetics in wet ball milled Mg hydrides**
by L. Meng (2011), II, 119 pages
ISBN: 978-3-89336-687-3

94. **Materials for Advanced Power Engineering 2010**
ed. by J. Lecomte-Beckers, Q. Contrepois, T. Beck and B. Kuhn
(2010), 1327 pages
ISBN: 978-3-89336-685-9

95. **2D cross-hole MMR – Survey design and sensitivity analysis for cross-hole applications of the magnetometric resistivity**
by D. Fielitz (2011), xvi, 123 pages
ISBN: 978-3-89336-689-7

96. **Untersuchungen zur Oberflächenspannung von Kohleschlacken unter Vergasungsbedingungen**
von T. Melchior (2011), xvii, 270 Seiten
ISBN: 978-3-89336-690-3

97. **Secondary Organic Aerosols: Chemical Aging, Hygroscopicity, and Cloud Droplet Activation**
by A. Buchholz (2011), xiv, 134 pages
ISBN: 978-3-89336-691-0

98. **Chrom-bezogene Degradation von Festoxid-Brennstoffzellen**
von A. Neumann (2011), xvi, 218 Seiten
ISBN: 978-3-89336-692-7

99. **Amorphous and microcrystalline silicon applied in very thin tandem solar cells**
by S. Schicho (2011), XII, 190 pages
ISBN: 978-3-89336-693-4

100. **Sol-gel and nano-suspension electrolyte layers for high performance solid oxide fuel cells**
by F. Han (2011), iv, 131 pages
ISBN: 978-3-89336-694-1

101. **Impact of different vertical transport representations on simulating processes in the tropical tropopause layer (TTL)**
by F. Plöger (2011), vi, 104 pages
ISBN: 978-3-89336-695-8

102. **Untersuchung optischer Nanostrukturen für die Photovoltaik mit Nahfeldmikroskopie**
von T. Beckers (2011), xiii, 128 Seiten
ISBN: 978-3-89336-696-5

103. **Impact of contamination on hydrogenated amorphous silicon thin films & solar cells**
by J. Wördenweber (2011), XIV, 138 pages
ISBN: 978-3-89336-697-2

104. **Water and Organic Nitrate Detection in an AMS: Laboratory Characterization and Application to Ambient Measurements**
by A. Mensah (2011), XI, 111 pages
ISBN: 978-3-89336-698-9

105. **Entwicklung eines neuen Konzepts zur Steuerung der thermischen Ausdehnung von glaskeramischen Verbundwerkstoffen mit angepasster Fließfähigkeit am Beispiel der Hochtemperatur-Brennstoffzelle**
von E. Wanko (2011), xi, 134 Seiten
ISBN: 978-3-89336-705-4

106. **Tomographic reconstruction of atmospheric volumes from infrared limb-imager measurements**
by J. Ungermann (2011), xiv, 153 pages
ISBN: 978-3-89336-708-5

107. **Synthese und Identifizierung von substituierten Mg-Al-Cl Doppelhydroxidverbindungen mit Schwerpunkt IR-Spektroskopie**
von B. Hansen (2011), XII, 121 Seiten
ISBN: 978-3-89336-709-2

108. **Analysis of spatial soil moisture dynamics using wireless sensor networks**
by U. Rosenbaum (2011), xxii, 120 pages
ISBN: 978-3-89336-710-8

109. **Optimierung von APS-ZrO2-Wärmedämmschichten durch Variation der Kriechfestigkeit und der Grenzflächenrauhigkeit**
von M. E. Schweda (2011), 168 Seiten
ISBN: 978-3-89336-711-5

110. **Sorption of a branched nonylphenol isomer and perfluorooctanoic acid on geosorbents and carbon nanotubes**
by C. Li (2011), X, 102 pages
ISBN: 978-3-89336-716-0

111. **Electron Transport in the Plasma Edge with Rotating Resonant Magnetic Perturbations at the TEXTOR Tokamak**
by H. Stoschus (2011), iv, 113 pages
ISBN: 978-3-89336-718-4

112. **Diffusion and Flow Investigations in Natural Porous Media by Nuclear Magnetic Resonance**
by N. Spindler (2011), viii, 144 pages
ISBN: 978-3-89336-719-1

113. **Entwicklung und Erprobung des Hygrometer for Atmospheric Investigations**
von T. Klostermann (2011), IV, 118 Seiten
ISBN: 978-3-89336-723-8

114. **Application of functional gene arrays for monitoring influences of plant/seasons on bacterial functions and community structures in constructed wetlands (Bitterfeld, Germany)**
by J. Ning (2011), xiv, 157 pages
ISBN: 978-3-89336-724-5

115. **Wasseraustrag aus den Kathodenkanälen von Direkt-Methanol-Brennstoffzellen**
von A. Schröder (2011), VII, 228 Seiten
ISBN: 978-3-89336-727-6

116. **CITYZEN Climate Impact Studies**
ed. by M. Schultz (2011), 45 pages
ISBN: 978-3-89336-729-0

117. **Software Tools zum interoperablen Austausch und zur Visualisierung von Geodatensätzen über das Internet**
von M. Schultz, M. Decker, S. Lührs (2011), iv, 156 Seiten
ISBN: 978-3-89336-730-6

118. **Optimierung eines Leichtbaudesigns für ein SOFC-Brennstoffzellenstack**
von T. Nguyen-Xuan (2011), III, 154 Seiten
ISBN: 978-3-89336-732-0

119. **Institute of Energy and Climate Research IEK-6:**
Nuclear Waste Management & Reactor Safety Report 2009/2010
Material Science for Nuclear Waste Management
ed. by M. Klinkenberg, S. Neumeier, D. Bosbach (2011), 242 pages
ISBN: 978-3-89336-735-1

120. **Fate of the Antibiotic Sulfadiazine in Yangtze River Sediments: Transformation, Sorption and Transport**
by N. Meng (2011), XII, 111 pages
ISBN: 978-3-89336-736-8

121. **Thermodynamische Eigenschaften gasförmiger und kondensierter Verbindungen für Hochtemperaturanwendungen**
von T. Markus (2011), II, 131 Seiten
ISBN: 978-3-89336-728-3

122. **Ein neues LIF-Instrument für flugzeug- und bodengebundene Messungen von OH- und HO_2-Radikalen in der Troposphäre**
von S. Broch (2011), IV, 160 Seiten
ISBN: 978-3-89336-742-9

123. **Processes in the Yangtze River System - Experiences and Perspectives**
Workshop-Proceedings
ed. by S. Küpper, G. Subklew, R.-D. Wilken (2011), 83 pages
ISBN: 978-3-89336-744-3

124. **Thermo-Mechanical Properties of Mixed Ion-Electron Conducting Membrane Materials**
by B. Huang (2011), 130 pages
ISBN: 978-3-89336-746-7

125. **Growth, Etching, and Stability of Sputtered ZnO:Al for Thin-Film Silicon Solar Cells**
by J. I. Owen (2011), xv, 192 pages
ISBN: 978-3-89336-749-8

126. **Entwicklung geträgerter $Ba_{0,5}Sr_{0,5}Co_{0,5}Fe_{0,2O3-\delta}$ Sauerstoff-Permeationsmembranen**
von F. Schulze-Küppers (2011), ii, 119 Seiten
ISBN: 978-3-89336-752-8

127. **Development of the 2-Component-Injection Moulding for Metal Powders**
by A. P. Cysne Barbosa (2011), XIV, 150 pages
ISBN: 978-3-89336-753-5

Schriften des Forschungszentrums Jülich
Reihe Energie & Umwelt / Energy & Environment

128. **Performance of Tungsten-Based Materials and Components under ITER and DEMO Relevant Steady-State Thermal Loads**
by G. H. Ritz (2011), X, 128 pages
ISBN: 978-3-89336-755-9

Energie & Umwelt / Energy & Environment
Band / Volume 128
ISBN 978-3-89336-755-9

JÜLICH
FORSCHUNGSZENTRUM